ULTRATHIN METALLIC FILMS OF MN, AGMN AND VMN GROWN BY MOLECULAR BEAM EPITAXY

by

Chian Liu

B.Sc.(diploma), Wuhan University, 1969

M.Sc., Simon Fraser University, 1983

THESIS SUBMITTED IN PARTIAL FULFILLMENT OF

THE REQUIREMENTS FOR THE DEGREE OF

DOCTOR OF PHILOSOPHY

in the Department

of

Physics

SIMON FRASER UNIVERSITY

February 1986

APPROVAL

Name: Chian Liu

Degree: DOCTOR OF PHILOSOPHY

Title of thesis: Ultrathin Metallic Films of Mn, AgMn and VMn Grown by Molecular Beam Epitaxy

Examining Committee:

Chairman: Dr. Richard H. Enns

Dr. Anthony S. Arrott
Senior Supervisor

Dr. Bretislav Heinrich

Dr. Michael Plischke

Dr. John F. Cochran

Dr. Carl Rau
External Examiner
Professor of Physics Department
Rice University, Houston, Texas
TX77251 USA

Date Approved February 24, 1986

PARTIAL COPYRIGHT LICENSE

I hereby grant to Simon Fraser University the right to lend my thesis, project or extended essay (the title of which is shown below) to users of the Simon Fraser University Library, and to make partial or single copies only for such users or in response to a request from the library of any other university, or other educational institution, on its own behalf or for one of its users. I further agree that permission for multiple copying of this work for scholarly purposes may be granted by me or the Dean of Graduate Studies. It is understood that copying or publication of this work for financial gain shall not be allowed without my written permission.

Title of Thesis/Project/Extended Essay

Ultrathin Metallic Films of Mn,

AgMn and VMn Grown by Molecular Beam Epitaxy

Author:

(signature)

Chian Liu

(name)

Feb. 27. 86

(date)

ABSTRACT

Ultrathin metal films of Mn, AgMn and VMn *etc.* have been grown on Ru(001) in an MBE system for the study of the epitaxy and the magnetic properties of the first few Mn layers when the Mn lattice is expanded to match the Ru lattice. It was found that Mn can grow on Ru epitaxially layer by layer and the first two layers of Mn on Ru have an expanded structure with a Ru lattice spacing. A new phase of Mn metal formed from the third layer on up to over 60 layers. This new phase of Mn has a so-called trimerized structure with the closest approach of ~2.39Å. Mn can also grow on Fe(100) epitaxially with an Fe spacing up to over 15 layers. The above conclusions have been demonstrated by AES, XPS, RHEED and EELFS analysis.

The magnetic properties of these MBE-grown thin films have been deduced from 3s XPS multiplet splittings by comparison with all the 3d transition elements using the computer data processing technique and Doniach-Sunjic lineshape curve fittings. It was found that it is the intensity of the satellite peak, not the energy splitting, which is more sensitive to the spin polarization of 3d electrons. The satellite intensity decreases from the expanded Mn and Mn in Ag to the trimerized Mn and Mn on Fe to Mn in V. This observation is related to the lattice spacing between Mn atoms and to the thermodynamical measurements of magnetic moment for AgMn (which has $5\mu_B$ per Mn atom) and VMn (which has no local moment). It is concluded that the satellite peak represents a $5\mu_B$ state which exists in every form of Mn on the time scale of 4×10^{-15}s and the magnetic moment of Mn atoms increases as the lattice spacing increases.

DEDICATION

TO WORLD PEACE AND PROGRESS

ACKNOWLEDGMENTS

I wish to express my sincere thanks to my senior supervisor, Professor A. S. Arrott, for his invaluable guidance and warm encouragement during the course of this research. I am very glad to have the honour to have been supervised by Professor Arrott. His knowledge, wisdom, perseverance and scientific spirit are only a few things I will never forget. I benefited a great deal from his personal influence.

I wish to thank the director of Surface Science Lab, Dr. B. Heinrich, for the experimental help and theoretical discussions. Those long hours we spent together for carrying out our experiments have left beautiful memories.

Thanks are also due to Dr. N. Alberding for carrying out the EELFS analysis and for his other friendly help, and to Mr. K. Urquhart for the computer programming and frequently computer assistance. The help from the technical and secretarial staff of the University and of the Physics Department is also very appreciated.

I wish to express my deep gratitude to the Simon Fraser University community, from the President and faculty members to the service staff and my fellow students, for their concern, friendship and enormous help, which made my stay in Canada a very pleasant one.

The financial support from Simon Fraser University, the Natural Sciences and Engineering Research Council of Canada and my supervisor is also very gratefully acknowledged.

TABLE OF CONTENTS

LIST OF TABLES

LIST OF FIGURES

CHAPTER 1

INTRODUCTION

For a long time people have been fascinated by the magnetic properties of thin solid films. This is because, on the one hand, thin magnetic films have potential applications in computer memories (see, e.g., Chaudhari *et al.* (1977)), magneto-optical waveguides (Okuda *et al.* (1983)) and magnetoelastic devices (Salansky (1970)) etc., and on the other hand, thin magnetic film studies can help people to a better understanding of magnetism. Especially in recent years, due to the rapid development of computers and ultrahigh vacuum technique, people can now carry out complicated calculations for more realistic systems and perform more ideal experiments to compare with the theory. Although, to date, a coherent unified theory of surface and film magnetism is still absent, quite a few theoretical calculations for surfaces and thin films have been reported (see, e.g., Wang and Freeman (1980), Jepsen *et al.* (1980, 1982) and Fu *et al.* (1985) *etc.*). A great deal of effort has also been contributed by experimental physicists. Different kinds of surface and thin film systems such as isolated or quasi-isolated single layer systems and vacuum deposited thin film systems have been studied. In the following we summarize briefly some theoretical and experimental work on magnetic properties of these systems. The cited works are only some examples related to our research and a complete survey is not attempted.

For ferromagnetic unsupported single layer films, Wang *et al.* (1981) have performed a self-consistent, spin-polarized energy band calculation for an isolated monolayer of Ni(001) and found an increased moment of 0.85 μ_B/atom compared to the bulk value of 0.62 μ_B/atom as obtained from the value of the center layer in a Ni(110) film by the same method, where μ_B is the Bohr magneton. Self-consistent, spin-polarized energy band calculations on unsupported single layer films of Fe, Co, Ni and Pd have been carried out by Noffke and Fritsche (1981). They found that the spin polarization in single layers of ferromagnetic materials is generally

larger than in the bulk and the associated magnetic moment per atom lies between the value of the respective free atom and that of the bulk. Recently Fu *et al.* (1985) have carried out self-consistent full-potential linearized augmented plane-wave calculations for a number of transition-metal-noble-metal systems. They found especially a large magnetic moment of 4.12 μ_B/atom for an isolated monolayer Cr(001) film and 3.7 μ_B/atom for a monolayer of Cr(001) deposited on Au(001) compared to the Cr bulk value of 0.59 μ_B/atom. This big enhancement in magnetic moment is mainly due to that in the isolated single layer systems, by which we mean that the single layers are free from crystal relaxation or reconstruction and isolated from each other, the reduced coordination number will lead to a band narrowing and an increase in density of states at the Fermi level and result in stronger magnetization. Unfortunately, no experiment has been done for this system due to the difficulty of making isolated, single layer samples. However, the systems studied in the following experiments may be considered as quasi-isolated single layer systems and can serve as examples to show the magnetic properties of these systems.

We have carried out some experiments on a quasi-isolated single layer system (Liu (1983)). By intercalation of hydrogen and water into transition-metal dichalcogenides TaS_2 and NbS_2 layer compounds followed by ultrasonic dispersion, we have successfully made TaS_2 and NbS_2 single layer water suspensions (Liu *et al.* (1984)). By single layers we mean a molecular layer composed of a sheet of Ta (Nb) atoms sandwiched by two sheets of S atoms. TaS_2 and NbS_2 are anisotropic, paramagnetic metals and water can be considered as a magnetic insulator. In a magnetic field TaS_2 and NbS_2 tend to align themselves perpendicular to the field because for them $\chi_{perpen} > \chi_{para}$, where χ_{perpen} and χ_{para} are the magnetic susceptibility perpendicular and parallel to the layer respectively. By measuring the optical absorption of these single layer water suspensions as a function of the magnetic field strength, we found that the magnetic susceptibility and anisotropy are very likely a few times bigger for these single layers compared to that of the corresponding bulk crystals (Liu and Frindt (1985)). No direct magnetic susceptibility measurement was tried due to the low value of susceptibility of these single layer

suspensions. A theoretic calculation of the magnetic susceptibility of single layer NbS_2 has been carried out by Li *et al.* (1985). They calculated the band structure for single layer NbS_2 using a tight binding model with zero interlayer interaction and using this model calculated the magnetic susceptibility. They found that χ_{para} is relatively unchanged and χ_{perpen} has an increase of a factor of about three over the expected bulk value, in good agreement with our observation.

People have tried to intercalate transition metals into layer compounds and thus obtained quasi-isolated, two-dimensional systems with the intercalate atoms sitting in between the layers of layer compounds (which are paramagnetic materials). For a review of the 3d transition metal intercalation complexes, see Beal (1979). Friend *et al.* (1977) and Parkin and Friend (1980) have studied magnetic properties of 3d transition metal intercalates of the niobium and tantalum dichalcogenides $M_{1/3}TaS_2$, $M_{1/3}NbS_2$ (M=V, Cr, Mn, Fe, Co, Ni), $Mn_{1/4}TaS_2$ and $Fe_{1/4}NbSe_2$, where the intercalated ions form an ordered superlattice. They found that there is a charge transfer from the intercalates into the lowest unoccupied bands in the host compounds and the intercalates become positive ions. Their magnetic susceptibility vs. temperature measurements show that the V, Cr and Mn intercalation complexes order ferromagnetically, the Co and Ni complexes order antiferromagnetically and the Fe complexes show both types of magnetic behaviour. They also found that the size of the effective magnetic moment of the complexes is close to the spin-only moment of the intercalate ions and not sensitive to the host compounds.

More recently, Barry and Hughes (1983) have studied $Mn_{1/3}NbS_2$ and $Fe_{1/3}NbS_2$ by using x-ray photoemission. They found a multiplet splitting of $\Delta E=6.1eV$ for Mn intercalant 3s peak and $\Delta E=4.5eV$ for Fe 3s peak. This multiple splitting corresponds to two final configurations with the 3s core hole having its spin either parallel or antiparallel to that of the unpaired 3d valence electrons and thus gives information on the valence shell electron spin. We will discuss this in more detail in later chapters.

Due to the development of Ultra-High Vacuum (UHV) technique people now can grow magnetic elements (e.g., Fe, Co and Ni) on different substrates with much better quality than two decades ago. It is found that the thin deposited films of these magnetic elements are not magnetically "dead" as initially suggested by Liebermann *et al.* (1970), but depend sensitively on substrate composition. Liebermann *et al.* reported that their electroplated Ni thin films on a Cu substrate became paramagnetic. Tersoff and Falicov (1982) and Wang *et al.* (1982) have calculated the Ni on Cu system and found that a Ni monolayer is substantially magnetic on Cu(100) substrates and paramagnetic on Cu(111). They found also that magnetization is suppressed at the Ni–Cu interface, but enhanced in isolated thin films. On the experimental side, UHV-deposited thin Ni films (as thin as 2 layers) on Cu were found magnetic by using electron capture spectroscopy (Rau and Eichner (1981)) and using spin-polarized photoemission (Pierce and Siegmann (1974)). For Ni, Fe or Co films on Pb–Bi alloy substrates and Al substrates, Bergmann (1978) and Meservey *et al.* (1980) found that when Ni film thickness is reduced below 2.5–3 atomic layers there is a transition from ferromagnetism to paramagnetism. Their measurements were carried out at a temperature down to 5K and 0.4K respectively. They also found that Fe or Co films retained their magnetic moment down to submonolayer thickness, even on the substrates where Ni lost its magnetic moment. All these experiments suggest that for thin deposited films there are still a lot of unknowns and the influence of the substrate composition on the magnetic properties of thin films is very important.

An important factor that affects the magnetic properties of thin deposited films is the lattice mismatch between these thin film and the substrate, especially when the deposited film is uniformly expanded to a larger lattice spacing compared to the bulk value. It is a well known fact that the magnetic properties of metals as well as alloys are related to the arrangement and separation of atoms in the lattice (see, e.g., Pearson (1958), Shiga (1973)). One would expect the same effect in the deposited thin films. In this respect, Brodsky (1981, 1983) has made metal film sandwiches containing Pd and Au by UHV-deposition. He found that Pd has a stretched

lattice parameter in the Au–Pd–Au sandwich and its magnetic susceptibiltity increases tremendously ($\chi/\chi_0 \simeq 500$, where χ and χ_0 are the magnetic susceptibilities for Pd in Au–Pd–Au and for bulk Pd respectively). Bulk Pd is a near–ferromagnetic material($\chi_0 \simeq 0.0007$ emu/g·atom at 2K). this increase in χ is attributed to the narrowing of the density of states of Pd films and the stretching of the Pd lattice. On the other hand, when Pd is subjected to high pressures (which decreases the Pd lattice paramater), its magnetic susceptibility deceases . Similar decease in magnetic susceptibility for Fe under high pressure is also observed (Williamson *et al.* (1972)).

The basic physics behind this relationship of lattice spacings and magnetic properties is that the lattice spacing determines the overlap of electron wave functions of neighboring atoms and thus affects the Coulomb interaction of electrons. It is well known that for the ground state configuration and for configurations containing equivalent electrons (i.e., electrons in the same subshell), there have been established empirically Hund's rules. According to Hund's rule, the lowest electrostatic energy corresponds to the largest possible value of S for a given configuration. S is the total spin quantum number of the atom. For a half–filled subshell, parallel spins give the largest S. By the Pauli exclusion princicple, electrons with parallel spins can not get close to each other compared to those with antiparallel spins. Thus electrons with parallel spins have a smaller Coulomb interaction. This is the physical explanation of Hund's rule. However, a smaller interatomic distance will lead to an increase in kinetic energy of valence electrons. This increase in electronic kinetic energy may cause the atom not to obey Hund's rule. Mn is a good example. Atomic Mn has five electrons in the d subshell and should have a large magnetic moment according to Hund's rule. But Mn has a smaller lattice spacing compared to that of Fe and Co. It is believed that the squeezing of the Mn atom causes Mn not to obey Hund's rule and to become páramagnetic. An idea thus follows, i.e., Mn might become more magnetic if the atoms could be further separated. Then depending upon the strength of the interatomic exchange it might become ferromagnetic. This is the initial motivation of the present work.

We have grown and investigated epitaxial Mn layers on the close-packed (001) surface of Ru (Heinrich *et al.* (1985)). Ru has a lattice constant close to that of Mn_4N which is a ferrimagnetic material in which the one out of four Mn atoms that is not squeezed by a neighboring N atom has $4\mu_B$, a possible value under Hund's rule. In our Mn growth, as indicated by Reflection High Energy Electron Diffraction (RHEED) and Extended Energy Loss Fine Structure (EELFS) analysis, the first 2-3 layers of the grown Mn did have an expanded lattice with the same lateral lattice constant as that of Ru. But a new phase of Mn with a trimerized structure formed after the formation of the third Mn overlayer. We have also grown Mn on bcc Fe(100) epitaxially and grown AgMn and VMn alloys on Ru by codeposition. The growth rate of these thin films and the composition of the alloys were determined by X-ray Photoelectron Spectroscopy (XPS) and Auger Electron Spectroscopy (AES) analysis. The surface conditions were closely monitored by AES (or XPS in some cases). The magnetic properties of these MBE-grown thin films were extensively studied by analyzing the Mn 3s XPS multiplet splittings using the computer data processing technique and Doniach and Sunjic lineshape curve fittings. These splittings were also compared with that in 3d transition elements from Ti through Cu. We tried to deduce the information of 3d spin polarization from 3s splittings (Arrott *et al.* (1985)). It was found that the intensity of the satellite peak for the Mn films decreases from Mn in AgMn(~17% at. Mn) and the expanded Mn on Ru to the trimerized Mn on Ru and Mn on Fe to Mn in VMn(~25% at. Mn). For Ti through Cu, the intensity of the satellite peak is highest for α-Mn and Fe and decreases on both side of Mn and Fe. The energy splitting for Mn in its different forms also decreases slightly as the intensity of the satellite peak decreases. This is qualitatively in agreement with what we expect from van Vleck (1934)'s theorem about the exchange splitting and with results of thermodynamical measurements of magnetic moment made for AgMn and VMn. We thus conclude that expanded Mn does have larger magnetic moment. The details will be discussed in later chapters.

The present thesis is organized as follows. Following the Introduction, in Chapter 2 we will describe the apparatus which we used in our experiments. The main apparatus is a commercial PHI-400 Molecular Beam Epitaxial (MBE) systsm in which RHEED, mass spectrometry, XPS and AES techniques are combined. Basic concepts of RHEED, XPS and AES are also introduced in Chapter 2. In Chapter 3, the growth of epitaxial layers of Mn, Ag and Mn-Ag *etc.* will be discussed. In Chapter 4 we will discuss the EELFS analysis on Mn overlayers. In Chapter 5 and Chapter 6, XPS and AES results will be analyzed. Important conclusions about the present study are summarized in Chapter 7. Some details about the instruments, some derivations and some of our computer programs are presented in the Appendix.

CHAPTER 2

APPARATUS AND INTRODUCTION OF RHEED, XPS AND AES

The apparatus we were using is a PHI-400 (Physical Electronics Division, Perkin-Elmer Corporation, U.S.A.) MBE system equipped with a UTI-100C (Uthe Technology International Corporation, U.S.A.) quadrupole mass analyzer, and RHEED, XPS, and AES instruments. For data collection, a Nicolet-1074 (Nicolet Instrument Corporation, U.S.A.) Signal Averager was used. A schematic diagram showing the major parts of our system is shown in Fig. 2.1. The basic operation principles of the vacuum system, the quadrupole mass analyzer and elementary concepts about RHEED, XPS, AES are reviewed in the following sections.

2.1 Vacuum Systems and Quadrupole Mass Analyzer

Since molecular beam epitaxy is essentially an Ultra-High Vacuum (UHV) deposition technique and RHEED, XPS, AES and mass analyzer all need very high vacuum, the UHV technique is extremely important in the present work. In our system, several different high vacuum pumps are used, namely, cryopump, ion pump, cryosorption pump and turbopump. By using the combination of these pumping systems, an ultimate UHV of $3x10^{-11}$ Torr in the growth chamber and $3.5x10^{-11}$ Torr in the analyzing chamber were obtained. The basic operation principles of these pumps as well as some other high vacuum techniques applied in the system are presented in Appendix A.

A UTI quadrupole mass analyzer is mounted in the growth chamber of our MBE system. It is very useful in analyzing the residual gases in the UHV system and in detecting the arriving rate of the deposition atoms. Also it is quite conveniently used as a leakage detector whenever there is a suspicion of possible leakage of the vacuum system. Details of UTI are given in

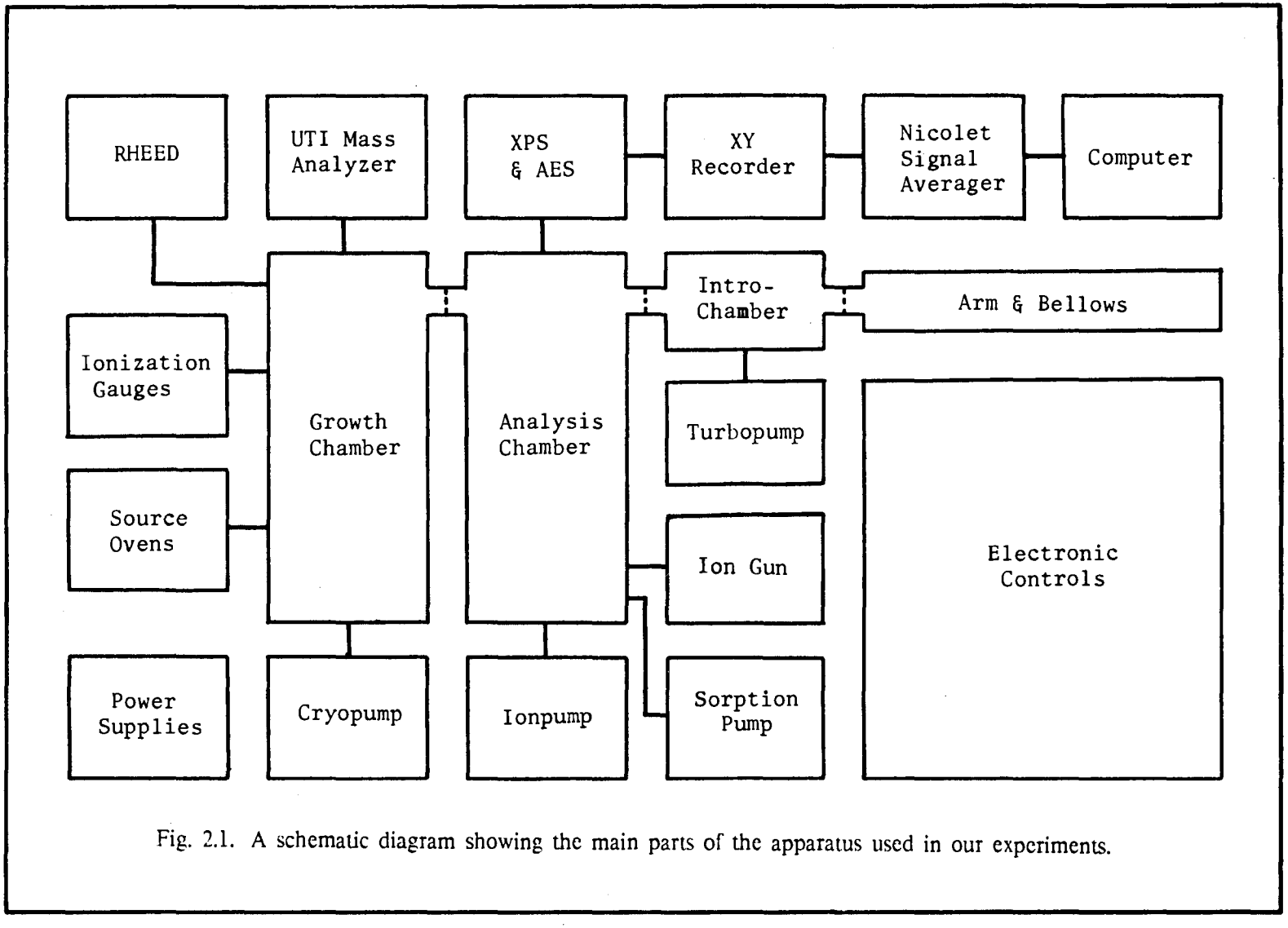

Fig. 2.1. A schematic diagram showing the main parts of the apparatus used in our experiments.

Appendix B.

2.2 RHEED — Reflection High Energy Electron Diffraction

A very important instrument in any MBE system is RHEED—Reflection High Energy Electron Diffraction. It is named "RHEED" because of its use of high energy electrons (10 keV to 100 keV) and because of its reflection feature. It is thus distinguished from LEED (Low Energy Electron Diffraction) and HEED (transmission High Energy Electron Diffraction). It is also frequently called RED (Reflection Electron Diffraction) for simplicity. Due to the very small incident angle used (1 to 5 degrees) in RHEED, the electron energy normal to the sample surface is very small and the electron beam can only penetrate a very thin surface layer. This fact makes RHEED an important tool in investigating the surface structure of material. It can be used to detect very thin deposits (even a submonolayer), the film smoothness and surface reconstructions *etc.* It is very useful especially in the study of molecular beam epitaxial growth, because the favourable glancing incidence geometry enables a continuous observation of the surface of the film while growth is taking place.

2.2.1 General aspects of RHEED patterns

In the ultrahigh vacuum MBE growth chamber, an electron gun and a display screen are the basic RHEED components. Electrons from the electron gun strike the sample surface in a glancing incidence angle and then reflect to the screen. The primary electrons together with the reflected and diffracted ones are displayed on the screen. The primary electrons (i.e., those which miss the sample) form a bright spot on the screen. This bright spot appears alone in the apparent shadow formed by the sample. The reflected electrons are displayed among diffraction patterns that may appear in the brighter portion of the screen. A sample with an amorphous surface gives no discernible diffraction pattern except an apparently uniformly illuminated background. For a polycrystalline surface, the diffraction pattern will be semicircular curves of

dots or rings. A single crystal will give a diffraction pattern of a series of horizontal streaks or rows of elongated spots. It is clear that the darker the background, the higher the ordering of the surface.

Using the de Broglie relation and considering the relativity influence, one can easily show that the wavelength λ (in Å) of electrons is related to the accelerating voltage V (in volts) by

$$\lambda = hc[\, eV(2m_0c^2 + eV)\,]^{-1/2}$$
$$= [\, 150/V(1 + 10^{-6}V)\,]^{1/2}$$

where h is the Planck's constant, c is the speed of light, e is the electron charge and m_0 the electron rest mass. For V=10 KV, λ is about 0.12 Å. For a single crystal specimen, from the wavelength λ, the distance from the sample to the screen (about 30.5 cm in our system) and the geometry of the diffraction pattern, one can figure out the planar unit cell, the orientation, and some other features such as the shape and size of the crystal.

Some RHEED patterns from single crystal surfaces may contain dark and light diagonal line pairs that appear to radiate from a central location. They are called Kikuchi patterns (An example of Kikuchi patterns will be shown in Fig. 2.4). The appearance of Kikuchi lines is an indication that the specimen is a reasonably flat single crystal with good lattice perfection. An explanation of Kikuchi patterns will be given in the next section.

A detailed discription and interpretation of different types of RHEED patterns have been given by E. Bauer (1969).

2.2.2 Theory of RHEED

Like all other diffraction phenomena, RHEED can be qualitatively understood from the fundamental theory of the Bragg constructive condition and Laue conditions. The Bragg condition is usually expressed in the crystal space as that the incident and reflected waves should

have an optical path difference equal to $N\lambda$ (N=integer) in order to ensure a constructive interference between them. It can also be represented in the reciprocal space as that

$$\Delta \mathbf{k} = \mathbf{G} \tag{2.2-1}$$

where $\Delta\mathbf{k}=\mathbf{k}-\mathbf{k}_0$ is called the scattering wave vector, $\mathbf{k}_0$ is the incident wave vector and $\mathbf{k}$ is the reflected wave vector, and $\mathbf{G}$ is a reciprocal lattice vector ($x2\pi$). The dot products on both side of Eq.(2.2-1) with $\mathbf{a}$, $\mathbf{b}$, $\mathbf{c}$ respectively gives the Laue conditions:

$$\mathbf{a}_1 \cdot \Delta\mathbf{k} = 2\pi h \tag{2.2-2a}$$

$$\mathbf{a}_2 \cdot \Delta\mathbf{k} = 2\pi k \tag{2.2-2b}$$

$$\mathbf{a}_3 \cdot \Delta\mathbf{k} = 2\pi l \tag{2.2-2c}$$

where $\mathbf{a}_1$, $\mathbf{a}_2$, $\mathbf{a}_3$ are unit vectors in the real space and h, k, l are integers.

When an electron beam is incident on a crystal surface, the constructive interference will occur in those directions where these conditions are met. This situation is conveniently visualized by the Ewald construction in the reciprocal lattice space. Fig. 2.2a shows a two-dimensional representation of such a construction. Let the incident wave vector $\mathbf{k}_0$ end at any one of the reciprocal lattice points O and draw a sphere (called Ewald sphere) of radius $|\mathbf{k}_0|$ around the origin M of $\mathbf{k}_0$ and passing through O. Then any one of other reciprocal lattice points that intersect the sphere will result a diffraction beam pointing from M to that point. In RHEED, since electrons can only penetrate a thin surface layer of the specimen, the reciprocal lattice of a crystal can be represented by an array of rods perpendicular to the crystal surface and located at the reciprocal lattice points of the crystal surface. In the vicinity of the origin O of the reciprocal lattice, where most of the reflected intensity is concentrated, the Ewald sphere in case of RHEED can be approximated by a plane since $|\mathbf{k}_0|$ is large compared to the reciprocal lattice distances (about $2\pi/0.1$Å for the former and about $2\pi/2.5$Å for the later. The diffraction pattern of a crystal surface represents then the plane section through the rods and perpendicular

Fig. 2.2. (a) A two-dimensional representation of Ewald construction in the reciprocal lattice. (b) A schematic representation of Ewald construction and its relation with the diffraction pattern observed in RHEED.

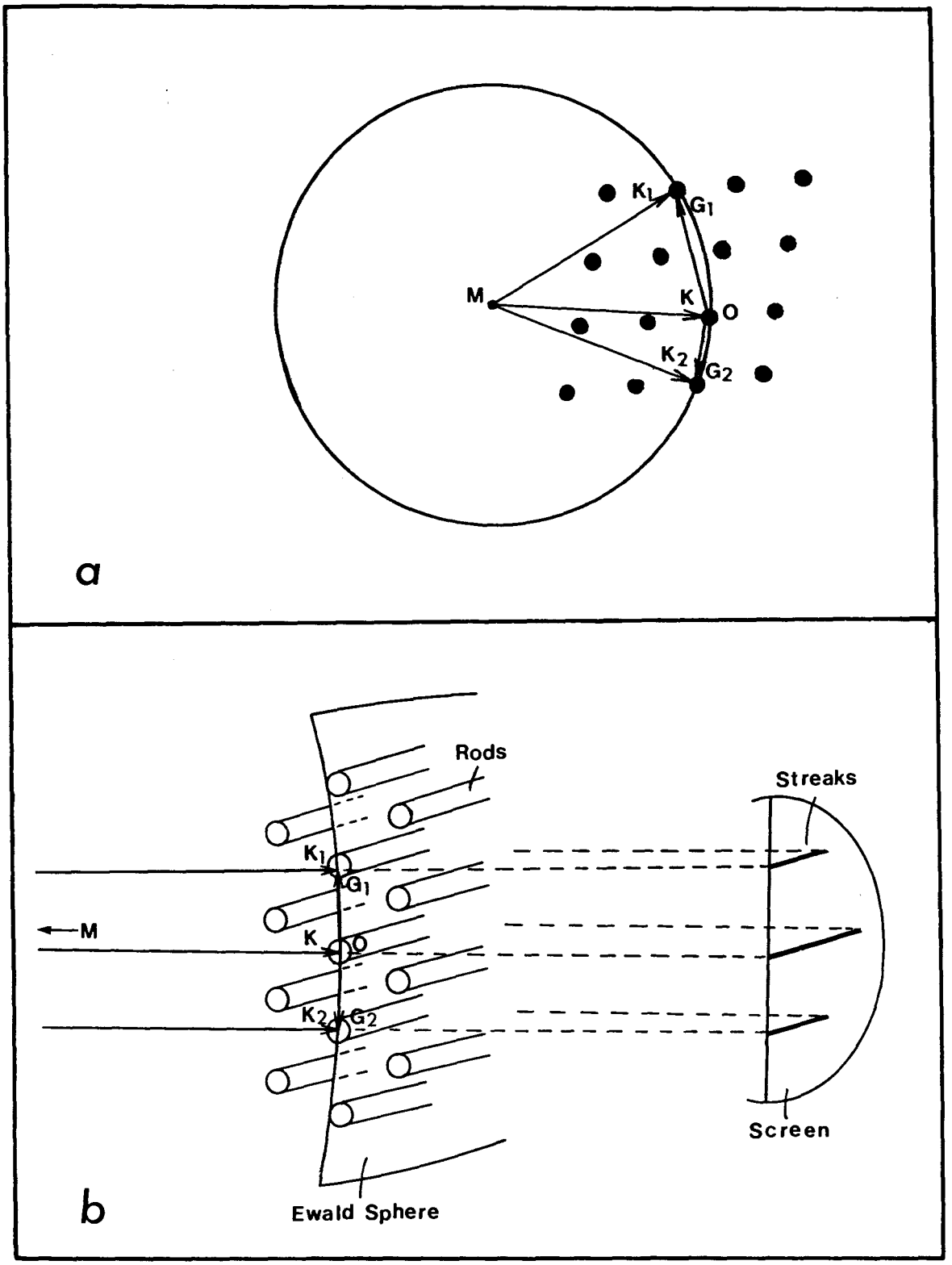
K1
G1
M
K
O
K2
G2
a
Rods
Streaks
K1
G1
M
K
O
K2
G2
Screen
b
Ewald Sphere

to the incident wave and it appears as streaks or elongated spots when the curvature of the sphere is taken into account. Fig. 2.2b shows the Ewald construction and its relationship with the diffraction pattern in RHEED. The rods of the reciprocal lattice and the streaks of the diffraction pattern are shown schematically in the figure. Note that in practice, due to the finite size of the electron beam and the spread of the electron wavelenght, the Ewald sphere is thickened into a spherical shell of thickness which varies with distance from the origin O of the reciprocal lattice.

Using the above simple theory we can qualitatively understand other RHEED patterns. For 3-dimensional crystal lumps which have a size bigger than the electron beam, their reciprocal lattice is also a set of 3-dimensional spots, so that they will contribute spots on the RHEED pattern. However, if the lumps are smaller in size than the spatial dimensions of the electron wave packets of the incident beam, they will not show up in the RHEED pattern except in a form of diffuse background. This is simply because each electron will encounter a mixture of crystal orientations and no constructive interference could happen. An amorphous surface or a polycrystalline surface in which single crystallites are too small will thus result in no Bragg scattering so that they can only contribute diffuse background. This effect is much more pronounced in the electron diffraction since that electron beam is usually well focused and the uncertainty principle thus play an important role in electron diffraction. Also, for electrons the interaction with atoms is much stronger compared with that for x-rays or neutrons. The electron beam dimensions and electron wave packet dimensions may not be the same. Depending on the particular experimental configuration, they may fall in the range from 100Å to 1000Å. But it is hard to determine them accurately (Beeby (1979), Cowley (1981)).

Kikuchi patterns can also be qualitatively understood from the fundamental theory. When electrons emitted from the electron gun strike the sample, they will introduce secondary electrons. The Bragg reflection of the secondary electrons generated in deeper layers of a specimen produces Kikuchi lines. In principle, secondary electrons can travel in any direction, but the

intensity distribution of secondaries depends on the direction of the incident beam and is strongly peaked in the forward direction. That is to say, much more secondaries travel in the forward direction. Those secondaries which leave the crystal without suffering a Bragg reflection will produce a general diffuse background. Those suffering a Bragg reflection will be diffracted and produce Kikuchi lines. A Kikuchi pattern is a superposition of these two effects. For a given set of lattice planes (not parallel to the incident beam), there are always two directions in which the Bragg condition can be satisfied, namely, one forward, the other backward (or less forward) , see Fig. 2.3. In the area near to the forward direction, secondaries produce a strong background on the screen except those areas where the Bragg condition are satisfied. The Bragg reflected secondaries from the backward direction would compensate and fill in these areas but they are much weaker in intensity. The total effect is thus a dark line on the bright background. Similarly, in the area near to the backward (or less forward) direction, secondaries produce a weak background on the screen and the Bragg reflected secondaries from the forward direction are much stronger in intensity, resulting in a bright line on the dark background. Due to the finite size and the divergence of the electron beam, the Kikuchi patterns appear quite often as bands. Fig. 2.4 (a–d) shows a set of RHEED patterns obtained from a Ru single crystal (001) surface. Nice Kikuchi lines can be easily observed. Transition metal dichalcogenides, well known for their layer structure, have almost perfect surfaces. So that their RHEED patterns usually show nice Kikuchi lines. Such patterns of $NbSe_2$ are shown in Fig. 2.4 (e–f). Also shown in Fig. 2.4 are RHEED patterns for a Ag on $NbSe_2$ sample (Fig. 2.4 (g–h)), where both Ag and $NbSe_2$ streaks are present. There are Kikuchi lines as well in Fig. 2.4 (g–h).

Although most of the important features of the RHEED pattern can be qualitatively understood from the above elemental theory, a quantitative analysis of the intensity distributions in the RHEED pattern requires more advanced quantum theory.

In a scattering problem, the wave function $\psi(\mathbf{r})$ of a free electron contains a plane wave and an outgoing spherical wave, and the wave equation can be described by an integral equation

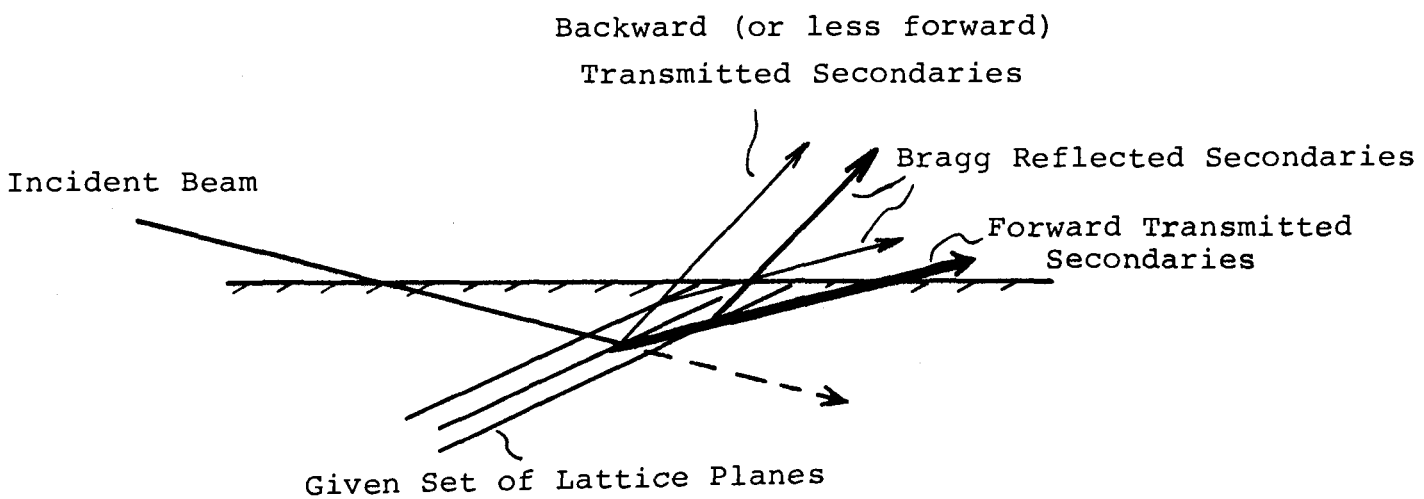

Fig. 2.3. A schematic representation of the formation of Kikuchi lines. Heavier lines represent stronger electron beam intensities.

Fig. 2.4. RHEED patterns showing Kikuchi lines: (a)–(d) a sequence of photos taken from a Ru (001) surface, which were taken by using different electron beam incident angles. (e)–(f) taken from a $NbSe_2$ surface. (g)–(h) taken from a Ag on $NbSe_2$ sample surface, where both Ag and $NbSe_2$ streaks are present.

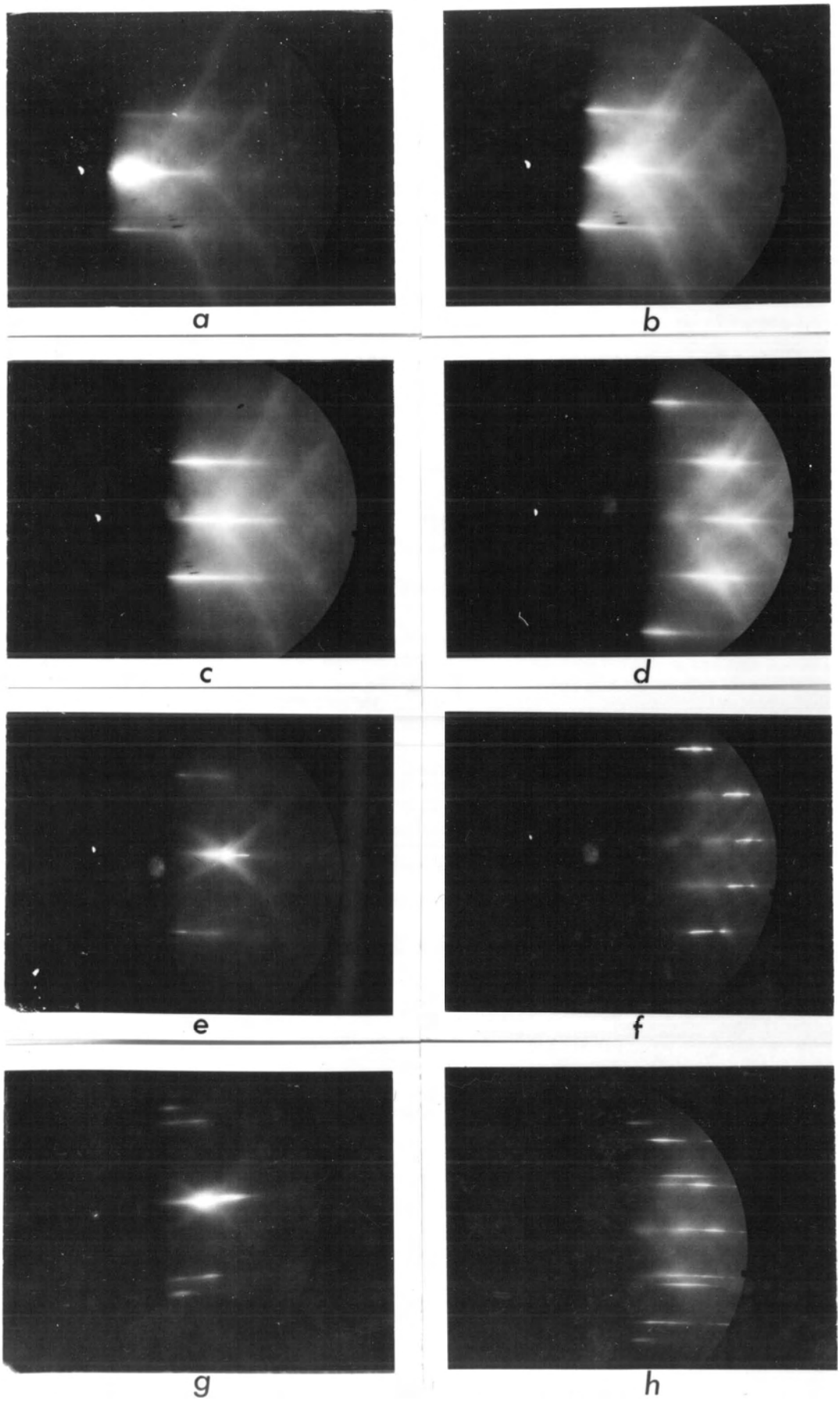
a
b
c
d
e
f
g
h

(Wu and Ohmura (1962)):

$$\psi(\mathbf{r}) = \exp(i\mathbf{k}\cdot\mathbf{r}) - (4\pi)^{-1}\int d\mathbf{r}'U(\mathbf{r}')\psi(\mathbf{r}')\exp(ik|\mathbf{r}-\mathbf{r}'|)|\mathbf{r}-\mathbf{r}'|^{-1} \quad (2.2\text{-}3)$$

where U(r) is an effective potential describing the mutual interaction between the incident wave and the scatterer, and the integration cover the whole scatterer. In electron diffraction, $|\mathbf{r}-\mathbf{r}'|$ is approximated as r since we are interested only in large distance $|\mathbf{r}|$ compared to the scatterer dimension. So that the scattered wave in Eq. (2.2–3) can be considered as a spherical wave with a scattering amplitude

$$f(\mathbf{k}) = -(4\pi)^{-1}\int d\mathbf{r}'U(\mathbf{r}')\psi(\mathbf{r}')\exp(-i\mathbf{k}\cdot\mathbf{r}') \quad (2.2\text{-}4)$$

where f(k) depends on $k=2\pi/\lambda$, θ(the polar angle) and ϕ(the azimuth angle). As long as Eq. (2.2–4) can be evaluated, the intensity distribution in the diffraction pattern can be simply obtained from:

$$I(\theta,\phi)d\Omega = |f(\theta,\phi)|^2 d\Omega \quad (2.2\text{-}5)$$

However, to calculate Eq. (2.2–4) is not easy because the exact form of U(r') and ψ(r') is unknown. Thus simplifying assumptions must be made. The simpest one is the first Born approximation, which assumes that the wave function in the scatterer is approximated by the incident wave, i.e., $\psi(\mathbf{r}')=\exp(i\mathbf{k}_0\cdot\mathbf{r}')$. In RHEED this assumption is reasonably justified because the high electron energy used , but it is still an approximation because the strong interaction between incident electrons and the scatterer compared to the x–ray case. Under this assumption, Eq. (2.2–4) becomes

$$f(\Delta\mathbf{k}) = -(4\pi)^{-1}\int d\mathbf{r}'U(\mathbf{r}')\exp(-i\Delta\mathbf{k}\cdot\mathbf{r}') \quad (2.2\text{-}6)$$

where $\Delta\mathbf{k}=\mathbf{k}-\mathbf{k}_0$, and the scattering potential U(r') is the Fourier transform of the scattering amplitude f(Δk):

$$U(r') = - \int d(\Delta k) f(\Delta k) \exp(i\Delta k \cdot r') \tag{2.2-7}$$

For single crystal scatterers, Eq. (2.2-6) can be written as $f(\Delta k) = S(\Delta k)L(\Delta k)$, where

$$S(\Delta k) = - (4\pi)^{-1} \int_{\text{unit cell}} dr' U(r') \exp(-i\Delta k \cdot r') \tag{2.2-8}$$

is called the structure amplitude, and

$$L(\Delta k) = \Sigma \exp(-i\Delta k \cdot (m_1 a_1 + m_2 a_2 + m_3 a_3)) \tag{2.2-9}$$

is called the lattice amplitude, (the summation is from $m_{1,2,3}=0$ to $m_{1,2,3}=M_{1,2,3}-1$). $\Delta r = m_1 a_1 + m_2 a_2 + m_3 a_3$ (m_{123} =integers) represents the translation displacement of a certain unit cell, and we have assumed that the crystal contains $M_1 \cdot M_2 \cdot M_3$ unit cells. If $\Delta k = G = h b_1 + k b_2 + l b_3$, one can easily obtain from Eq. (2.2-9) that

$$|L(\Delta k)|^2 = \frac{\sin^2(M_1 h/2)\sin^2(M_2 k/2)\sin^2(M_3 l/2)}{\sin^2(h/2)\sin^2(k/2)\sin^2(l/2)} \tag{2.2-10}$$

It is obvious that the conditions for maxima of $|L(\Delta k)|^2$ lead to Laue conditions (2.2-2). Because $|S(\Delta k)|^2$ varies very slowly with Δk as compared to $|L(\Delta k)|^2$, the relative intensity distribution within the intensity regions around the reciprocal lattice points is mainly determined by Eq. (2.2-10). It is easy to show that the width of the diffraction maximun is proportional to 1/M (Kittel, 1976), so that the more atoms involved in the diffraction the narrower the diffraction width. For different intensity regions and different kind of unit cells, the intensities are determined by Eq. (2.2-8), which is proportional to the atomic scattering factor:

$$f_i(\Delta k) = - (4\pi)^{-1} \int_{\text{atom}} d(r) U_i(r) \exp(-i\Delta k \cdot r) \tag{2.2-11}$$

and further assumption about the potential of the atom is needed. For practical use, the atomic scattering factors for electrons can be found in general references, for example,in the "International Tables for X-ray Crystallography, vols. 3 and 4" (Kynoch Press, Bermingham,

1952–1962), and in the books by Vainshtein (1964) and by Heidenreich (1964).

The above theory considers only single scattering and is called the kinematical diffraction theory. Due to the strong interaction of electrons with atoms, multiple scattering is important and a dynamical scattering theory is often needed. The calculation for the dynamical theory is complicated and will not be attempted here. Good references showing the calculation and the computer programs in LEED can be found in the book by Van Hove and Tong (1979).

An elementary and detail description of the Born approximation and scattering calculations can be found in the textbooks by Bransden and Joachain (1983) and by Goldberger and Watson (1964). For more details about RHEED, see Bauer (1969) and Beeby (1979).

2.3 XPS — X-ray Photoelectron Spectroscopy

The technique of X-ray Photoelectron Spectroscopy (XPS) is based on the photoelectric effect. By exposing the specimen to a flux of nearly monoenergetic x-rays and then analyzing the resultant emission of photoelectrons, one can dig out a rich panoply of information on the localized core levels and energetic shifts which relate to chemical bonding and many-electron effects of the material studied. For this reason XPS is also called ESCA, namely, Electron Spectroscopy for Chemical Analysis. The ability of XPS is far beyond just identifying the chemical composition of the sample. By analyzing the shape and intensity of XPS peaks, which correspond to the energy distribution curves of photoelectrons, people can figure out electronic structures of atoms as well as solids. In recent years, there is a lot of interest in the satellite structure in the vicinity of XPS core level peaks. Various models have been suggested to interprete the structure. But before going into details, we introduce briefly the instrument and fundamental concepts in XPS. For simplicity, the instrumental part is presented in Appendix C. The chemical effects on XPS will be discussed together with that on AES in Section 2.4.

2.3.1 The Photoemission Process

When a beam of x-rays strikes the specimen, it causes the photoemission process. This process includes the generation of photoelectrons, the interaction of photoelectrons with other electrons and the escape of photoelectrons from the sample surface. The interactions of photoelectrons with nuclei in XPS are usually not important and can be ignored. Thus the photoemission process can be described by considering only electronic motion. The relativisitic effect can also be ignored in XPS due to the relatively small kinetic energy of photoelectrons (For $E_k = 1000eV$, $v/c = 0.06$, where v is the photoelectron velocity and c the speed of light).

The photoemission process in a solid is a many-body problem. For a system containing N electrons with spatial coordinates $\mathbf{r}_1\mathbf{r}_2\cdots\mathbf{r}_N$ and spin coordinates $\sigma_1\sigma_2\cdots\sigma_N$, the basic excitation process involving absorption of a photon with energy $h\nu$ can be described in the one-electron picture by

$$\begin{array}{lcll} \text{Initial state} & & \text{Final state ion} & \text{Photoelectron} \\ \Psi^i_{tot}(N),\ E^i_{tot}(N) & \overset{h\nu}{\Rightarrow} & \Psi^f_{tot}(N-1,K),\ E^f_{tot}(N-1,K) & + \quad \phi^f(1)\chi^f(1),\ E_k \end{array} \qquad (2.3\text{-}1)$$

where superscripts i and f represent the initial and final state respectively, Ψ_{tot} and E_{tot} represent the wave function and the corresponding total energy of the system, the index K refers to the one-electron orbital from which photoemission occurs, and $\phi^f(1)\chi^f(1)$ describe the orbital and spin motion of the photoelectron which has a kinetic energy of E_k. In Eq. (2.3-1) it is assumed that the coupling between the photoelectron and the (N-1)-electron ion is sufficiently weak so that their final states can be separated. From the above photoemission process, considering energy conservation, one has

$$E^i_{tot}(N) + h\nu = E^f_{tot}(N-1,K) + E_k \qquad (2.3\text{-}2)$$

The binding energy of the electron in orbital K refering to the vacuum level is thus given by

$$E^{V}_{B}(K) = h\nu - E_k = E^{f}_{tot}(N-1,K) - E^{i}_{tot} \qquad (2.3-3)$$

(note that in practical measurements the binding energy is referred to the Fermi level and E_k is measured by the spectrometer, so that $E_B = h\nu - E_k - \phi_A$, where ϕ_A is the spectrometer work function, cf. Fig. C.3 and Appendix C.2.) The wave function Ψ for an N-electron system can be approximated as a single Slater determinant Φ of N orthonormal one-electron spin-orbitals. The total energy E_{tot} is given by $<\Phi|\,H\,|\Phi>$, which can be approximately calculated by using the Hartree-Fock (HF) self-consistent-field method. H is the total Hamiltonian of the system. If one assumes that the ejection of a photoelectron from orbital K does not alter the other one-electron spin-orbitals, then Eq. (2.3-3) will lead to the Koopmans' theorem, which says that the binding energy of the Kth electron is given by the negative of the HF eigenvalue (Koopmans (1934)), and the XPS spectrum would appear as a number of sharp peaks corresponding to the core levels of the atom. Obviously this is too rough a approximation. To account for the rich features of the XPS spectrum, corrections considering the relaxation and correlation effects in the photoemission process have to be made.

2.3.2 The Relaxation and Correlation Effects

In the photoemission process the created core hole in the Kth orbital tends to attract the surrounding electrons through the Coulomb interaction, leading to the "relaxation" of the other one-electron orbitals in the atom. According to Friedel's theory (1954), the photo-excited atom can be treated as an impurity of one unit higher atomic number than the lattice atom. The outgoing photoelectron "sees" these changes and gains an additional energy due to the screening of the core hole, resulting in a lowering of the binding energy. This is the basic idea of atomic relaxation. In a solid, the sudden creation of a hole also tends to polarize the neighboring atoms' electronic charges toward the hole, leading to an additional contribution to the relaxation energy, i.e., the extra-atomic relaxation. For insulating ionic, semiconducting covalent and metallic materials, the detailed mechanisms of the extra-atomic relaxation are somewhat different.

In an ionic solid, there are no covalent bands or itinerant electron states, so that no electronic charge could be readily transfered. The screening of the core hole is mainly provided by polarization of the electronic charge on the neighboring ions. The neighboring ions relax too, but they are too slow to affect the active electron's binding energy. Veal and Paulikas (1983, 1985) have systematically studied 3d transition metal fluorides which are ionic compounds. They explained that the 3d populations associated with different final state screening conditions lead to "satellite" features in the vicinity of the "main" photoelectron peaks. They examined especially the 3s lineshapes of these compounds and concluded that the more intense "main lines" result from local (atomic) 3d screening and the "satellites" at higher binding energy correspond to nonlocal (extra-atomic) screening. And each channel of screening is accompanied by exchange splittings (will be discussed later). Their theoretical calculations (using a relativistic local density atomic code (quoted by Veal and Paulikas as Liberman *et al.* (1965)) to calculate eigenvalues and transition energies for groups of atoms or ions systematically configured to simulate chemical changes) support the above models.

In a semiconducting solid, the extra-atomic relaxation can take place through chemical bonds. The active atom (in which a core hole is created) can polarize the bond and attract the electronic charge density to screen the positive hole. However, a quantitative understanding is still absent for most semiconductors, due to the difficulty of defining the reference energy of binding energies (Shirley, 1978).

In metals, the electrons in the Fermi sea respond to the created hole rather rapidly. It can be assumed (Ley *et al.* (1973)) that a core hole is shielded mostly by an electronic charge placed in states just above the Fermi energy. For transition metals, it was tested by Williams and Lang (1978) that the screening charge is d-like. This screening charge and the core hole form an "excitonic" state. Since the energy of creating the electron-hole pair goes continuously to zero as the momentum of the photoelectron transfers to the pair, the core level XPS lines of most metals have a characteristic skew line shape, tailing off on the high binding energy side. The detailed

lineshapes of metals were first discussed by Doniach and Sunjic (1970) and are presented by the form

$$I(\epsilon) = \frac{\Gamma(1-\alpha)\cos[\pi\alpha/2+(1-\alpha)\tan^{-1}(\epsilon/\gamma)]}{(\epsilon^2+\gamma^2)^{(1-\alpha)/2}} \qquad (2.3\text{-}4)$$

where ϵ is the energy variable relative to the maximum energy in the absence of lifetime broadening, γ is the lifetime of the core hole and α is an asymmetry parameter which is related to the phase shift of the lth partial wave δ by $\alpha = \sum_l (2l+1)(\delta_l/\pi)^2$ according to Nozieres and de Dominicis (1969). When $\alpha = 0$, $I(\epsilon)$ reduces to a Lorentzian lifetime broadening with $2\gamma = \text{FWHM}$, as expected from lifetime effects. In practical analysis one should also add into Eq. (2.3-4) the instrumental resolution parameter.

The overall core level lineshapes of metals are quite different from the insulating case, in which well defined satellite structures are observed. Ni however, is an exception. Ni has always shown strong satellites about 6eV below the main core-level lines. The reason for this exception is not clear. Some authors claimed that it is due to a two-hole state (one in the core level, another in the 3d level created by an Auger process) created in the photoemission process (Hufner and Wertheim (1975)), or due to a resonant photoemission (Guillot *et al.* (1977), Feldkamp and Davis (1979) and Oh *et al.* (1982)). They could not, however, explain the absence of these satellites in other 3d metals. The very narrow and nearly filled 3d band of Ni might make Ni different from other 3d transition metals. For other 3d transition metals, the satellite structure of the core level peaks is not well defined and only the skew line shape is observed. However, by using the Doniach and Sunjic theory, one can sometimes still decompose the skewed peak into two or more peaks.

Like the relaxation effect, which deals with the electronic motion screening the created core hole, the electron correlation effect is also a correlation of electronic motion, but it puts more emphasis on the motion which causes the change of the electronic configuration of the

atom. It becomes quite important in such systems with unpaired electrons where the total angular momenta L and S are different from zero, e.g., transition metals. To study the effects of electron correlation, people usually use the configuration interaction (CI) method, which is basically a variation method with a trial function Φ which is a linear combination of Slater determinants:

$$\Phi = \sum_i c_i \Phi_i \ , \tag{2.3-5}$$

where the coefficients c_i are variational parameters and the various Slater determinants Φ_i correspond to different electronic configurations. A change in the electronic configuration would lead to a change in Φ_i. The intensities of peaks (primary and satellites) due to a certain transition are determined by the matrix elements for that transition, which depend on the configuration interactions. The positions of satellite peaks also depend on the CI's.

Φ and Φ_i in Eq. (2.3-5) can represent either the final state or the initial state. The final-state CI is commonly known as "shake-up" or "shake-off". A shake-up or shake-off process stands for the process that upon the excitation of one photoelectron, another electron is excited to a higher bound state (shake-up) or to an unbound continuum state (shake-off). The initial-state configuration interaction is usually considered less important but in some cases it can affect the intensities of shake-up lines or even create new satellite lines attributable to transitions that would be forbidden without this interaction (Shirley (1978)).

Bagus *et al.* (1973) provided an example of CI calculations on Mn^{2+} and Mn^{3+} ions, from which we can have a more quantitative understanding of the effects of CI on intrashell s-level splittings. By including the CI in their theoretical calculations, they could successfully explain the magnitude of the observed 2s and 3s doublet splittings and the intensity ratio of these splittings. These splittings are due to multiple final states generated in open shell systems and are called multiplet splittings. In the following section we will introduce the concept of XPS multiplet splittings.

2.3.3 XPS Multiplet Splittings

Multiplet splittings arise from the multiple final states, which can occur in any system in which the outer subshell or subshells are only partially occupied. For example, in a Mn^{2+} free ion, the 3d subshell is only half-filled and the ground state can be described in L-S (Russell-Saunders) coupling as $3d^5(^6S)$. Upon ejecting a 3s electron, two final states may be formed, i.e., $3s3d^5(^7S)$ or $3s3d^5(^5S)$, depending upon whether the spin of the remaining 3s electron is parallel or antiparallel to those of the five 3d electrons. These two final states are called a doublet. The energy difference between these two states depends mainly on the 3s-3d exchange integral. This is because the exchange interaction acts only between electrons with parallel spins and thus the ^7S energy will be lowered relative to the ^5S energy due to the 3s-3d exchange. This energy splitting is called the multiplet (doublet in the present case) splitting or exchange splitting. One-electron theory (Van Vleck (1934), Bagus *et al.* (1973)) predicts that the exchange interaction energy (and thus the energy splitting between the doublet) is simply:

$$E=(2S+1)K \tag{2.3-6}$$

where S is the total spin of the unpaired electrons in the valence levels (5/2 in the present case) and K is the 3s-3d exchange integral. And the intensity ratio of the doublet is given by the ratio of multiplicity of the two final states, i.e.,

$$R=[2(S+1/2)+1]/[2(S-1/2)+1]=(S+1)/S \tag{2.3-7}$$

According to this simple model, for the 3s peak in Mn^{2+} this ratio is then 1.4 and E is calculated to be ~13 eV. In the real case of MnF_2, as measured by Kowalczyk *et al.* (1973), the XPS 3s splitting is about 6.5 eV and the intensity ratio is about 2.0. This discrepancy is mainly due to relaxation and configuration interaction effects. Nevertheless, this model should be able to predict the correct trends for changes in spin states, i.e., the more unpaired electrons in the valence levels, the more exchange splitting and the more intense the satellite peak. These trends

have been clearly demonstrated by Clark and Adams (1971) for chromium compounds and by Veal and Paulikas (1985) for Mn and Fe compounds, *etc.*

Veal and Paulikas (1983, 1985) argued that due to the local screening, the 3s exchange splitting in MnF_2 should be based on a d^6 state condition instead of the previously mentioned d^5 state condition. In another word, the 3s hole will be fully screened when the screening electron goes into an empty 3d state. This argument brings the calculated splitting and the intensity ratio closer to the measured value (but the discrepancy still exists). Further more, they argued that the nonlocal screening (i.e., extra-atomic relaxation) (which is unobservable for MnF_2) is a general source of satellite structure in other ionic transition element compounds, such as MnF_3, FeF_2 *etc.* In this case, the exchange splitting is affected by these two screening conditions (local and nonlocal) since the total 3d population is different under these two conditions (adding one d electron for local screening, without adding it for nonlocal screening). This screening mechanism should affect all the core level XPS peaks while the 2p peak is not affected much by the exchange interaction. So that they used 2p peak splitting to predict the screening effect in 3s peaks. This simple model works quite well for 3d-series ionic compounds and as shown later in Chapter 5, it seems also reasonable for explaining the famous 6 eV splitting in Ni 2p and 3s peaks. Unfortunately, life is never so simple. As pointed out by Bagus *et al.* (1973), the transfer of the 3s electron to the 3d shell can be accompanied by the transition of $3p^2$ to 3s3d, yielding the states $3s^23p^43d^7$. This approximate degeneracy results in configuration interactions that reduce the 3s splitting for MnO from 12 eV to 6 eV or less. Generally speaking, the process of electron relaxation and correlation is still far from a complete understanding.

More details about electronic relaxation and correlation effects can be found in a recent review article by Bechstedt (1982).

2.4 AES — Auger Electron Spectroscopy

Whenever a hole is created in an inner shell of a atom, it is unavoidably followed by an Auger process, i.e., an electron from an outer shell will fall down to fill that hole and stimulate another electron to jump out of the atom. This process of radiationless rearrangement of an atom is known as the Auger effect and the electrons being ejected in this process are called Auger electrons. In some cases, the primary hole can also be filled by an electron from the same major atomic shell but a different subshell which has a higher energy, the released energy may also stimulate another electron in an outer shell to eject from the atom. This process is called a Coster-Kronig (C-K) Auger process. Furthermore, if all the energy levels involved are in the same shell as the initial hole, then the process is called a super Coster-Kronig Auger process. Schematical energy level diagrams showing these Auger processes are shown in Fig. 2.5. Obviously, the energy released by filling the initial hole must be sufficient in order to ensure the Auger process to happen. As a result, the C-K and super C-K processes are energetically possible only in limited regions of the periodic table.

Depending on which energy levels are involved, the Auger electron has a certain name. For instance, the Auger electron shown in Fig. 2.5(a) is called a $KL_{23}L_{23}$ Auger electron, where K and L_{23} are x-ray notations in which K, L, M, ····· correspond to the atomic shells of n=1, 2, 3, ····· respectively. Inside each shell different energy levels are numbered in series according to their l and j quantum numbers, e.g., $L_1=2s_{1/2}$, $L_2=2p_{1/2}$, $L_3=2p_{3/2}$, $M_1=3s_{1/2}$, $M_2=3p_{1/2}$, $M_3=3p_{3/2}$, $M_4=3d_{3/2}$ and $M_5=3d_{5/2}$ *etc.* In a $KL_{23}L_{23}$ Auger process, the initial hole is in the K shell and the final two holes are in the L_{23} (or 2p) subshells. Or in general, an ABC Auger process refers to the case where the initial hole is in the A shell and the final two holes are in the B and C shells (or subshells). Since electrons are indistinguishable particles, one should not stress too much on which electron fills the initial hole and which electron jumps out of the atom (Chattarji (1976)).

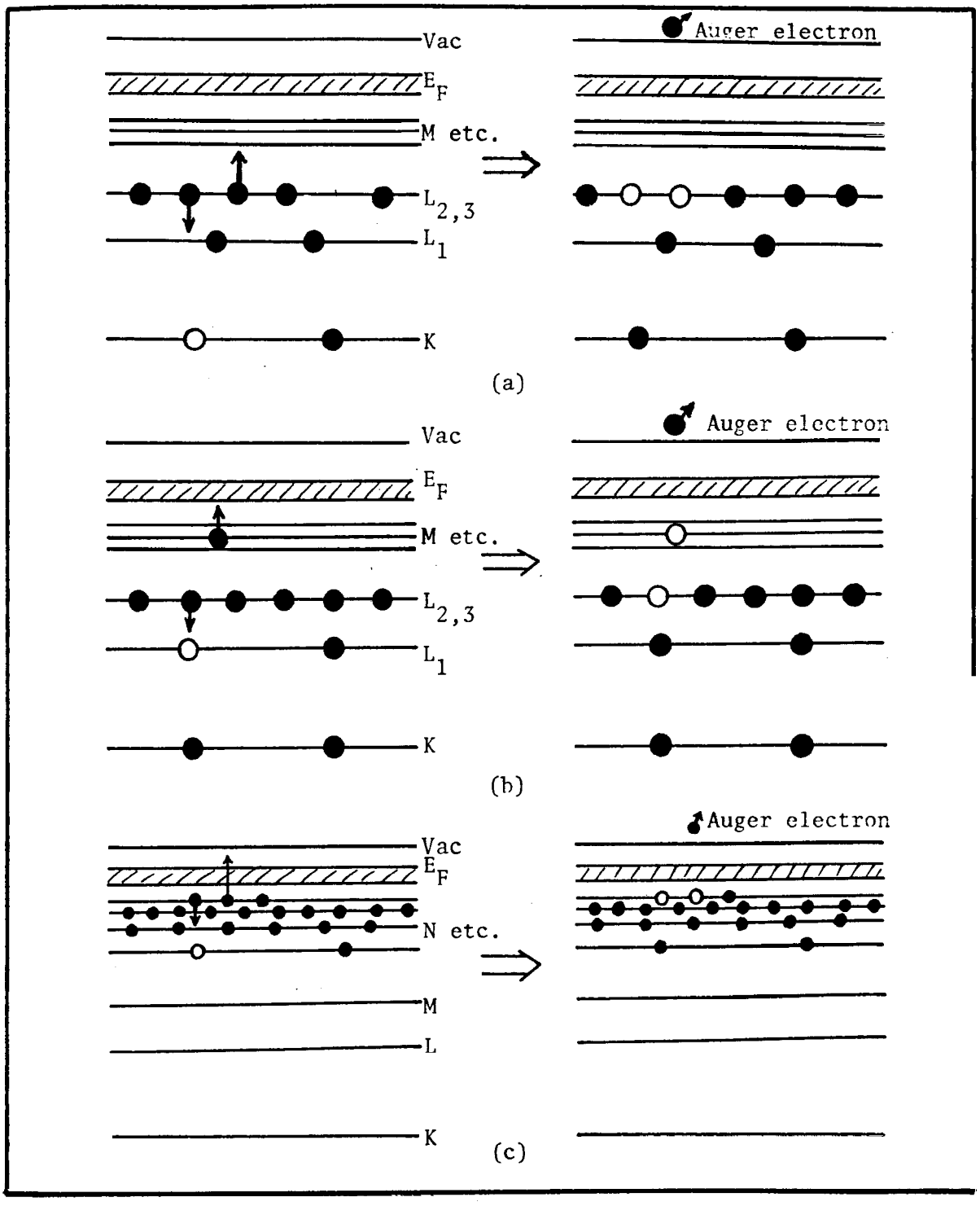

Fig. 2.5. Schematic energy level diagrams showing: (a) the Auger process, (b) the Coster–Kronig Auger process and (c) the super Coster–Kronig Auger process.

AES has been widely used for surface chemical analysis. Information about the chemical changes and the physics involved inside the sample can be obtained by analyzing the Auger peak positions, line shapes and intensities for certain Auger transitions. To understand this, we should know some concept about chemical effects in a solid-state environment.

2.4.1 Chemical Effects in AES and XPS

Chemical effects exist in both AES and XPS for a solid sample. In a solid, the outer electrons form a valence band, which has a certain width. The inner levels retain a quasi-atomic character, but they are shifted in energy compared with the corresponding levels in a free atom. These shifts are called chemical shifts, which depend on the chemical environment. For pure metals the shift can be several eV. For oxides it can be even larger. When a clean metal surface has adsorbed oxygen atoms, there will be a charge transfer from the metal atoms to the oxygen atoms, leading to a decrease of the electron density around the metal atom. The decrease in the electron density is equavelent to a increase in the nuclear charge of the atom. Thus the remaining electrons inside the atom will have a higher binding energy, i.e., their energy levels will be shifted downwards in a schematic energy level diagram. An example is shown in Fig. 2.6 for the case of the Al free atom, Al metal and Al_2O_3 (Bauer, 1972).

The chemical effects have important influence on XPS and AES. From Fig. 2.6 we can easily see that the line positions and line shapes of XPS and AES signals will be changed as we go from free atoms to solids or to oxides. These changes have been observed in our studies and in later chapters we will use them to study the oxidization of Mn overlayers *etc.*

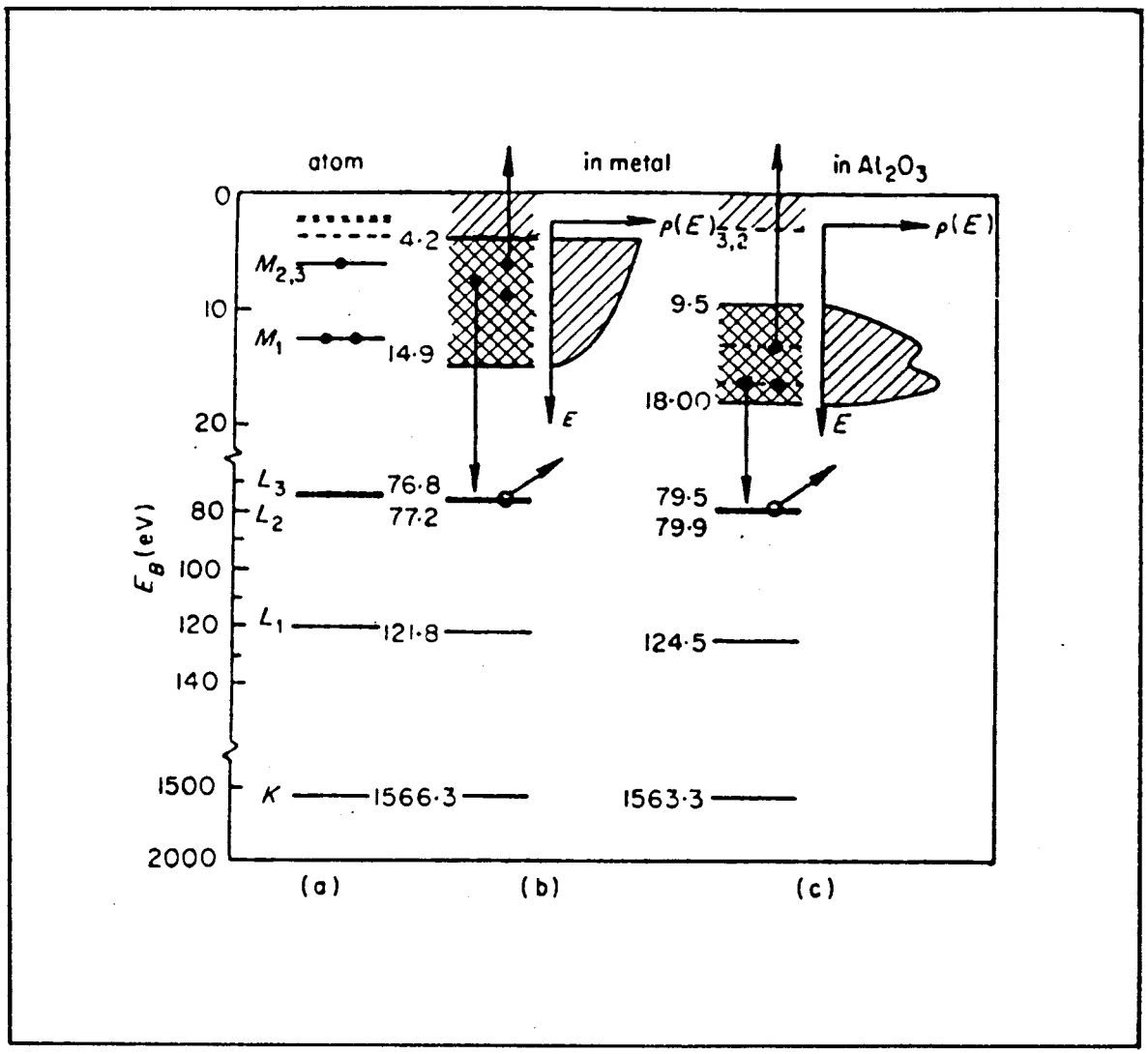

Fig. 2.6. Schematic energy level diagrams for: (a) free Al atoms, (b) Al metals and (c) Al in Al_2O_3. ρ(E), the density of states, is also shown in (b) and (c). These energy diagrams demonstrate the origin of chemical effects for the Al solid and Al oxide compared to the Al atom. (from Bauer (1972))

2.4.2 Auger energies, linewidths and lineshapes

From the simple energy level diagram of Fig. 2.5, one would expect that the energy of an ABC Auger electron would be simply the binding energy of the A level minus the sum of the binding energies of the B and C levels (taking the hole in the A level into account). In the solid state, the effects of the interaction between the two final holes and the relaxation of electrons should be taken into account. The general expression for the Auger energy is thus

$$E(ABC) = E(A)-E(B)-E(C)-F+R \qquad (2.4-1)$$

where F represents the energy of interaction between the holes in the B and C levels in the final state and R represents the relaxation energy due to the two-hole final state, including both the intra-atomic and the extra-atomic relaxation.

The Auger line widths for free atoms are mainly determined by the lifetime of the inner-shell vacancies involved, i.e. by the transition rates for the specified Auger process. For a solid, the Auger peaks are broadened and shifted. For example, an Auger peak in a solid involving two final holes in the valence band (called the valence-type Auger signal), e.g., a LVV Auger transition, would be broadened as twice the width of the valence band. This can be visualized if we consider two extreme cases, one with the two holes at the top and another with the two holes at the bottom of the valence band (cf. Fig. 2.6). However, the interaction between the two holes in the valence band will also play an important role. Because of the screening of other valence electrons of the system, this interaction is not simply the Coulomb integral between the two valence electrons ejected in the Auger process. We will thus call it the effective Coulomb interaction U_{eff}, which is the sum of the last two terms in Eq. (2.4-1). So that Eq. (2.4-1) can be written as:

$$E(ABC) = E(A)-E(B)-E(C)-U_{eff} \qquad (2.4-2)$$

When U_{eff} is larger than two times the band width, the Auger spectra will be quasi-atomic and

the material behaves as if the electrons are localized on a single atom. When U_{eff} is smaller than the bandwidth, the Auger spectra will be quite broad and the material behaves like a free-electron metal with delocalized electrons and weak correlation (Sawatzky, 1977). This fact gives special importance in AES since knowledge of such electron-electron interaction is required for many important problems in the physics of transition metals. We will discuss this in Chapter 6 when we analyze the AES data. Nevertheless, in general the Auger peaks (especially the valence-type peaks) in solids will be broadened and the structure in the density of states function will be reflected in the Auger peaks as long as the Auger electrons come from the valence band. It turns out that in many cases the Auger line shape is a weighted folding of the density of states. The information on the density of states can be derived from the Auger line shape by using suitable deconvolution techniques (Chattarji, 1976).

A lot of effort have been made in recent years to calculate Auger line shapes and intensities. Better understanding of Auger processes has been achieved. But it seems that there is still a long way to go for the theoretical calculation to fit the experimental data. The numerical calculation is tedious and difficult and will not be attempted in the present work.

CHAPTER 3

ANALYSIS OF EPITAXIAL GROWTH OF MN, AGMN AND VMN THIN FILMS

In our experiments, Ru is the most oftenly used substrate. It has a lattice constant of 2.70Å which is close to the closest Mn–Mn distance of Mn_4N (2.733Å, Takei *et al.*, 1960) and larger than the smallest distances in α–Mn (2.24Å, Bradley and Thewlis,1937). Epitaxially grown Mn overlayers might have an expanded lattice spacing and are worth studying.

The MBE growth of Mn, Ag and MnAg on Ru(001) substrate has been extensively studied by using RHEED, AES and XPS analysis. The results we have obtained are convincing and self–consistent.

We found that Mn can grow epitaxially layer by layer on Ru with its first two layers following exactly the Ru hexagonal structure and the Ru inplane lattice spacing. Starting from the third overlayer, Mn atoms always develop a new phase of structure which we call the trimerized structure or 3x1 structure. The Mn growth rate at a Mn source temperature of 606C and a substrate temperature of 60C was determined as about two minutes per layer. The 3x1 structure can grow on a Ru(001) substrate in the substrate temperature range from about –16C to 250C.

Ag can also grow epitaxially on Ru, but it takes its own lattice spacing from the beginning of the growth, while the lateral orientation of Ag overlayers is the same as Ru's. We found that the first two Ag overlayers have a layer by layer growth and then a kind of island–growth follows. At T(Ag)=600C and T(Ru)=R.T.(room temperature), the Ag growth rate was determined as about 7 minutes per layer.

Ag and Mn can grow together epitaxially with up to 10% Ag in Mn on Ru or with up to 35% Mn in Ag on Ag grown on Ru substrate. The compositions of the grown Mn–Ag alloys

were determined by AES and XPS analysis. The results are consistent with what would be expected from the Ag and Mn growth rates.

$NbSe_2$ substrates were also used to check the Mn and Ag growth. It was found that Mn sticks on $NbSe_2$ quite well. RHEED patterns showed that Mn grows on $NbSe_2$ (at room temperature) amorphously. After a Mn growth of 2.25 ± 0.08 minutes at T(Mn)=606C and $T(NbSe_2)$=R.T., $NbSe_2$ RHEED streaks totally disappeared and only an amorphous background was observed. The disappearence of the substrate RHEED features is taken as an indication of monolayer coverage of deposits, similar to the LEED case (Powell (1974)). The above observation agrees with the AES and XPS analysis of the Mn growth rate. Ag does not grow on $NbSe_2$ layer-by-layer at room temperature. It forms its own RHEED streaks right in the beginning of the deposition and $NbSe_2$ streaks did not disappear even after a deposition of five layers (on average) of Ag. Such RHEED patterns showing the coexistence of Ag and $Nbse_2$ streaks have been shown in Fig. 2.4 (g-h). This indicates the formation of Ag islands, or in other words, Ag does not "wet" $NbSe_2$. On the other hand, in case of Ag on Ru, Ru streaks disappeared after a deposition time which corresponds to the completion of a monolayer of Ag, according to AES analysis.

The theory of epitaxial growth by van der Merwe (1964, 1975) has been applied to analyze the growth of Mn and Ag on Ru. A good agreement between the theory and our experiments was obtained for the case of Mn on Ru. However, for the case of Ag on Ru, the fact that Ag has its own lattice spacing right in its first overlayer can not be explained by the theory.

In the following sections, the details of the above conclusions are discussed.

3.1 Sample Preparation and RHEED Analysis of Mn growths

A Ru rod was spark-cut into Ru(001) disks about 8mm in diameter and about 1.5mm thick. These disks consist of large (about 6x2 mm^2) grains within ± 2 degrees of the (001) orientation as shown by x-ray diffraction. The Ru disks were mechanically polished in a conventional manner using diamond compound polishing slurries with grit sizes decreasing to 1μm. The polished disks were cleaned in sequence of trichlorone - acetone - methanal ultrasonic baths. Another cleaning solvent—Tape Path Cleaner TX113 (The Texwipe Company, U.S.A.) was also used with success.

To mount the Ru disk on a Mo sample holder in a way such that the RHEED pattern can be easily observed in any direction, the following method was used. A slit was cut on the side of the Ru disk. A Mo wire and a 3%Re-W spring hold the Ru disk firmly in a channel cut in the Mo sample holder, as shown in Fig. 3.1 (a-b). In this way the sample and the sample holder can have a good electrical and thermal contact and also nothing is blocking the electron beam in RHEED. Another convienent way to mount the sample is using two clamps to hold the sample onto the sample holder, as shown in Fig. 3.1 (c-d). $NbSe_2$ samples were mounted in this way. Vanadium plate samples were also mounted in this way, but two edges of the V plate were cut down below the plate surface so that the clamps would not block the RHEED pattern. To mount an iron disc sample and in order to have a uniform stress on the sample, a Mo foil with a hole in it was used to replace the two clamps. The edge of the iron disc was spark-cut into steps (not shown).

Samples were usually outgased in the introduction chamber overnight at R.T. or heated to 120-150C for half an hour before entering the analysis chamber. Then in the analysis chamber they were further cleaned by Ar^+ sputtering with an Ar pressure of $5x10^{-5}$ torr. Following the ion sputtering, they were annealed at a temperature up to 750C and then cooled down naturally to the desired substrate temperature. For a fresh mechanically polished sample, several cycles of

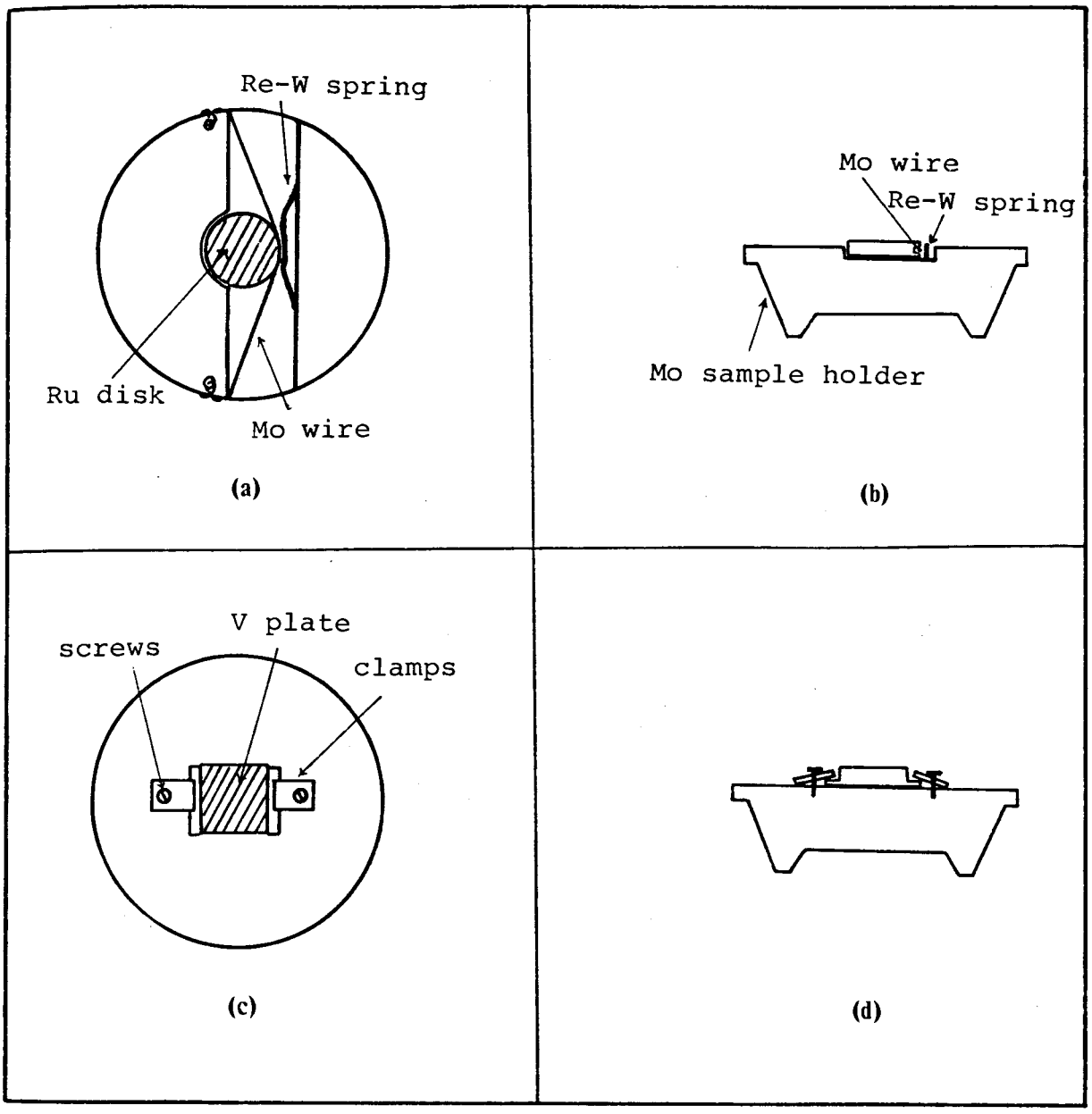

Fig. 3.1. Schematic diagrams showing the methods of mounting samples. (a) and (b): mounting a Ru disk, (c) and (d): mounting a V plate. (a) and (c) are top views. (b) and (d) are side views.

sputtering-annealing were usually used. Ru samples subjected to these treatments showed little oxygen and carbon in AES. No other impurities could be detected. The O(510eV) AES intensity was about 0.005 of Ru(273eV) AES intensity which corresponds to about 0.5% monolayer of oxygen. The carbon contaimination was about 1% monolayer as determined by the ratio of the upper part to the lower part of the Ru(273eV) AES peak.

The deposition of Mn, Ag *etc.* were carried out immediately after the Ru substrate was cooled down to the desired temperature (usually 60C for Mn growth and R.T. for Ag growth). The effusion cells were heated to the desired evaporation temperature about half an hour before the deposition in order for them to reach the equilibrium. In growth of Mn-Ag, the Mn effusion cell temperature was usually set to 606C (thermal couple reading), while the Ag temperature was varied according to the required deposition rate.

During the growth, RHEED was occasionally, sometimes continuously, watched to monitor the growth. For Mn growth at T(Mn)=606C, it was observed that in the first five minutes of deposition the RHEED pattern does not change appreciably from that of the Ru substrate (Fig. 3.2 (a-b)). After about 5.2 ± 0.1 minutes the RHEED pattern from a Ru[120] diffraction (i.e. the electron beam parallel to Ru[120]) shows the appearance of additional diffraction streaks which developed to almost equal intensities to old streaks after about 10 minutes' growth. As derived from AES studies (shown later), the Mn growth rate was about 2.25 minutes per layer. The first five minutes of Mn growth thus corresponds to the completion of the second layer and the start of the third layer of Mn. The RHEED patterns of the Ru substrate and a 12 minutes growth of Mn on Ru are shown in Fig. 3.2. Mn growth up to an hour at T(Mn)=606C showed similar RHEED patterns as Fig. 3.2 (c-d). Growth longer than an hour has not been attemped.

From the theory of RHEED (see section 2.2.3) one can figure out the behavior of Mn overlayers. In the first five minutes' growth, Mn atoms could easily find the A and B sites in the Ru hexagonal lattice. The interfacial energy could overcome the misfit between Mn and Ru (see

Fig. 3.2. RHEED patterns for a Ru (001) surface before the Mn growth ((a) and (b)) and after a 12 minutes Mn growth ((c) and (d)). The electron beam is parallel to Ru [120] in (a) and (c), and to Ru [110] in (b) and (d).

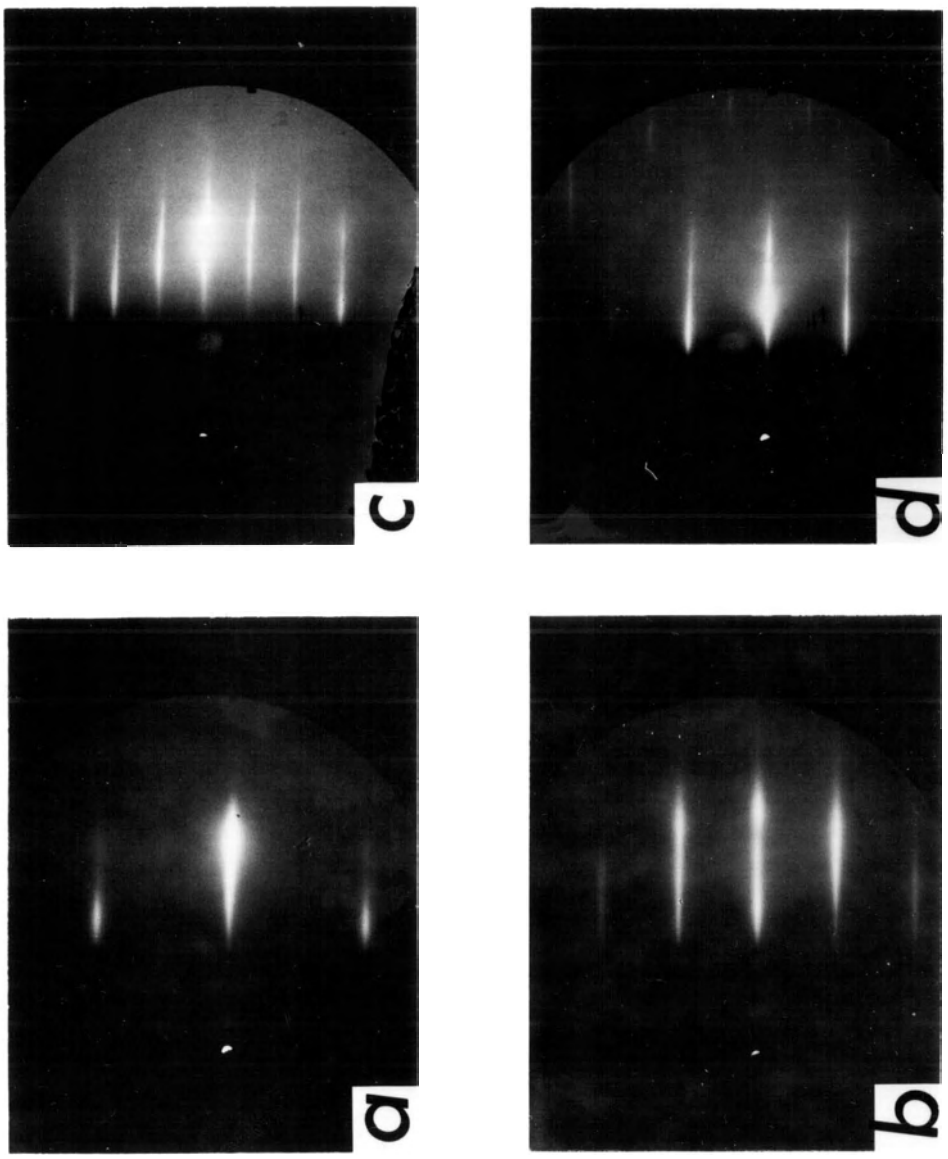
c
d
a
b

below) so that the Mn overlayers could follow the Ru structure and showed no noticeable change in RHEED patterns. The RHEED patterns for thicker Mn overlayers (Fig. 3.2 (c–d)) correspond to a new phase of Mn which has a new periodicity compared to the first two Mn overlayers. Careful observations of RHEED patterns comfirmed that the 2-dimensional reciprocal lattice of this new phase still has a hexagonal symmetry but the number density of streaks increased by a factor of three. By this reason we call it the 3x1 structure. This means that in the real space, Mn atoms have been trimerized and the number density of these trimers is three times less compared to the Ru(001) density. The simplest way to visualize the trimerization is to assume that the number of atoms per layer in the new phase is the same as that of the Ru substrate and every group of three Mn atoms simply move closer to each other forming a new unit. However, RHEED intensity calculations ultilizing Eq.(2.2–8) along [120] direction could not give equal intensities for each streaks in the RHEED pattern (Fig. 3.2c). Morever, it is also hard to explain how this structure would propagate from one layer to the next without Mn atoms falling into the large holes in the lower layer. In an alternative way, we assume that in the new phase Mn density has been increased in the ratio of four to three compared to the substrate density and then every four Mn atoms form a tetrahedron unit. These tetrahedrons thus correspond to the observed 3x1 structure. One can make a closed packed structure with four atoms in the area of three by choosing the lattice parameter to be decreased by 0.866 and rotating the axes by 30° (90°) with respect to the substrate. The stacking started from the third Mn overlayer would naturally lead to a modulation of this structure, i.e., three Mn atoms in a unit cell would move toward the fourth and most likely raising the fourth atom somewhat out of the plane to form a tetrahedron at each corner of the 3x1 unit cell. Thus these tetrahedrons as new subgroup units form a hexagonal lattice with a new parameter of $\sqrt{3}a$, where a is the Ru a spacing. This modulation would produce not only the observed streaks but also a almost equal intensity for each streak. Such a model is illustrated in Fig. 3.3. By assuming that Mn atoms are hard-balls with equal diameter and that neighboring balls touch each other, one can easily find out that the distance between neighboring Mn atoms is about 2.39Å and the central atoms of the tetrahedrons

Fig. 3.3. A proposed model for the trimerized Mn structure showing: (a) expanded Mn atoms, (b) tetrahedrons on top of the expanded Mn atoms, (c) a single tetrahedron on the expanded Mn atoms and (d) one way of stacking of the tetrahedrons, where the tetrahedrons directly pile up.

b
d
a
c

are about 0.47Å out of the plane. The stacking of the fourth Mn overlayer would still follow this kind of structures. These tetrahedron layers may directly pile up with the central atoms of the tetrahedrons aligned in straight lines, as shown in Fig. 3.3d. Or they may also pile up in a different way, namely, in the fourth layer the central atoms of the tetrahedrons might be pulled down to the valley in the third Mn overlayer. Then for the fifth Mn overlayer, the central atom of the tetrahedron would be again raised, and so on. This structure can thus be built up layer by layer in a close packed fashion.

This 3x1 structure of Mn was stable below 420C as observed by heating the sample and watching the RHEED pattern. Above 450C, Mn started to clump and the RHEED pattern showed that the 3x1 streaks disappeared and were replaced by some faceted spots. This is an indication of clumping of Mn atoms. Further increase of the temperature up to 800C, we could see from the UTI mass spectrometer that Mn line grew to a maximum and then decreased gradually, a clear indication of Mn evaporation. RHEED pattern showed only the Ru streaks, but XPS measurement showed that small Mn peaks were still there. These remaining Mn atoms (correspond to about 1/4 monolayer) might have hidden in the grooves of the Ru surface and thus were bound strongly there.

For the substrate temperature dependence of Mn growth, it was observed that we could grow Mn 3x1 structure in the substrate temperature range from about -16C to 250C. Mn growth at a substrate temperature of 300C showed no 3x1 structure but weak streaks at the position of Ru streaks with a diffuse background. From the ratios of the XPS Mn signal to Ru signal, it was noted that the Mn sticking coefficient decreases as the substrate temperature increases. The growth rate of Mn at T(Ru)=250C decreased to about 70% of that at T(Ru)=60C and the growth rate at T(Ru)=300C decreased to one half of that at T(Ru)=60C. This is mainly due to the reevaporation of Mn atoms from the substrate into the vacuum. The difference between the growth at -16C and that at 60C is about 15%.

Much higher deposition rate of Mn on Ru was also tried. At T(Mn)=700C and T(Ru)=60C the growth rate as determined by AES increased by a factor of about 20 compared to that at T(Mn)=606C and T(Ru)=60C, or in other words, the growth rate was about 20 layers per minute. For a total growth of 50 layers, the RHEED still showed good 3x1 patterns, but the background was more diffuse compared with the low growth-rate case, indicating some disorder occured during the growth.

Mn can also grow epitaxially on a bcc Fe(100) substrate. As observed from RHEED, the grown Mn had the same pattern as Fe for over 15 layers of Mn. (Thicker Mn films have not been tried.) The growth condition was: T(Mn)=606C, T(Fe)=R.T. AES and XPS showed that the Fe substrate was totally and uniformly covered by Mn.

For AgMn alloy on Ru(001) substrate, RHEED showed that for up to 35% at. Mn, the codeposited AgMn films still have clear pattern, the same as a Ag pattern. This suggests that Mn might have a substitutive position in a Ag fcc lattice. For VMn alloys on Ru, the RHEED pattern showed broad broken streaks with two phases and diffuse background.(The additional streaks are quite weak in intensity.) It is not caused by the Ru substrate, since AES measurements could not detect Ru signals after the VMn growth. The broken streaks are due to some 3-dimensional features of the surface. The two phases presumably are due to some additional symmetry introduced by Mn atoms. Since the additional streaks are quite weak and the background is quite strong, we will not analyze the possible structure of VMn. Most likely the possible structure is not well defined. The substrate temperature was room temperature for both AgMn and VMn alloys.

3.2 AES and XPS Analysis of MBE growths

AES and XPS have been successfully used to analyze the thin film growth, including the type of growth (i.e., layer by layer growth or 3-dimensional growth), the growth rate and the composition of binary alloy overlayers. In this section a brief introduction of each method and the results of the analysis will be presented.

AES and XPS analysis of MBE growth is based on the fact that the created Auger or photoelectrons undergo inelastic scattering when they travel in a solid and experience an exponential decay $\exp(-l/\lambda)$, where l is the travelling distance of electrons inside the sample and λ is the inelastic mean free path. By definition, λ is the mean distance electrons traveled before they decay to e^{-1} of the initial intensity. Obviously, λ depends on the electron energy E. The mean free path lengths are very high at low energies, but fall to 1-8Å in the energy range 30-100eV and then rise again as E increases further. However, λ is not that sensitive to the element of atoms in which electrons travel. The relationship between λ and E can be approximately represented by a so-called universal curve in the energy range greater than 100eV (from PHI's XPS handbook):

$$\lambda = 0.105E^{3/4} \qquad (3.2\text{-}1)$$

where λ is in Å and E in eV. More recently, Seah and Dench (1979) considered further the dependence of λ on the atom size a and obtained for the whole energy range that

$$\lambda = 538aE^{-2} + 0.13a^{2/3}E^{1/2} \qquad (3.2\text{-}2)$$

where λ and a are in Å and E in eV referred to the Fermi level. The atom size a is derived from $\rho Na^3 = A$, where ρ is the density of the element (in g/cm^3), N is Avogadro's number and A the atomic weight of the element. Note that in many cases Eq.(3.2-1) and Eq.(3.2-2) are rough approximations. Eq.(3.2-2), for example, has a root-mean-square scatter factor of 1.36 for the

energy range greater than 150eV.

Now we consider the deposition process. Using a hard-ball atomic model and the concept of inelastic mean free path, we can show (Appendix D.2) that for a layer by layer growth, an AES (XPS) intensity vs. thickness curve would follow the exponential law and have a linear dependence showing "breaks" with the first break corresponds to the completion of the first monolayer, the second break to the second monolayer, of the deposit, *etc.*. The ratio of slopes s_2/s_1 would be $\exp(-l_0/\lambda)$, where l_0 is the path the electron traveled in a single overlayer and λ the inelastic mean free path. And for the ratio of slopes s_3/s_1 we have $s_3/s_1=(s_2/s_1)^2$.

We have carried out AES (XPS) intensity vs. thickness (or deposition time) measurements for Mn on Ru and Ag on Ru systems. After Ru substrate was cleaned by Ar^+ sputtering and annealing, Mn (Ag) was grown on Ru for certain interval of time and then both Mn (Ag) and Ru AES (XPS) signals were measured and recorded on an X-Y recorder. Meantime, the Mn (Ag) flux was measured by UTI mass analyzer. The UTI readings were used to modify the deposition time. This "grow and measure" procedure was repeated until sufficient data points were obtained.

Fig. 3.4 shows the AES result of Mn on Ru growth at T(Mn)=615C and T(Ru)=60C. Two breaks can be easily identified in each curve (shown by small arrows in Fig. 3.4a). For Ru 231eV curve, the ratio of slopes are measured as follows: $s_2/s_1=0.67$, $s_3/s_1=0.42$. We can see that s_3/s_1 is very close to $(s_2/s_1)^2$ $(=0.47)$. For Mn 589eV curve, $s_2/s_1=0.79$, $s_3/s_1=0.61$ which is also very close to $(s_2/s_1)^2$ $(=0.62)$. From the position of breaks the Mn growth rate on Ru at T(Mn)=615C and T(Ru)=60C was about 1.75 minutes per layer. From the slope of the curves we obtained $\lambda=6.8$Å for E=231eV and $\lambda=11.5$Å for E=589eV. The least square fit of the data with exponential functions is shown in Fig. 3.4b. The exponential curve fits the data quite well in the whole data range for both curves. This is a strong evidence for the layer by layer growth of Mn on Ru. If we assume the thickness of one monolayer of Mn is 2.0Å and consider the

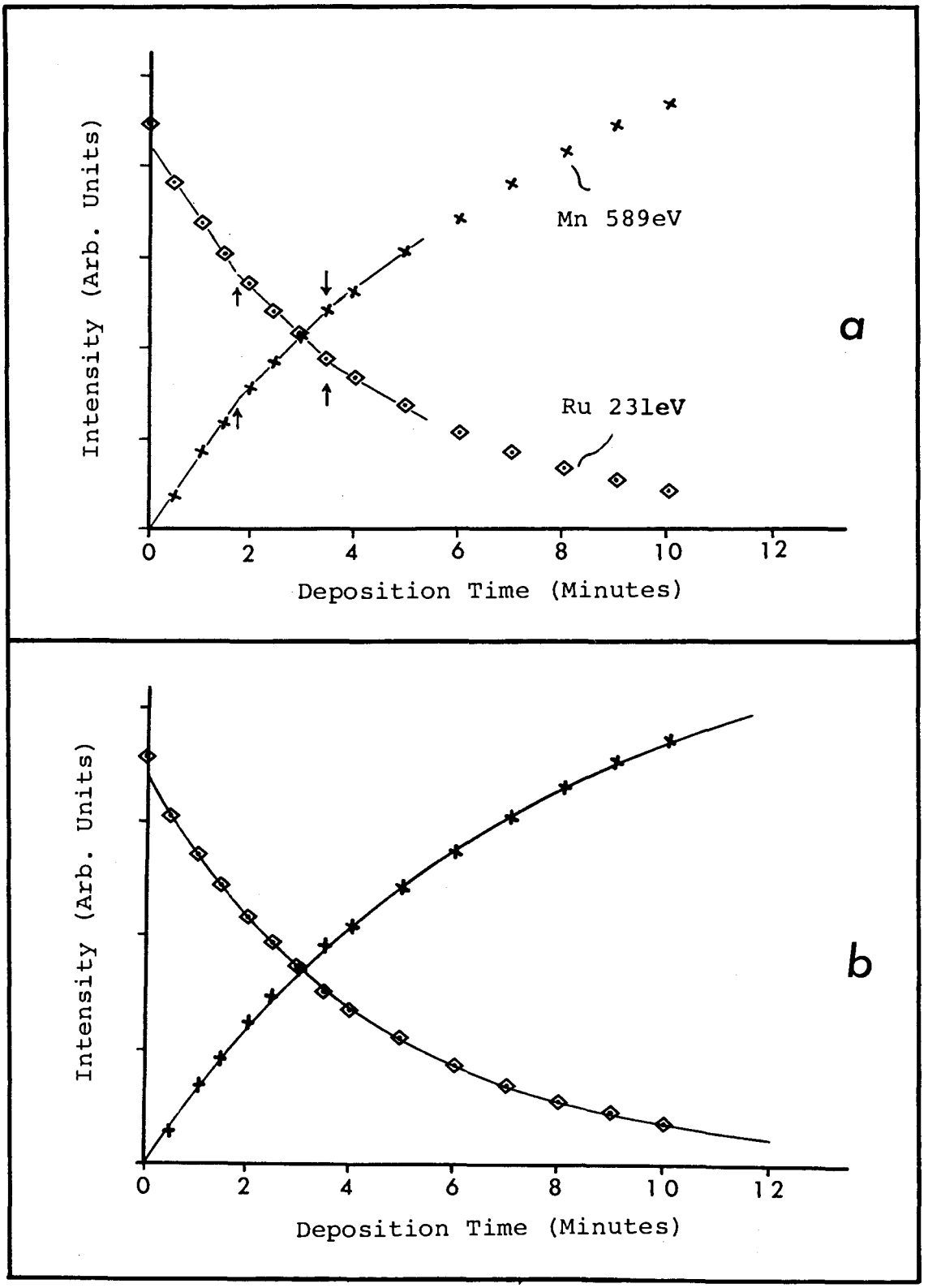

Fig. 3.4. AES intensity vs. deposition time measurements for Mn on Ru. (a) shows two breaks in each data set. (b) shows the exponential least square fit of the data.

analyzer geometry correction cos42°, the exponents derived from the least square fitting together with the estimation of the growth rate (1.75 minutes per layer) would lead to a λ of 6.8Å for Ru 231eV and 11.8Å for Mn 589eV. These λ values are very close to the universal curve (6.2Å and 12.5Å from Eq.(3.2-1), and 6.8Å and 11.0Å from Eq.(3.2-2)).

This experiment was repeated for three times and similar results were obtained. The same measurement was also carried out at T(Mn)=606C and T(Ru)=60C. Although the data obtained at this temperature (not shown) are not as neat as that shown in Fig. 3.4, they also fit the exponential curve quite well. Similar analysis leads to a deposition rate of 2.3± 0.2 minutes per layer.

It was noted that in the above AES measurements, oxygen Auger signal developed continuously. For the data shown in Fig. 3.4, oxygen signal was accumulated to as high as the Mn signal. This corresponds to about 20% of oxygen in the Mn overlayer if we assume that oxygen atoms were mixed with Mn atoms (note however, according to our angular resolved measurement, there was more oxygen on the surface than in the bulk). Due to the presence of oxygen, the RHEED patterns as seen at the end of measurement were always very diffuse and unclear. This increase in oxygen contamination is mainly due to the fact that Mn is very active to oxygen. It is also due to an electron beam stimulated oxidation process (see, e.g., Coad *et al.* (1970), Ranke and Jacobi (1975)). The very intense electron beam we used (e.g., 40 μA beam current and ~0.4x0.4 mm^2 beam size, i.e., about 25 mA/cm^2) would have increased the temperature in the analysing area and would cause more CO and CO_2 to decompose. (For a 2 keV electron beam, the dissipation energy at the surface would be 50 W/cm^2.) All these effects lead to an increased speed of oxidation. Despite the presence of oxygen, the nice breaks observed in the Auger intensity vs. deposition time measurements indicate that we still had a layer by layer growth of Mn on Ru. The additional oxygen atoms made the Ru signal decay faster and the Mn signal increase slower. As a result, the λ derived from the Ru 231eV curve should be bigger than the actual value and the λ derived from the Mn 589eV curve should be

smaller than the actual value. Considering the results of the experiments described below, the actual λ values are very likely as 5.8 ± 0.5Å for Ru 231eV and 12.7 ± 0.5Å for Mn 589eV signals.

To avoid the accumulation of oxygen in Mn overlayers, we have carried out the above measurement in another way, namely, we started each step of growth from a clean Ru surface, i.e., we resputtered and reannealed the sample after each step of measurement. Results of such a measurement are shown in Fig. 3.5a. The Mn source temperature was 606C and the Ru substrate temperature was about 60C. Only the exponential fit was tried due to the difficulty in obtaining enough data points to see "breaks" in the curve. The exponents obtained from the least square fit gave a Mn growth rate of 2.2 ± 0.1 minutes per layer if we take the λ values of 5.8Å for Ru 231eV and 12.7Å for Mn 589eV. This is in good agreement with the previous results.

For comparison, Mn was deposited onto the layer compound $NbSe_2$ at T(Mn)=606C and T($NbSe_2$)=R.T. RHEED patterns of $NbSe_2$ showed very nice streaks (see Fig. 2.4 (e–f)). Upon deposition of Mn, the $NbSe_2$ streaks became weaker and weaker until finally they totally disappeared in the diffuse background after about two minutes and 15 seconds of deposition. This phenomenon has been observed for five times at the same temperature setting and the deposition time needed for the disappearence of $NbSe_2$ streaks was in the range of 2 minutes 10 seconds to 2 minutes 20 seconds. This is a good indication that the Mn growth rate is 2.25 ± 0.08 minutes per layer at T(Mn)=606C, in good agreement with the results of Auger analysis. It also seems to us that the sticking coefficients are very close for Mn on Ru and Mn on $NbSe_2$.

The above determined Mn growth rate later on was used to estimate the growth of Mn on the Fe substrate. For T(Mn)=606C and T(Fe)=R.T., after ~20 minutes growth of Mn, the Fe 703eV AES peak totally disappeared, indicating the thorough coverage of Mn. Considering the observation of RHEED, which showed still clear streaks with a Fe lattice spacing, we thus know that we have a layer by layer epitaxial growth of Mn on Fe(100).

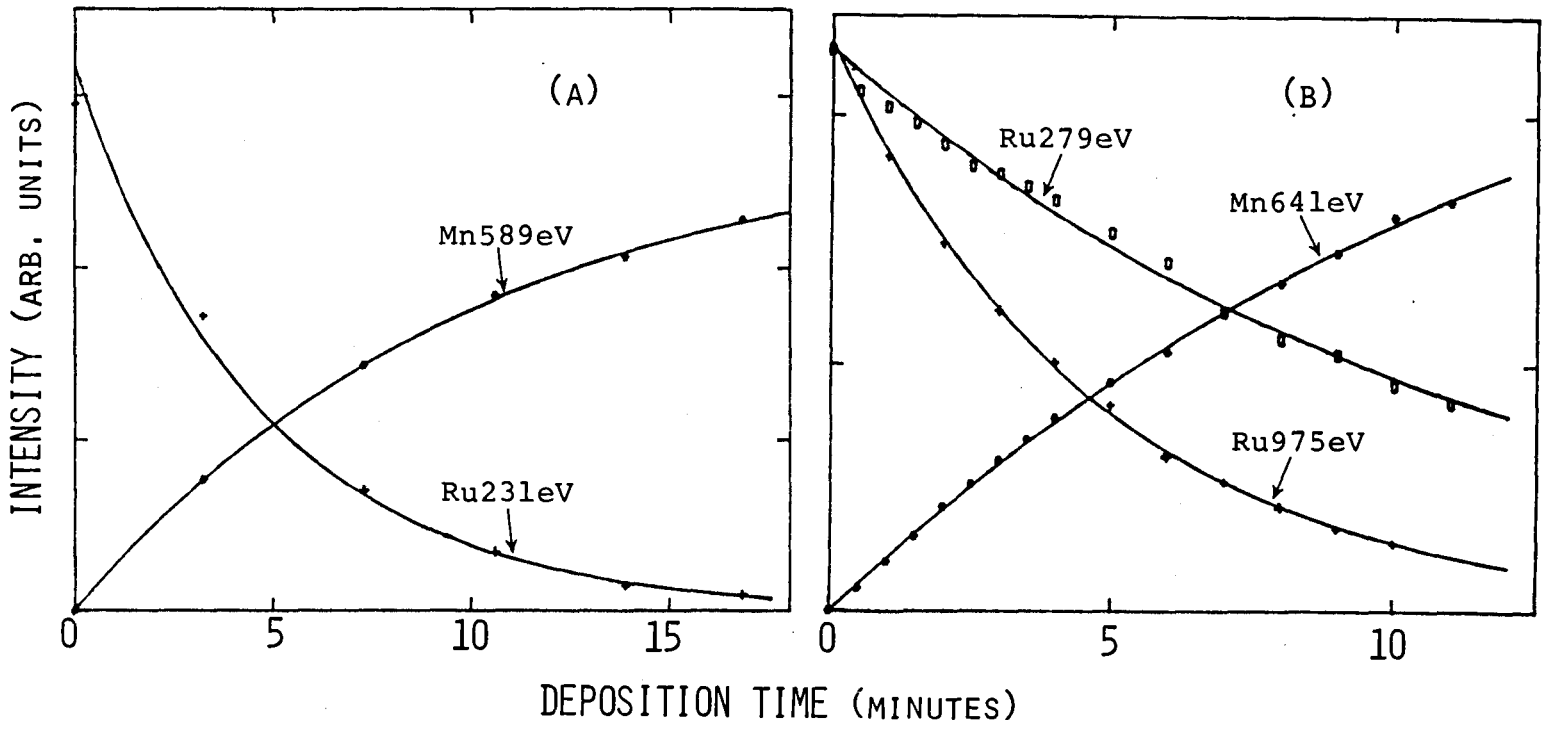

Fig. 3.5. AES and XPS intensity vs. deposition time measurements for Mn on RU. (a) AES intensity vs. deposition time, where each step of deposition was started from a freshly prepared Ru substrate, (b) XPS intensity vs. deposition time, the exponential least square fit is shown by the solid lines.

XPS was also used to determine the Mn growth rate. Mn was deposited in steps (of every half minute up to a total of four minutes and then every one minute up to 11 minutes) onto Ru substrate at T(Mn)=606C and T(Ru)=60C. The advantage of XPS is that the x-ray beam does not stimulate oxidation (note that Mn still seizes the residual oxygen in the system). The disadvantage is the difficulty in aligning the specimen and in keeping the measuring conditions identical for each measurement, although care has been taken to keep the sample position as identical as possible. In the XPS measurement, the Ru 279eV, Ru 975eV and Mn 641eV (all in binding energies, which correspond to approximately 969eV, 273eV and 607eV kinetic energies respectively) peaks were used. Since we could not make sure that the sensitivity for each measurement is the same, a background level was also recorded and later on was used to correct the data. The results after such a background correction together with the exponential least square fit are shown in Fig. 3.5b. The nice exponential fits of data indicate a layer by layer growth. Note also that the lower kinetic energy curve (Ru 975ev) decays much faster than the higher kinetic energy curve (Ru 279eV). This is also an indication of uniform Mn coverage. Quantitative analysis however is difficulty to make. This is mainly because we were using a cylindric mirror analyzer. During the XPS measurement, the sample was tilted with respect to the axes of the analyzer. Photoelectrons detected by the analyzer would have different paths inside the sample depending on their emerging angle. Furthermore, the distribution of photoelectrons is direction dependent. More electrons would appear in the forward direction than in the backward direction of the x-ray beam. To determine exactly the distribution function obviously is not an easy job. For this reason we did not try to analyse quantitatively the XPS data. Many other laboratories have hemisphere energy analyzer in which electrons (photoelectrons) enter into the analyzer in a narrow, well-defined angle along the axes of the analyzer instead of along the 42° cone in the cylindric mirror analyzer. In that case, XPS was quite successfully used for quantitative analysis.

The AES intensity vs. deposition time measurements were also carried out for Ag growth on Ru. The result for a growth at T(Ag)=600C and T(Ru)=60C is shown in Fig. 3.6. Two breaks can be identified, which indicate that the Ag growth rate was about 7 minutes per layer. This growth rate agrees quite well with the RHEED pattern observations, which showed that during the growth at the same temperature setting, Ru streaks became weaker and weaker and totally disappeared after about 7 minutes of deposition. It agrees also with the composition measurement of MnAg binary alloy overlayers. We have grown Ag and Mn simultaneously on Ru at T(Ag)=600C, T(Mn)=606C and T(Ru)=60C. The atomic composition Mn:Ag, determined by AES and XPS was about 3:1. Recalling that the Mn growth rate at T(Mn)=606C and T(Ru)=60C was around 2.3 minutes per layer, we can see that the 7 minutes per layer Ag growth rate matches the Mn growth rate quite well. This is also an indication that the sticking coefficient for Ag on Ru and for Mn on Ru is the same.

In the Ag 356eV curve (Fig. 3.6a), there is a kink at about $t_1'=2.3$ minutes, which corresponds to the time needed for completion of 1/3 of a monolayer of Ag. This might be due to the fact that up to this deposition time the Ag atoms are likely isolated from each other and thus have a larger Auger yield per Ag atom. A model of such a possible submonolayer arrangement of Ag atoms is shown in Fig. 3.7. Ag atoms at these submonolayer sites very likely form groups. These groups may not be coherent with each other, since we could not observe a clear superlattice RHEED pattern during the process of deposition. Similar submonolayer kink in the AES intensity vs. deposition time curve was observed by Binns and Norris (1982) for Mn overlayers on Cu (100). They have observed a sublattice LEED pattern for this submonolayer structure however.

In Fig. 3.6a, the first data point at t=0 in the Ru 231eV curve is unexpectly low. This may have something to do with the Ru surface conditions. It may also be related to the posible Ag submonolayer structure. Ru 231eV Auger electrons might shift the probability density due to this Ag structure. However, this behavior of Ag on Ru is not reproducibly observed. We have

Fig. 3.6. AES intensity vs. deposition time for Ag on Ru. (a) shows the breaks and (b) shows the exponential fits of the data, where the dash line in (b) shows the least square fit of the Ru 231eV data, the solid lines are the exponential curves obtained by using reasonable paramenters (see text).

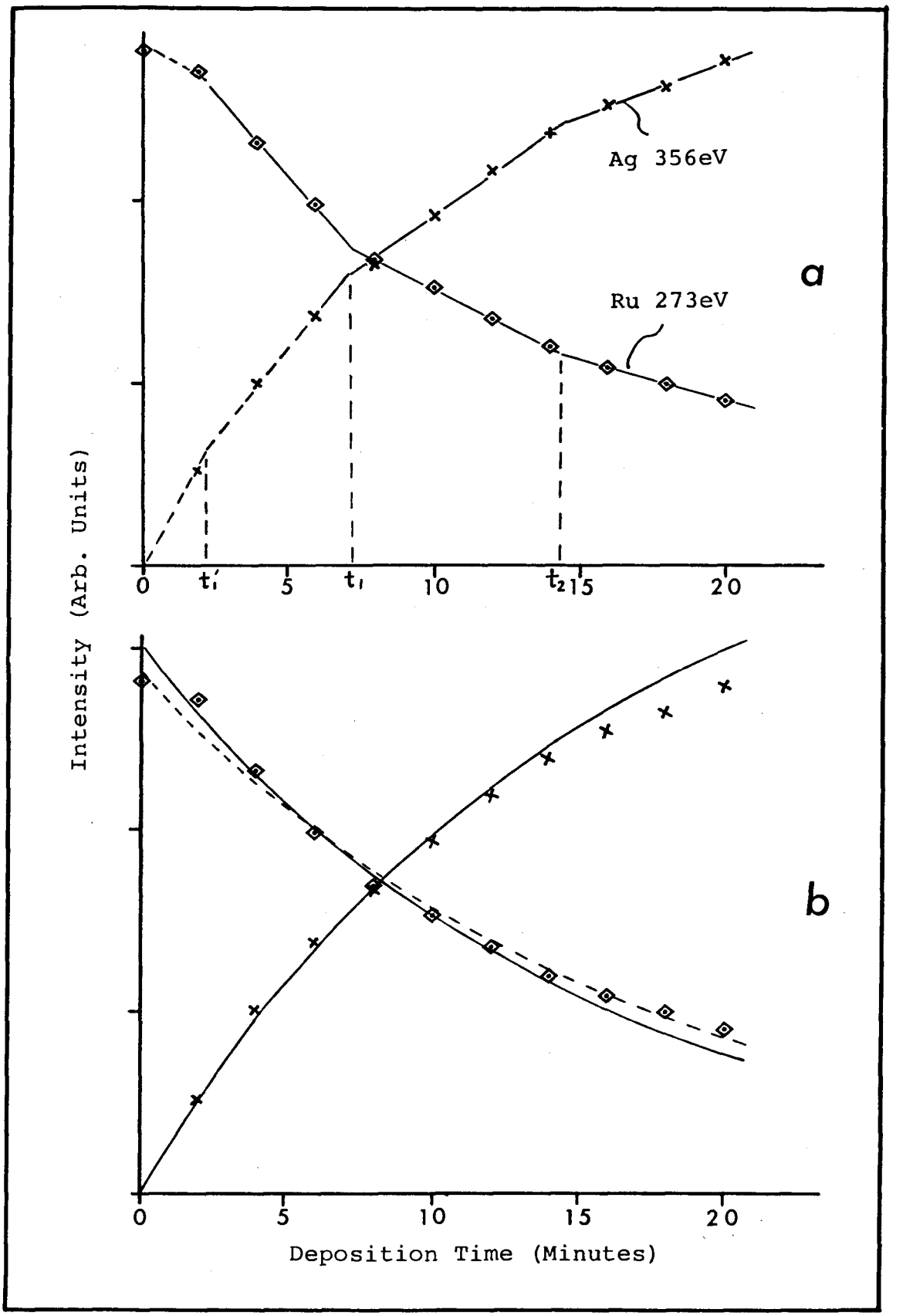
Ag 356eV
Ru 273eV
a
b
Intensity (Arb. Units)
0
t'
5
t
10
t2
15
20
Deposition Time (Minutes)

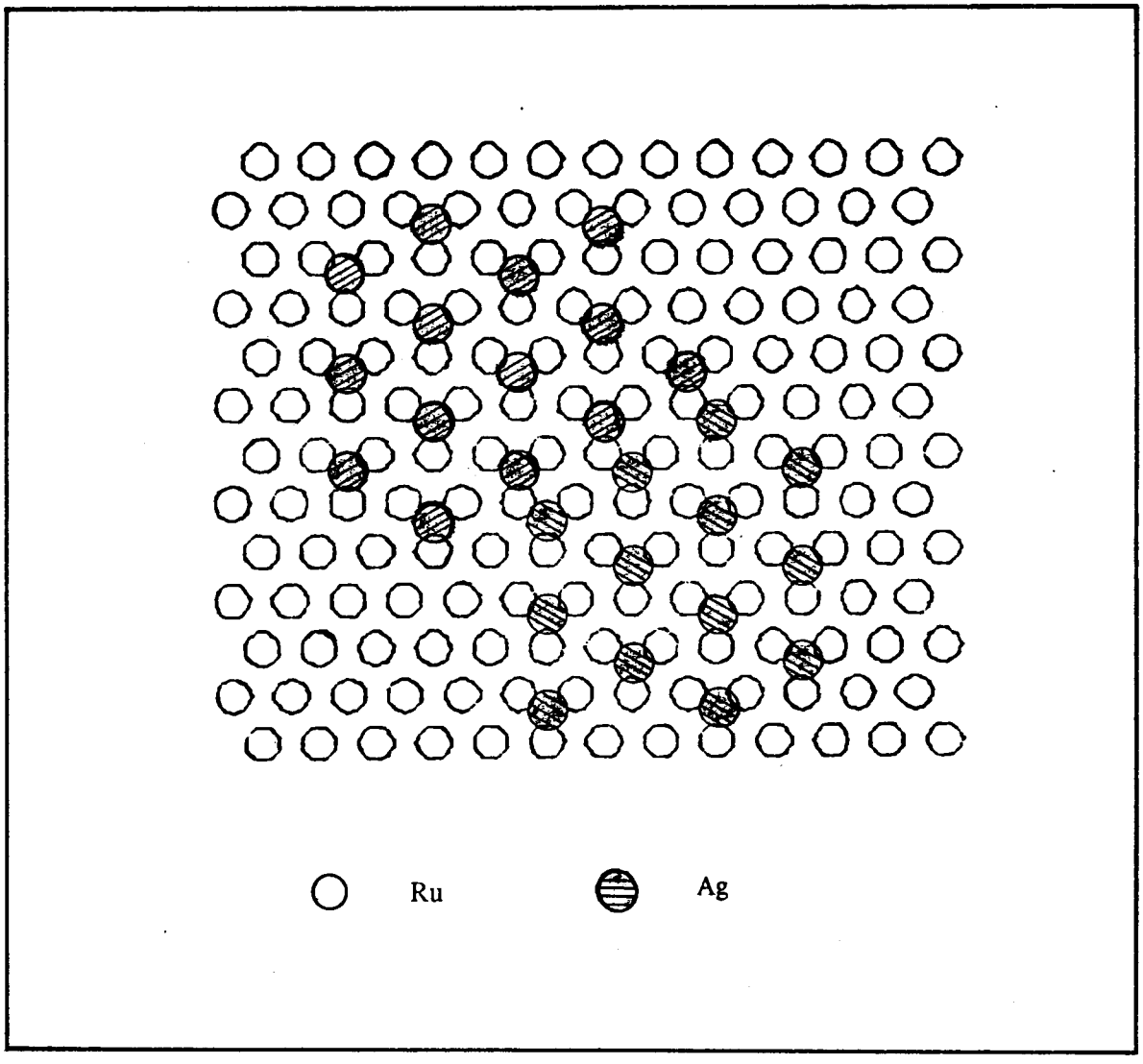

Fig. 3.7. A possible submonolayer arrangement of Ag atoms on Ru (001) at $t_1' = t_1/3$. t_1' and t_1 are defined in Fig. 3.6. Note that two incoherent Ag submonolayer groups are shown.

repeated the same experiment twice more. For one of these experiments, the first data point was low, similar to that shown in Fig. 3.6. For the other experiment however, the relative position of the first data point was much higher. The reason for this uncertainty about this first data point is not clear. In later analysis, we will ignore this data point.

The least square exponential fit for the Ru 231eV curve could not fit the data well even if we ignored the first data point. Such a fit is shown by the broken line in Fig. 3.6b. The Ag 356eV curve can be fit by an exponential curve since the undetermined saturation value of the Ag signal is an extra degree of freedom. But such a fit resulted in too small a λ value (5.5Å) for Ag 356eV Auger electrons. λ would be 8.5Å according to Eq. (3.2-1) or 10.1Å according to Eq. (3.2-2). The published value is 7.2Å (Jackson *et al.*, 1973) or 8.2Å (Seah, 1972). If we take λ = 7.2Å for Ag 356eV and λ = 6.6Å for Ru 231eV Auger electrons and a growth rate of 7 minutes per layer, the corresponding exponential curves can be plotted as shown in Fig. 3.6b by the solid lines. From Fig. 3.6b we can see that these two curves fit the data quite well up to t = 14 minutes (or 2 layers). Afterwards the data start to deviate from the solid curves. This is an indication of a three-dimensional flat island growth. So that likely the first two layers of Ag atoms were deposited in a layer-by-layer fashion and then Ag atoms prefered to form flat islands. These Ag islands were still flat up to over 40 layers as suggested by the RHEED observations which showed nice Ag streaks. This conclusion about the Ag growth is in agreement with other people's observation for Ag on Ge(001) (Lince *et al.*, 1983) and for Ag on Cu (Namba and Vook, 1981). More details of the Ag growth will not be attempted as it is not a principal interest of the present study.

Ag and Mn have been grown together on Ru(001) substrate. The composition of the grown alloys was determined by AES and XPS using the relative Auger sensitivity chart and the atomic sensitivity table (PHI's Handbook, Davis *et al.* (1978), Wagner *et al.* (1979)). To determine the intensity, the peak to peak height was used for AES and the area (background subtracted using a simple tangential baseline) under the XPS peak was used for XPS. For all the

measurements we have done, the results obtained from AES and from XPS are very close (within 5 percent). The uniformity of the coevaporation was checked by measuring different parts of the sample. The difference in composition over the sample (8 mm in diameter) was within 5 percent.

Seah (1983) described an improved method for the quantification of AES and XPS, where the corrections of the atomic size and the back-scattering factor have been considered. We have tried this method and found that this correction makes very little difference for the Mn and Ag alloys.

3.3 van der Merwe Model of Thin Film Growth

van der Merwe (1964, 1966, 1975) has developed a theory of the layer-by-layer growth of epitaxial bicrystals. An epitaxial bicrystal system consists of a semiinfinite single crystal substrate and an epitaxially grown two-dimensional overlayer crystal. At the interface between the two crystals, there is a discontinuity in the periodic crystalline structure of each crystal and a mismatch between the atoms on each side. The energy of an epitaxial bicrystal depends on the mismatch, the thickness of the film, the overall strain and the bonding both in the crystals and at the interface. The stable configuration corresponds to the one of minimum energy.

In the process of growth, the depositing atoms can sit in the potential minimum sites of the substrate (or the overlayer) and thus lower the energy. But by doing so the lattice parameter of the overlayer has to be changed if there is a lattice mismatch between the overlayer and the substrate. The change in the lattice parameter introduces a strain energy and thus increases the total energy. The thicker the overlayer, the larger the strain energy. So that in many cases of layer by layer growth, the first few overlayers may follow the substrate structure homogeneously with the same lattice parameter as the substrate and the misfit is accommodated entirely by elastic strain (no dislocations). This kind of growth is called pseudomorphic growth. The energy associated with the elastic strain is called the elastic strain energy. Then after these first few

layers, the overlayers that followed may relax to minimize the total energy, leading to the creation of the so–called misfit dislocations. By equating the elastic energy of the homogeneous strain in the overlayers with the interfacial energy (which is the sum of the misfit potential energy, the overlayer strain energy and the substrate strain energy), one can estimate how thick an overlayer one can grow without the appearence of misfit dislocations for a given system. Below, we will apply this theory to Mn growth on Ru and Ag growth on Ru. Before we do that, let us see that how to calculate the elastic strain energy and the interface energy.

For a van der Merwe model (or Frank and van der Merwe model, as first proposed by Frank and van der Merwe (1949a,b)), it is assumed that it is a plane strain problem. The energies associated with the x and the y misfit dislocations may be calculated independently and then added to obtain the total energy. Hence one can consider the x–direction only (1D model). Such a model is shown in Fig. 3.8, where the mismatching interface of two epitaxial crystals A and B with one–dimensional misfit is shown.

The elastic strain energy (which is proportional to the product of the shear modulus and the square of the strain, see the general reference, e.g., Timoshenko and Goodier (1951)) per unit area of interface may be written (Jesser and Kuhlmann–Wilsdorf (1967))

$$E_e=[\mu_b t/(1-\sigma_b)](e_x^2+e_y^2+2\sigma_b e_x e_y) \qquad (3.3\text{–}1)$$

where t is the thickness, μ_b is the shear modulus and σ_b is Poisson's ratio of the overlayer, and e_x and e_y are the strain along the x and the y directions respectively. In Eq.(3.3–1), it has been assumed that the strain energy in the substrate is zero and the thickness of the overlayer is allowed to expand or contract in accordance with Poisson's ratio. The quantity $\mu_b/(1-\sigma_b)$ is called the effective elastic constant of the overgrowth.

The interfacial energy is the total energy in the interface, which is the sum of the average misfit potential energy and both the overlayer and the substrate average strain energies. These

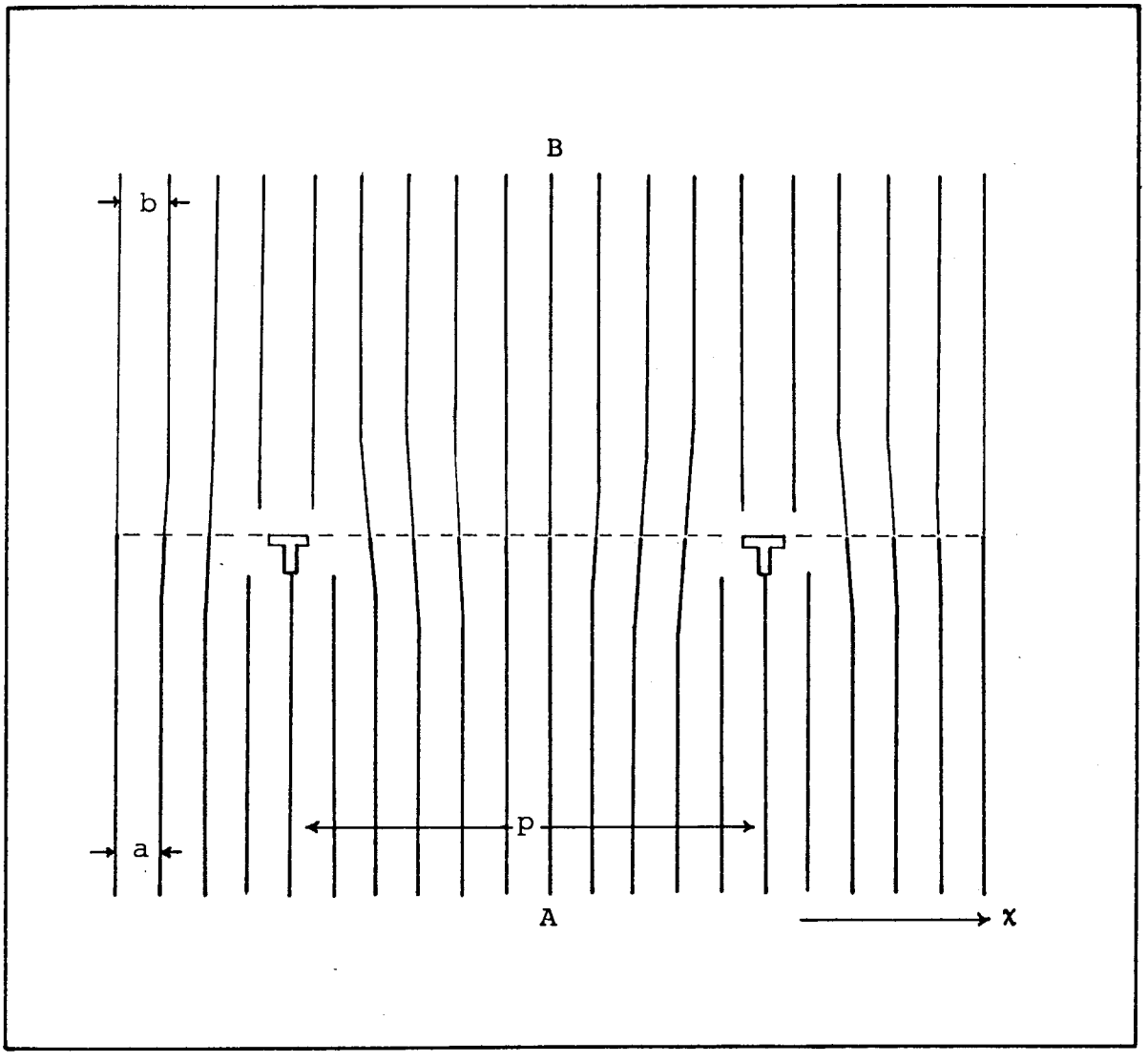

Fig. 3.8. The van der Merwe model showing the mismatching interface of two epitaxial crystals A and B with one-dimensional misfit. (taken from van der Merwe and Ball (1975))

energies have been calculated by using a sinusoidal model for the interfacial potential-energy density and using the Timoshenko (1934) method to solve a plane strain equation. The final result as shown by van der Merwe and Ball (1975) is

$$E_i = 0.5(\mu c/2\pi^2)(c/d)[1-A-\beta \ln(1-A^2)] \quad (3.3\text{-}2)$$

$$\beta = 2\pi d\lambda/\mu p \quad (3.3\text{-}3)$$

$$\lambda = [(1-\sigma_a)/\mu_a + (1-\sigma_b)/\mu_b]^{-1} \quad (3.3\text{-}4)$$

$$A = (1+\beta^2)^{1/2} - \beta \quad (3.3\text{-}5)$$

(if we take the first approximation).

Where μ is the interfacial shear modulus, σ the interfacial Poisson's ratio, c the average interfacial lattice spacing, p the misfit spacing and d the layer spacing. Now we take the case of Mn on Ru to calculate these quantities.

First of all, we determine the lattice parameters. Ru has a hexagonal lattice with a=2.70Å. The lattice spacing of Mn is hard to determine, because it has four complicated allotropes. The most common form of Mn at R.T. is α-Mn, which has 29 atoms per unit cell (or 58 atoms in a BCC unit cell) with the closest approach of 2.24Å. β-Mn (stable from 700C to 1079C) has 20 atoms in a BCC unit cell. γ-Mn has a FCC structure at high temperatures (1079C-1143C). The metastable γ-Mn phase made by electrolysis at R.T. is FCT (Face Centre Tetragonal) with a lattice parameter of 3.782Å, a c/a ratio of 0.934 and the closest approach of 2.587Å. The fourth allotrope, namely, δ-Mn, is obtained only at very high temperatures (from 1140C to the melting point of Mn). (Barrett (1952), Sully (1955)). For the case of Mn grown on Ru, since Ru has a close packed hexagonal lattice, the grown Mn might have a structure similar to γ-Mn, at least for the first two overlayers(cf. the RHEED analysis in Chapter 3). It is well known that a close packed lattice with an ABCABC... stacking is a FCC lattice, but the basal plane is the (111) plane of the FCC lattice. So that it is reasonable to assume that the equilibrium Mn spacing is close to 2.587Å, the closest approach in γ-Mn at R.T. (the distortion of γ-Mn from FCC to

FCT has been neglected in the assumption). We will take this value for our calculation, i.e., take b=2.587Å (cf. Fig. 3.8).

For other parameters, we have the average interfacial lattice spacing c=2ab/(a+b)=2.64Å, the misfit spacing p=ab/(a-b)=61.80Å and the layer spacing d=2.20Å (assuming that d is the same as the Ru(001) layer spacing).

The shear modulus and Poisson's ratio for many elements can be found in the handbook edited by Samsonov (1968). Some of them are listed in Table 3.1.

Table 3.1 Shear modulus and Poisson's ratio of Ru, Ag, Cr, Fe and Co

Element(i)	μ(i) (GN/m^2)	σ
Mn	/	/
Ru	173	0.296
Ag	28.8	0.37
Cr	71.6	/
Fe	81.2	0.28
Co	74.8	0.31

Since the Mn data are not available, we assume that they are close to that of Cr, Fe and Co, and assume μ(Mn)=75 GN/m^2 and σ(Mn)=0.3.

The interfacial shear modulus μ can be derived from the relationship between the shear energy $\mu c/2\pi^2$ and the interfacial potential energy of interaction. The interfacial potential energy depends on the adsorption energy for A atom on B atom, ϕ(AB), and that for B atom on A atom, ϕ(BA), (van der Merwe (1964)). The final result for a close-packed surface can be derived as

$$\mu=(\pi^2 n/3c)[\phi(AB)+\phi(BA)] \tag{3.3-6}$$

where n is the atomic plane density at the interface. For a Ru substrate, $n=1.584\times10^{15}/cm^2$. The adsorption energies ϕ(RuMn) and ϕ(MnRu) can be obtained from the paper by Miedema and Dorleijn (1980), from which we have ϕ(RuMn)=450 KJ/mole and ϕ(MnRu)=325 KJ/mole. Thus we have from Eq.(3.3-6) the interfacial shear modulus $\mu=2.52\times10^{12}$ dyne/cm^2. Then Eqs.(3.3-2) to (3.3-5) lead to $E_i=3.35\times10^{10}$ dyne·Å.

To calculate the elastic strain energy E_e by using Eq.(3.3-1), it is noted that Mn on Ru has a hexagonal symmetry while Eq.(3.3-1) refers to rectangular coordinates. This difficulty can be overcome if we consider the hexagonal grid of misfit dislocations as the product of two parallel sets of dislocations with a spacing equal to half the diameter of the hexagonal cell (Jesser and Kuhlmann-Wilsdorf (1967)). Here again we take the bulk Mn spacing as the same as the closest approach of γ-Mn (2.587Å). Decomposing the displacement between Mn and Ru into x and y components would lead to the conclusion that the strains $e_x=e_y=(2.7-2.587)/2.587=0.044$. Thus according to Eq.(3.3-1) we have $E_e=t\cdot0.54\times10^{10}$ dyne. The critical condition $E_e=E_i$ then leads to the conclusion that one can grow a Mn overlayer of thickness t=7.6Å (or about 3.5 layers) on Ru(001) substrate without the appearence of misfit dislocations. This is in good agreement with our observation (~5Å), considering the approximations and assumptions we made in the calculation.

One might also remember that in Section 3.2 we proposed a model to explain the observed RHEED pattern for the grown Mn in a modulated structure, where a 3x1 structure with a Mn

spacing of 2.39Å was suggested. If we use b=2.39Å in the above van der Merwe calculation, we would end up with a critical thickness of 1.6Å, which seems too small compared to the observed value. Thus the modulated bulk Mn structure might be not suitable for determining b, the equilibrium Mn spacing. This is not that surprising if one considers the geometry of the trimerized structure. Due to the strange behavior of Mn atoms, the choice of the equilibrium Mn spacing is an open question.

The van der Merwe calculation should be regarded as a rough estimate. For example, for a magnetic material, we should also consider the energy due to the magnetic moment. As shown by Oguchi and Freeman (1984), the antiferromagnetic fcc Mn undergoes a magnetically induced lattice distortion (which is a contraction perpendicular to the ferromagnetic lattice plane). This influence of the magnetic moment has been totally ignored in the van der Merwe model. Nevertheless, as indicated by the above calculations, the results are in reasonable agreement with the experimental observations. It shows that the information about the mismatch and adsorption energies of the substrate and the overlayer clearly have significant importance for the layer-by-layer growth. Our calculation for the case of Mn grown on a Ru(001) surfase confirms that the 3x1 structure we observed in the RHEED pattern is due to the shrinking of Mn atoms.

Similar calculations for the case of Ag on Ru have also been carried out. In contrast to the case of Mn on Ru, Ag has a larger lattice spacing than Ru (call it positive misfit), with the closest approach of 2.89Å and a layer spacing d=2.36Å. Other quantities needed for the calculation can be obtained from the same sources as were used for the calculation of Mn on Ru. A critical thickness of t=5Å or about 2 layers was obtained for a room temperature substrate. As observed by AES, a 3-dimensional growth developed after the first two Ag overlayers, but the RHEED patterns showed that Ag had its own lattice spacing even in the first overlayer. This is not in agreement with the above calculation. The main reason is that in the van der Merwe model, only purely harmonic interactions between the atoms are considered. By introducing anharmonicity in the interactions of the overgrowth, Markov and Milchev (1984) demonstrated

that due to effects of substrate–induced fracture, the positive misfit appears more difficult for the pseudomorphic epitaxial growth of thin films than the negative one. Under equal other conditions, the critical thickness for pseudomorphic growth should be smaller when the misfit is positive. This is in agreement with our observations for Mn growth on Ru (negative misfit) and for Ag growth on Ru (positive misfit).

CHAPTER 4

EELFS ANALYSIS OF MN THIN FILMS ON RU

In recent years, there has been a rapid growth of activities in structure studies using Electron Energy Loss Spectroscopy (EELS) technique. EELS measures the inelastically scattered electrons as a function of their kinetic energy. These electrons can be produced and measured in an AES setup, i.e. basically an electron gun and an electron energy analyzer in a UHV system. In our setup, the electrons are normally incident on the sample and the scattered electrons are detected in a reflection mode within a cone of 42° around the normal of the sample surface. The energy and momentum of the incident electrons are fixed, while the energies of the scattered electrons are analysed.

When electrons are incident on a solid sample, most of them are elastically reflected. Some of them however, will suffer energy losses. At those energies which are just large enough to excite core-level electrons out of the sample, the energy loss becomes most serious. This is due to the well-known edge-absorption. From the absorption edge, in an energy range extended for several hundred eV, there is fine structure which contain structure information of the sample, similar to those in x-ray absorption spectra. For this reason, they are called EELFS (Extended Energy Loss Fine Structure), similar to EXAFS (Extended X-ray Absorption Fine Structure).

The fine structure in both EELS and EXAFS is caused by the interference of an outgoing state from the central atom with backscattered components from neighboring atoms. In EXAFS, the photon radiation is treated as a classical electromagnetic wave and its reaction with the core state of the atom can be represented by the dipole approximation. The absorption of photons can be treated to first order and calculated from the "Golden Rule". Thus the structure information can be obtained from the square of the matrix elements $|\langle f|\hat{e}\cdot r|i\rangle|$, where $|f\rangle$ is the final state of the photoelectron, $|i\rangle$ is the initial core state, $\hat{e}$ is the polarization unit vector

of the electric field of the x-ray and r is the position vector of the photoelectron taking part in the transition. The initial state $|i>$ is fixed and does not change with the x-ray energy. The final state $|f>$, which can be considered as a sum of the outgoing state from the centre atom and the backscattered part from the surrounding atom, does change with the x-ray energy and causes the fine structure. Detailed analysis (e.g. Stern (1974)) shows that the geometric structure of the sample determines the Fourier transform of the fine structure.

In the case of EELS, the incident electrons are fast compared to the mean orbital velocity of the core electrons. Thus the atomic potential acts as a weak perturbation, i.e. the first Born approximation is valid and both the incident and scattered electrons can be treated as plane waves. In this case the inelastic cross section and thus the fine structure in the loss spectrum is proportional to the square of the matrix element $|<f|\exp(i\mathbf{q}_3\cdot\mathbf{r})|i>|$, where $\mathbf{q}_3$ is the momentum transfer during the process and r is the position vector of the related electrons (Leapman *et al.* (1980)). In the limit of $\mathbf{q}_3\cdot\mathbf{r}<<1$ (which is the case in EELS), the matrix element reduces to $|<f|\mathbf{q}_3\cdot\mathbf{r}|i>|$, which is similar to that in the EXAFS case. People thus expect a correspondence between EELS and EXAFS. The same Fourier transform technique used in EXAFS should also give structure information when it is applied to EELS. This has been proved true experimentally for many systems (Chiarello *et al.* (1984)). The quantitative theoretical calculations however, are usually more difficult in EELS than in EXAFS. This is because in EELS there are multiple-scattering events taking place in both the initial and final states. Also, there are two final-state electrons in EELS, since both the incident electron and the ejected core electron must be accommodated above the Fermi level. Despite these difficulties in theoretical calculations, experimentally we can successfully obtain the structure information from EELS by carefully choosing suitable material as standards. Our EELS investigation of Mn thin films on Ru was carried out on this comparative basis. Ni and α-Mn were studied together with Mn on Ru for comparison. The structure of an fcc Ni single crystal is simple and well known and EELS study on a Ni single crystal has been carried out by Crescenzi *et al.* (1981). This gives us a good case

to be used to check our technique. By comparing the results we obtained for Mn on Ru and that for α-Mn and for Ni, we can thus get information about the structure of our MBE-grown Mn thin film.

4.1 Experimental Details in EELS

The growth of Mn thin films on Ru has been described in Section 3.1. Thin Mn films of about 15 layers thick were usually used for EELS measurements. These films showed nice 3x1 RHEED patterns which indicate a new phase of Mn. The investigation of two-layer Mn on Ru has been hampered by the interference of the Ru substrate EELS signals.

A polycrystalline α-Mn plate was cut, mechanically polished with a one micron diamond finishing, and chemically polished in an ultrasonic cleaner. The solutions for chemical polishing were ~5% nitric acid mixed with ~95% acetone. After chemical polishing the sample was cleaned and then mounted and dried in the introduction chamber with dry nitrogen gas flowing through to prevent α-Mn from forming too thick an oxide layer. The sample was then cleaned in the UHV by Ar^+ sputtering – heating – Ar^+ sputtering cycles. The α-Mn sample after the above treatment contained about 5% of oxygen and no other detectable impurities within the limits of AES. AES was used both before and after EELS measurements to monitor the sample contamination.

The Ni single crystal we used was an ~4x5 mm^2 disc with a thickness of ~0.6mm and RRR≃245, where RRR is the Residual Resistivity Ratio. It was cleaned in the UHV chamber by cycles of Ar^+ sputtering and annealing at 750° C. No detectable impurities were found on the Ni surface after the above treatment.

The measurements were carried out (at R.T. in all cases) in the usual Auger mode with mostly a primary beam energy (E_p) of 1 keV. The energy resolution we used was $\Delta E/E=0.6\%$,

where ΔE is the absolute energy resolution and E is the kinetic energy of the electrons to be analysed. Different beam energies of 1100 eV and 1200 eV were also used to see if it makes any difference. The energy loss spectra, recorded as the derivative of the electron energy distributions with a 6eV peak-to-peak modulation, showed no difference for beam energies from 1 keV to 1200eV. One such spectrum for Ni is shown in Fig. 4.1. The prominent peak on the high energy side is the derivative of peaks due to the $3p_{3/2}$ and $3p_{1/2}$ excitations. It can be used for energy calibration purpose. The small peak at ~888eV is the derivative of the 3s edge. The other wiggles are the extended energy loss fine structure of the 3p edge, in which we are interested. These fine structure oscillations extended a few hundred eV from the edge. They are weak in amplitude and have very low frequences. The 3s edge will not interfere with the 3p edge energy loss fine structures since it is quite small by itself and has basically no oscillations.

Energy loss spectra for α-Mn and Mn on Ru are similar to that for Ni. But the EELFS oscillations are weaker (still visible) compared to the case of Ni. To increase the sensitivity, for α-Mn and Mn on Ru the energy scanning range (usually 500eV) was so chosen that it catches just the Mn 3s edge and avoid the Mn 3p edge. The Mn 3p edge was recorded separately (for calibration use) using a smaller channeltron voltage. The data were recorded in the Nicolet signal averager with a scanning speed of 1eV/sec and were accumulated for 4 to 8 scans to improve the signal-to-noise ratio. It was found that at the end of each measurement, the amount of oxygen was always increased (the basic vacuum was in 10^{-10} torr range) but still relatively small and the Mn 2p XPS peak did not show noticeable change. This indicates that the formation of MnO is negligible.

Fig. 4.1. Ni 3p edge EELS data (derivative mode with 6eV p–p modulation). The primary electron beam energy was 1 keV. Peaks due to the 3p and 3s excitations are indicated in the diagram. E_0 is the onset of the 3p edge.

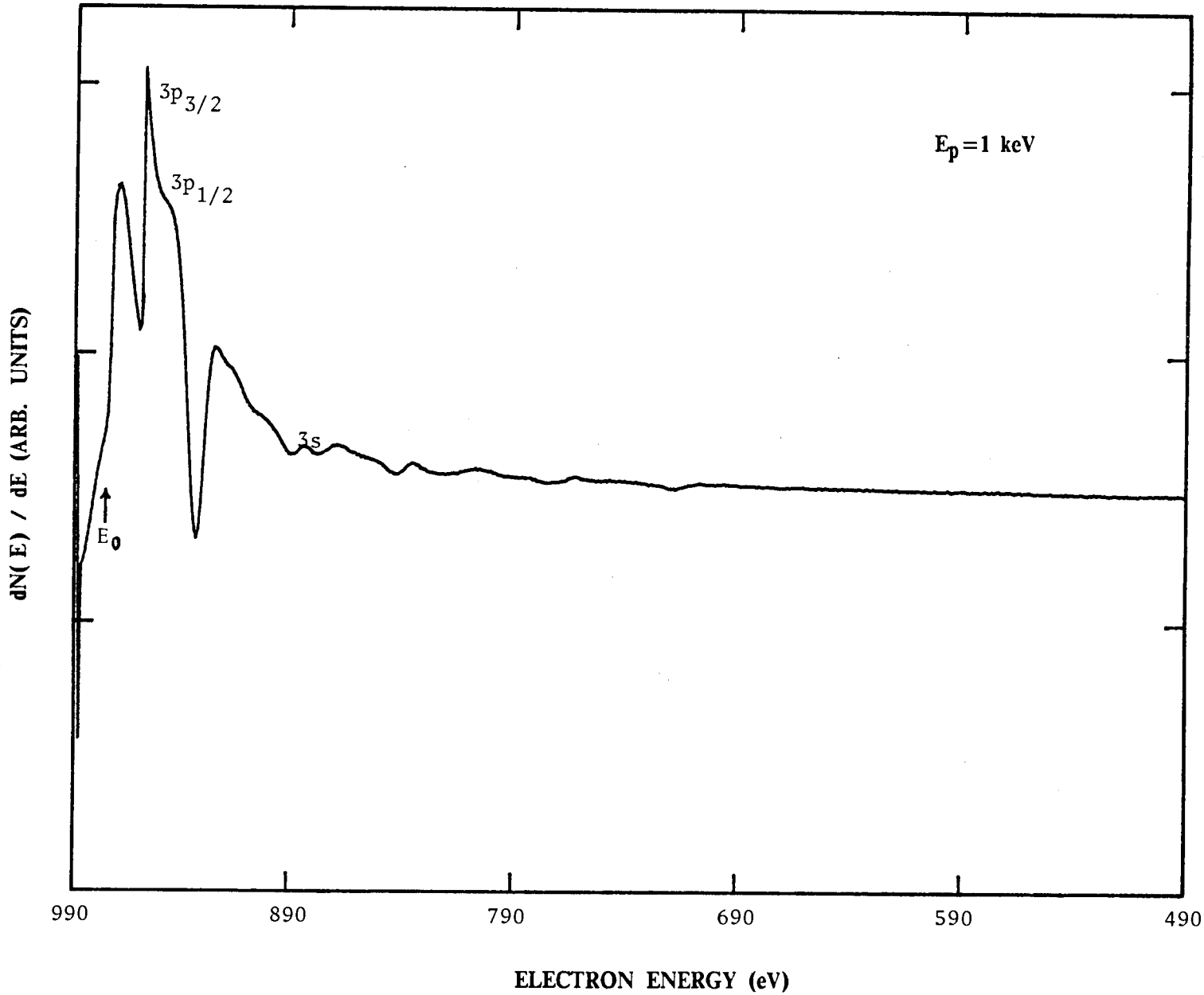
$3p_{3/2}$
$3p_{1/2}$
E_p=1 keV
3s
E_0
dN(E) / dE (ARB. UNITS)
990
890
790
690
590
490
ELECTRON ENERGY (eV)

4.2 EELFS Analysis and Results

In order to obtain the structure information, the raw data such as that shown in Fig. 4.1 should be properly processed. Our procedure to handle the data is as follows. First of all, the original derivative data were integrated and then the background was carefully subtracted. The coordinate was converted from energy E(eV) (in Fig. 4.1) into the wave vector $k(Å^{-1})$ ($k(Å^{-1})=\sqrt{(0.263(E-E_0)(eV))}$, where E_0 is the 3p edge onset. Usually the inflection point (cf. Fig. 4.1) is taken as E_0). After these treatments the oscillatory part above the 3p edge for Ni is shown in Fig. 4.2, where $\mu(k)$ is the electron intensity. The prominent peak in Fig. 4.2 is the 3p edge.

The Fourier transform of $\mu(k)$ then gives the structure information and is shown in Fig. 4.3 (Thanks are due to Dr. Neil Alberding for carrying out the analysis and plotting the diagrams). The limits of the Fourier integral were 2.6 to 11.2 $Å^{-1}$. The correction for the phase shift between the outgoing wave and backscattered wave is not included in the diagram. Similar to EXAFS, the Fourier transform magnitudein EELFS is strongest for the first-neighbour atomic shell and dies away rather fast when the distance increases. Since the Ni structure is well known, we can determine the phase shift by comparing the known Ni first nearest neighbour distance and the position of the first peak in Fig. 4.3. This correction was determined to be -0.18Å, i.e., the whole R(Å) coordinate should be shifted 0.18Å to the right. After taking this correction into account, the second peak position meets the second nearest neighbour distance quite well. For other peaks in Fig. 4.3, this kind of assignment becomes more difficult. Although the third peak corresponds to the fourth nearest neighbour distance, we could not make any sense of the fourth peak in Fig. 4.3. The main reason is that as we go to higher orders, the complicated combination of atomic distances together with the different phase shift for more complicated geometry might smear out the Fourier signal. Nonetheless, the results for the first two peaks are quite satisfactory and we can thus use this technique for other elements.

Fig. 4.2. Ni EELFS signal after integration and background subtraction from Fig. 4.1. The absolute zero of $\mu(k)$ is not shown. The variable has been converted from energy(eV) into wave vector ($Å^{-1}$).

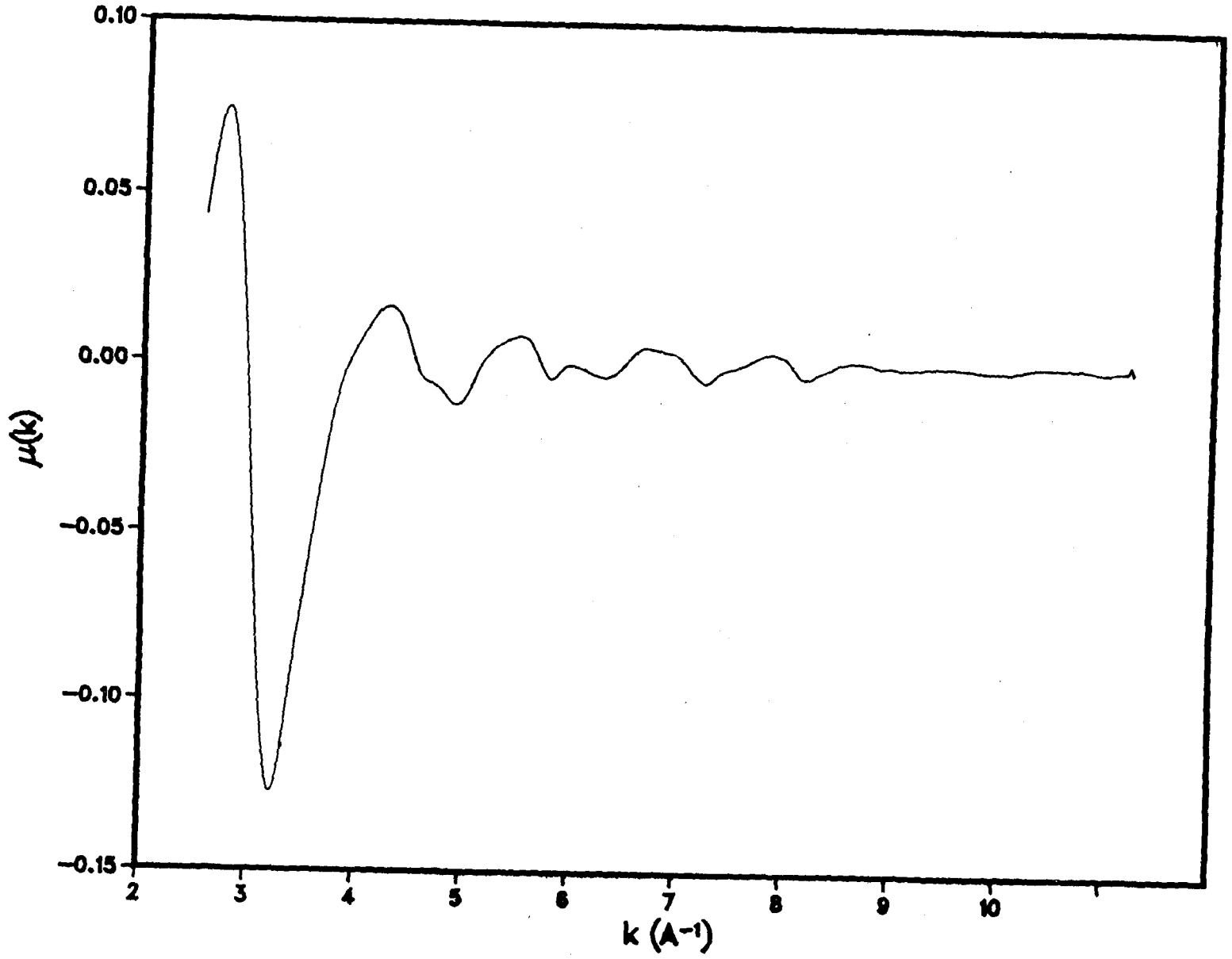

q 69 b

Fig. 4.3. Fourier transform of the EELFS signal of Fig. 4.2. The integration limits were 2.6 to 11.2 $Å^{-1}$. R is the distance from the central atom.The phase shift correction is not included in the diagram. The inset shows the Ni structure, where the arrows indicate the first nearest neighbour (No.1), the second nearest neighbour (No.2),*etc.*

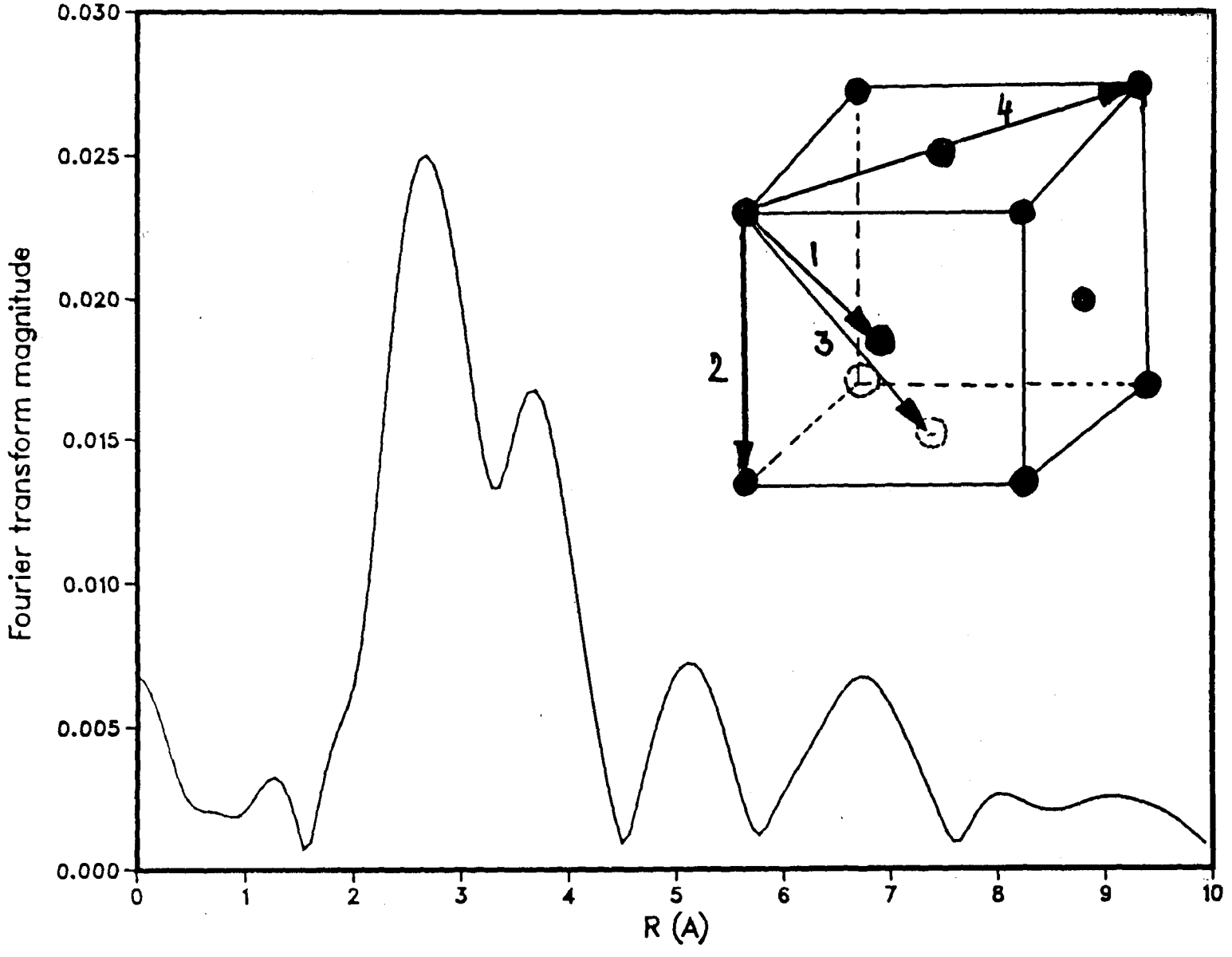
0.030
0.025
0.020
0.015
0.010
0.005
0.000
Fourier transform magnitude
0
1
2
3
4
5
6
7
8
9
10
R (A)
1
2
3
4

We have applied this technique to α-Mn and the trimerized Mn on Ru substrate. The results of Fourier transform are shown in Fig. 4.4, where R(Å) is the distance from the central atom without the phase shift correction. From Fig. 4.4 it can be seen that the peaks for Mn on Ru are narrower and more well defined compared to the α-Mn case. As we mentioned in Section 3.3, α-Mn has very complicated structure which contains four kinds of atoms. There are 58 atoms in a unit cell with the closest approach of 2.24Å. This accounts for the very broad Fourier peaks. Comparing (a) and (b) in fig.4.4, it is clear that the MBE-grown Mn on Ru definitely has a different and simpler structure than α-Mn. Further more, as shown by the dotted line, the first peak for Mn on Ru corresponds to a larger first-neighbour distance (we assume that Mn in the MBE-grown Mn and Mn in α-Mn have the same phase shift). From Fig. 4.4, it can be measured that the difference in distance is 0.15 ± 0.02Å. Thus the closest approach in Mn on Ru is 2.39 ± 0.02Å. This is in excellent agreement with the model we proposed in Section 3.1, where we suggested that the trimerized Mn consists of tetrahedra with a distance of $\sim$2.39Å between neighbouring atoms. Considering the assumptions we made in calculating this distance, this exact agreement should be regarded as accidental. But clearly the nearest neighbour distance in Mn on Ru is noticeably greater than that in α-Mn and not as large as the Ru spacing 2.70Å and certainly not as large as 4.68Å($\sqrt{3}$ x Ru spacing) seen in the diffraction pattern. The well defined Fourier peaks (Fig. 4.4b) together with the observations of RHEED suggest that the model of trimerized Mn is quite reasonable. The distance of the second Fourier peak in Fig. 4.4b is about 3.70Å after taking the phase shift into account. This might correspond to the second nearest neighbour distance. But considering that the magnitude of the second peak is quite small and that the stacking of the trimerized Mn is complicated, this second peak should not be taken too seriously.

We found that EELS is a quite useful technique in MBE work. Combining with RHEED it can help us to clarify the structure of MBE-grown films. For example, from RHEED we found that the MBE-grown Ni on Fe should have a bcc structure like Fe instead of the usual Ni

Fig. 4.4. Fourier transform of EELFS signals for: (a) α-Mn and (b) ~15 layers of Mn on Ru. The phase shift corrections are not included. The dotted line serves as a guide to the eyes for comparing the first peak positions in (a) and (b).

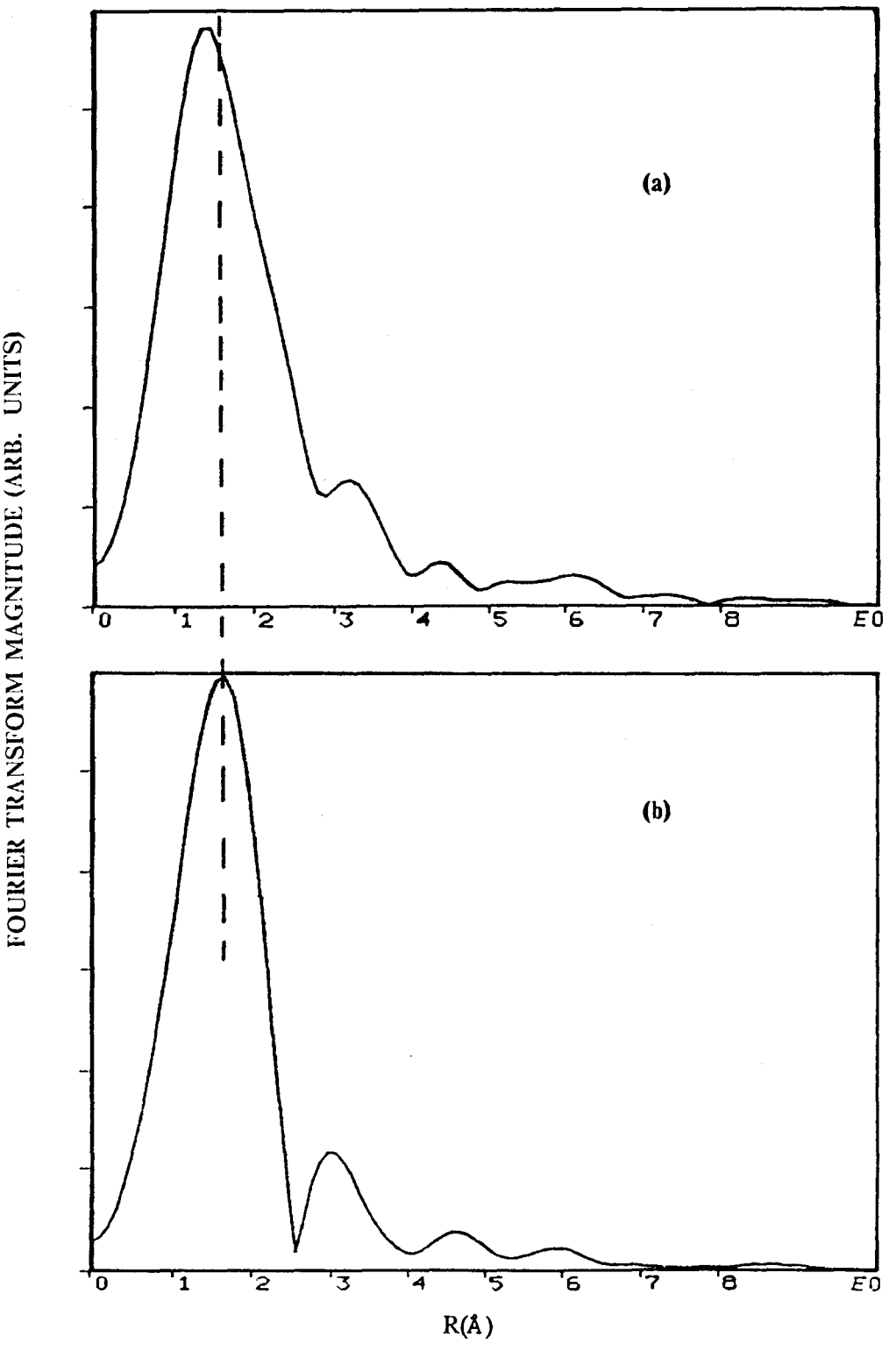
FOURIER TRANSFORM MAGNITUDE (ARB. UNITS)
(a)
(b)
0
1
2
3
4
5
6
7
8
E0
R(Å)

fcc structure. Otherwize the Ni spacing has to increase by 15% in order to explain the RHEED pattern (Heinrich *et al.* (1985b)). By using EELS, if we find the nearest neighbour distance is close to that of Fe, then we know that the grown Ni is a bcc Ni and not an expanded fcc Ni. Such an experiment is in progress. No doubt, we will find more and more applications of EELS in the field of MBE and surface sciences.

CHAPTER 5

XPS STUDIES OF MN, AGMN AND VMN THIN FILMS ON RU SUBSTRATE

XPS is the main technique we used to study the physical and chemical properties of Mn thin films. It was used mostly in three fashions in our study. One is the survey scan of the sample, where Mg-k_α x-rays ($h\nu = 1253.6$eV) were usually used and the binding energy scanned from 1000 eV to 0 eV. Another is the narrow scan for certain interesting XPS peaks, such as the Mn 2p peak, where the chemical state of the sample can be detected from the chemical shift of the peak. The third is the accumulated narrow scan especially for the XPS 3s peak, from which we obtain information about the magnetic moment of the atoms in the sample. The 3s peak study is the main object and will be discussed in detail in this chapter.

Fig. 5.1 is an XPS survey scan of an ~2-layer Mn thin film on a Ru substrate. The scan was obtained using a Mg-k_α x-ray radiation. The analyzer pass energy was 100eV. At the thickness of ~2 layers of Mn, all the Ru peaks can still be easily seen. Fig. 5.1 shows nicely both the Mn and Ru signals. Using the PHI's XPS Handbook, these peaks are identified and shown in the figure. Also shown in Fig. 5.1 are peaks due to Auger transitions. The symbols L_3, M_{23} and M_{45} *etc.* are x-ray notations of energy levels (cf. Section 2.4). The symbol V represents all valence (or quasi-valence) levels of the element, e.g., V stands for M_{45} and other valence states for Mn and stands for N_{67} and other valence states for Ru. The Auger peaks in XPS will be discussed in Chapter 6, which deals with AES.

Although Mg-k_α is mostly used in our study, Al-k_α x-ray ($h\nu = 1486.6$eV) is also quite useful. The energy of photoelectrons is dependent on the excitation energy, while the energy of Auger electrons is only related to the energy levels involved in the Auger transition. Remember that the XPS spectrum is recorded as a function of the binding energy. As a result, the same Auger peak will have a different line position for Mg and Al x-ray sources. This fact can be

Fig. 5.1. XPS spectrum of a ~2-layer Mn thin film on Ru substrate with a Mg-K_α x-ray radiation and 50 eV pass energy. At this thickness of Mn, both Mn and Ru signals can be seen. The peaks are identified in the figure, where V stands for valence levels, i.e., M_{45} and other valence states for Mn and N_{67} and other valence states for Ru spectrum.

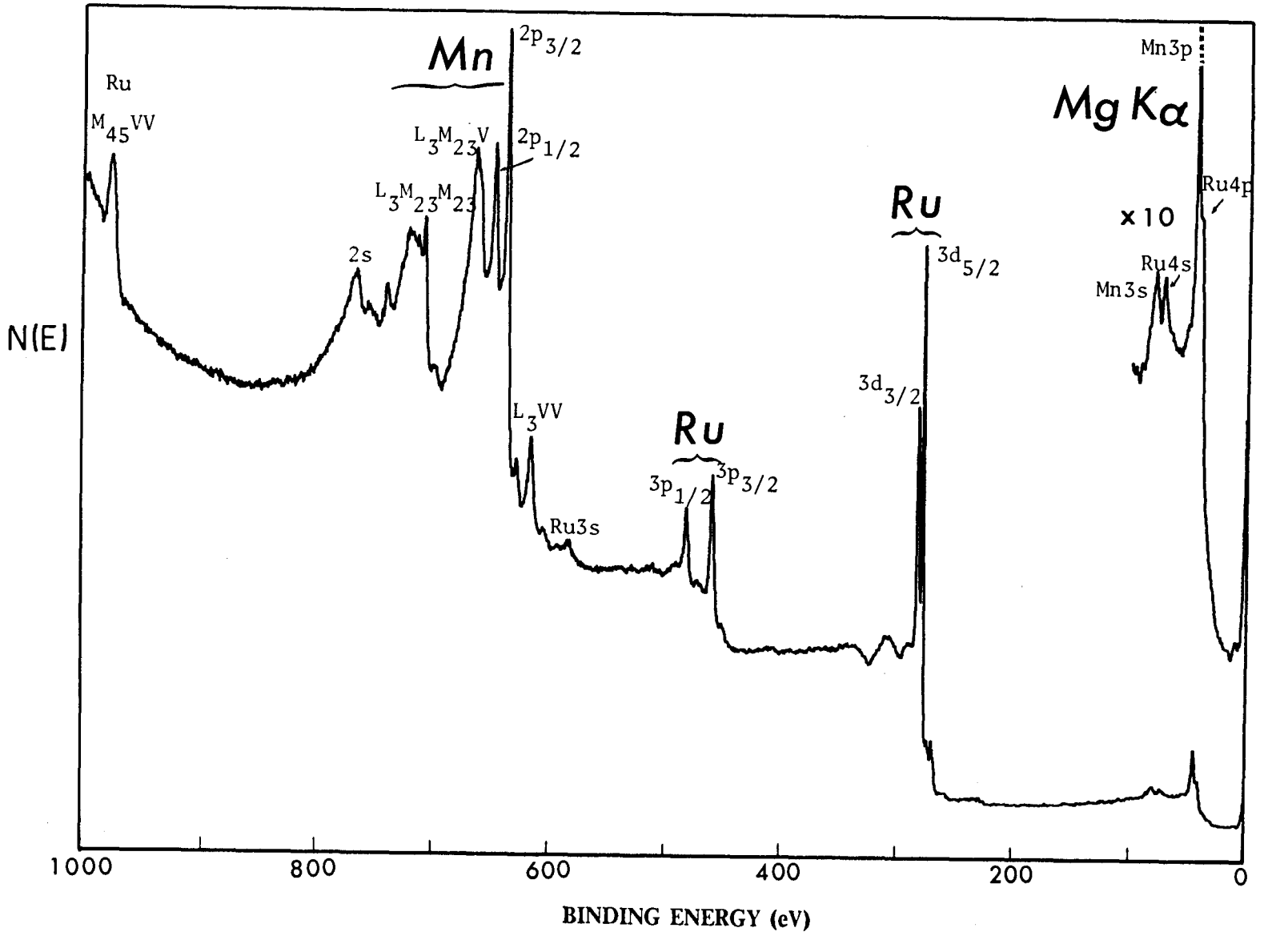
Mn
2p3/2
Ru
M45VV
L3M23V
2p1/2
L3M23M23
2s
L3VV
Ru3s
Ru
3p1/2
3p3/2
Ru
3d5/2
3d3/2
Mg Kα
Mn3p
Ru4p
x10
Ru4s
Mn3s
N(E)
1000
800
600
400
200
0
BINDING ENERGY (eV)

used to identify Auger peaks in XPS by comparing the spectra obtained from Mg and Al x-ray excitations. This is especially useful for analysing some compounds where the peaks are more complicated.

The survey scan can be used to monitor the MBE growth. As stated in Chapter 3, Mn growth on Ru has a layer-by-layer feature and this feature is evident from XPS. Our XPS spectrum showed that the Ru high-binding-energy signal decayed more rapidly compared to the low-binding-energy signal upon the Mn growth as it should for a uniform growth.

The survey scan is useful for detecting the impurities in the sample. From Fig. 5.1 we can see that the sample measured was very clean and contained no other detectable impurities. It should be remembered however, the sensitivity for detecting impurities from XPS is rather low (detectable impurities range from about 0.1% to 1% at.). It is especially difficult to detect carbon in ruthenium, where their XPS signals are mixed together. It is also hard to detect small amount of oxygen in Mn, since oxygen has a much lower XPS sensitivity factor compared to manganese (2.1 for Mn and 0.63 for oxygen).

The survey scan is also useful to locate each individual peak. From the survey scan we can determine the range of narrow scans for the interesting peaks. In the following section we will discuss some of these peaks, especially the 3s peaks. But before we go to the 3s peaks, we will discuss the Mn 2p peak and the oxidization process of Mn.

5.1 XPS Study of the Oxidization Process of Mn

It would be nice if we could take the grown Mn thin films out of the UHV chamber and carry out measurements outside. But the oxidization of Mn is a serious problem. Even in the UHV chamber, the Mn thin films are still gradually oxidized by the residual oxygen in the vacuum. This oxidization problem can not be neglected in the material we are studying. Thus it

is very important to find an effective way to monitor the oxidization process of Mn. We found that the Mn XPS 2p peak is very sensitive to the oxidization and that observing the shape of the Mn 2p peak is the best way to monitor the oxidization status of Mn. As introduced in Section 2.4.1, the chemical environment will have a big influence on the core level electrons and shift their energy levels. When an oxygen atom is attached to Mn atoms, the distribution of electrons will change correspondingly. More electrons will be attracted towards the oxygen atom, leading to a higher binding energy of core electrons of the surrounding Mn. For the rest of Mn atoms the binding energy will be unchanged. As a result, the measured core level XPS peaks will show a change in the line shape, composed of a normal part and a higher binding energy part. The more oxygen, the stronger the higher-binding-energy-part will be. And also, the more oxygen, the higher binding energy the core electrons will have.

In a Mn atom, the 2p electrons are closer to the nucleus compared to 3s and 3p electrons, so that they are more sensitive to the change in binding energy. Also, in XPS, Mn $2p_{3/2}$ peak is the strongest one, which makes it easier to observe the change in peak shape. For this reason, we have used the $2p_{3/2}$ peak to study the oxidization of Mn.

Fig. 5.2 shows two sets of Mn $2p_{3/2}$ peaks for different oxidization status. Data shown in Fig. 5.2a was taken just after the growth of ~2 layers of Mn on Ru. That in Fig. 5.2b was taken 5 hours later including ~3 hours of XPS measurements. Fig. 5.2c is the superposition of (a) and (b). The difference between (a) and (b) can be clearly seen from the figure. The shoulder at around 641.5 eV is due to the formation of Mn oxides. The shoulder was greatly increased for case (b). The main peak was also lowered a little because of the oxidization. The intensity on the lower binding energy side was also increased. This might be related to more complicated Auger processes due to the formation of Mn oxides.

According to Auger analysis for the same sample, Fig. 5.2b corresponds to as much as 20% of oxygen in Mn. It was noticed that after ~1 hour of XPS measurements, the Mn $2p_{3/2}$ peak

Fig. 5.2. Mn XPS $2p_{3/2}$ peaks showing different oxidization status. (a) Mn $2p_{3/2}$ peak taken just after the Mn growth. (b) Mn $2p_{3/2}$ peak taken 5 hours later (including ~3 hours XPS measurements). (c) The superposition of (a) and (b). The pass energy used was 50eV for both (a) and (b).

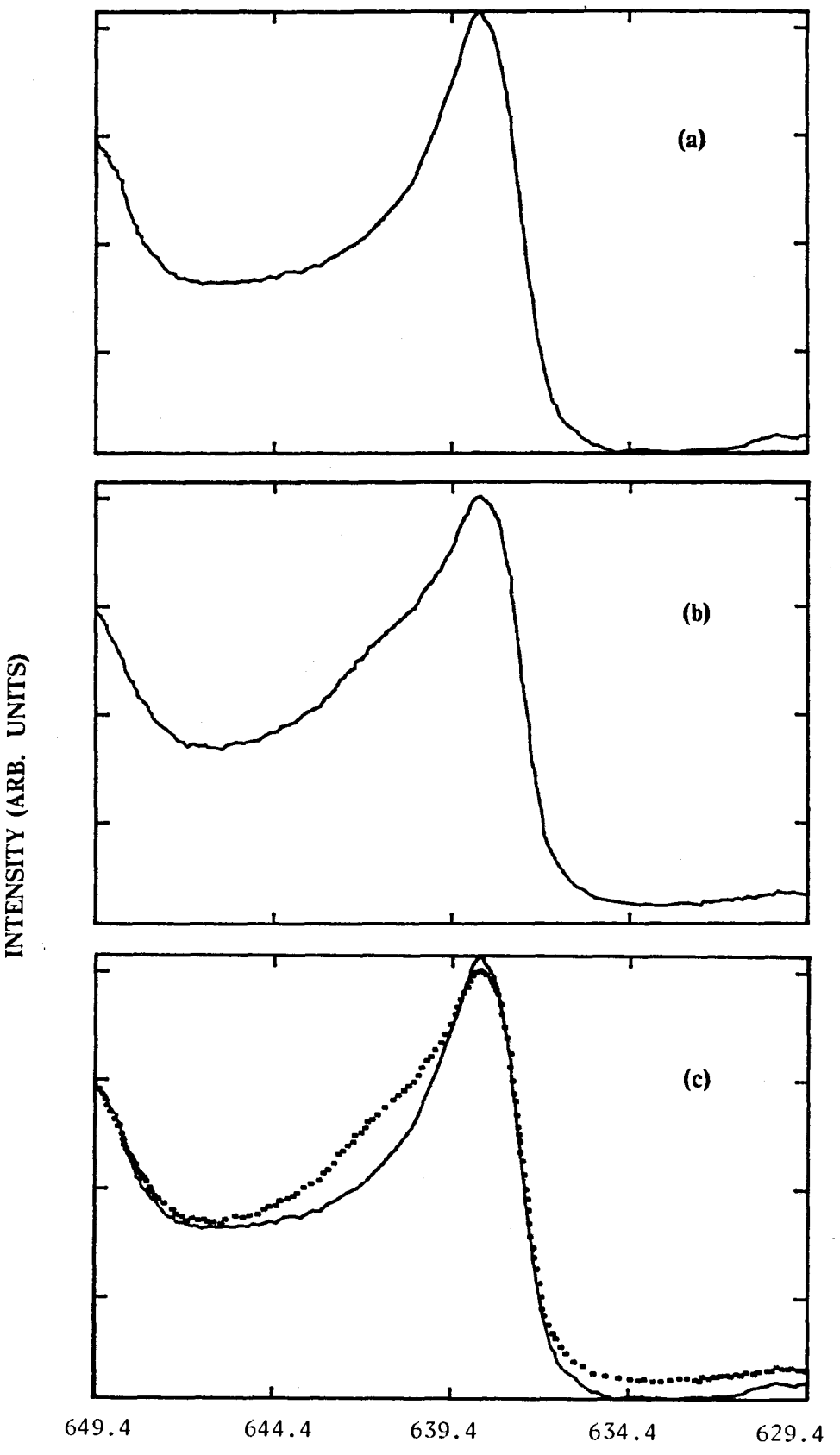
(a)
(b)
(c)
INTENSITY (ARB. UNITS)
649.4
644.4
639.4
634.4
629.4
BINDING ENERGY (eV)

essentially looked the same as that in Fig. 5.2a, although the sample contained ~10% of oxygen. It was also noticed that two layers of Mn on Ru right after the growth showed ~7% of oxygen in Mn according to AES. This might suggest that at the begining of the oxygen absorption, most of the adsorbed oxygen atoms might be still in the atomic form so that they will not show up in the Mn $2p_{3/2}$ peak. According to these ideas, the Mn $2p_{3/2}$ peak was always closely watched and XPS measurements were limited to the time before any noticeable change in the $2p_{3/2}$ peak, which is usually about one hour.

5.2 Mn 3s Peak Exchange Splittings

Due to the 3s-3d exchange interaction, the XPS 3s peak exchange splittings of the first row of transition metals are very sensitive to the spin polarization of 3d electrons. Thus by systematically studying the 3s peak splittings people can gain an insight into the understanding of magnetism and the magnetic status of the material. For this purpose, we have thoroughly studied the XPS 3s peaks for a number of materials, including our MBE-grown thin films, namely, the expanded Mn on Ru, the trimerized Mn on Ru, Mn on Fe, and AgMn and VMn alloys, and bulk samples of the first row of transition metals from Ti to Cu. The preparation of MBE-grown thin films has been described in previous chapters. The bulk samples were mechanically polished to a 1 μm diamond finish. They were then cleaned in UHV by cycles of Ar^+ sputtering and annealing. Most of the samples contained no impurities in the limit of AES sensitivity except that the Fe sample contained ~9% of C, α-Mn contained ~5% of oxygen and V contained ~3% of C.

Fig. 5.3 shows the results of our XPS 3s peak measurements. Narrow scans with 50 eV pass energy were used. The signals were averaged for at least 8 times using a Nicolet signal averager to increase the signal to noise ratio. Fig. 5.3a shows Mn 3s peaks in different environments, namely, (1) AgMn (~15% at. Mn) alloy on Ag on the Ru substrate, (2) ~2 layers

Fig. 5.3. (a) Mn 3s peaks for (1) AgMn (15% at.Mn), (2) 2 layers of epitaxial Mn on Ru, (3) 15 layers of epitaxial Mn on Ru, (4) 10 layers of epitaxial Mn on Fe and (5) VMn (25% at.Mn). The Cu 3s peak (dotted line) is shown for comparison. (b) The 3s peaks for Ti through Cu superimposed with the peaks aligned. All the data shown in both (a) and (b) are subjected to background subtractions.

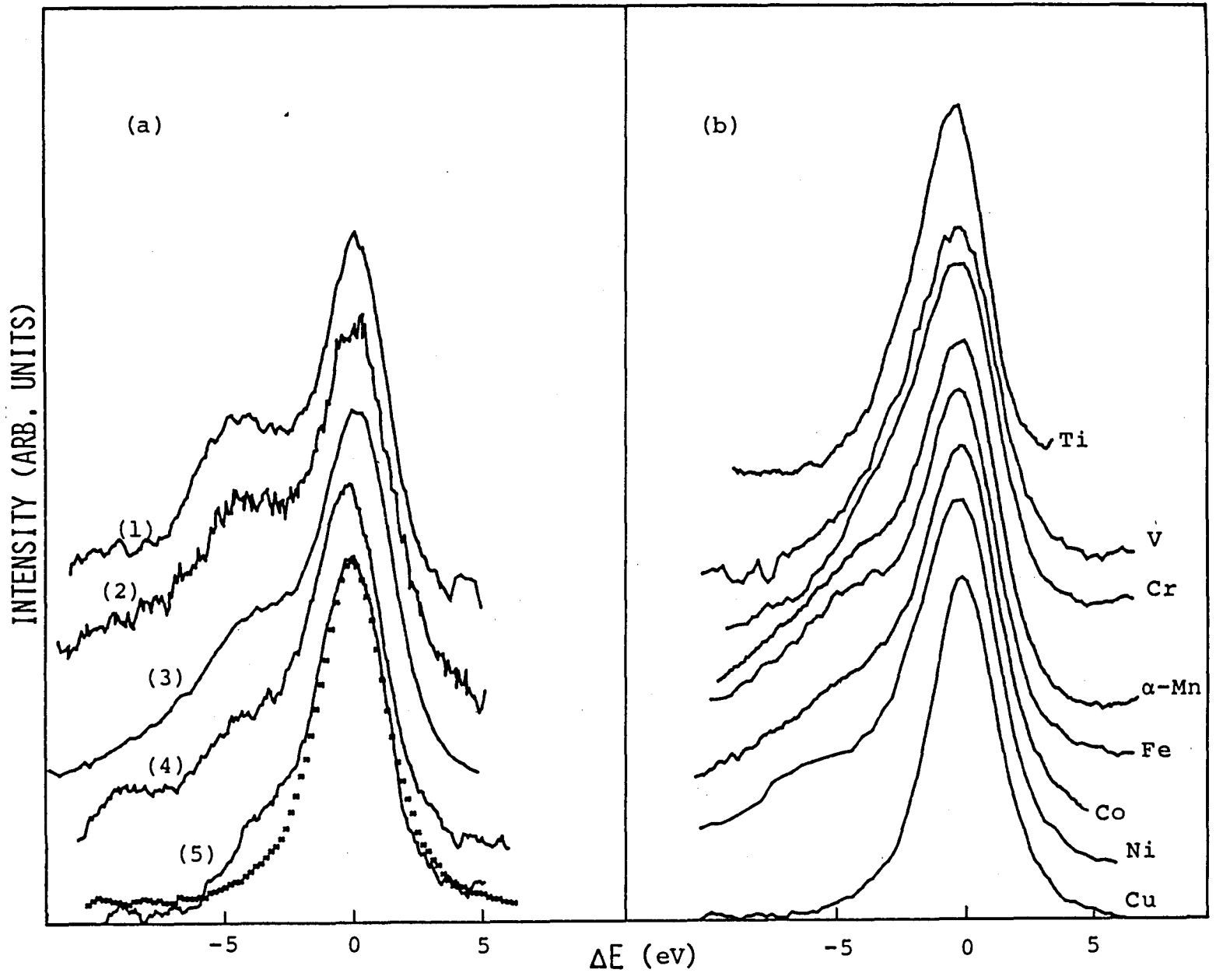
(a)
(b)
INTENSITY (ARB. UNITS)
(1)
(2)
(3)
(4)
(5)
Ti
V
Cr
α-Mn
Fe
Co
Ni
Cu
-5
0
5
-5
0
5
ΔE (eV)

of epitaxial Mn on the Ru substrate, where the Mn lattice was expanded (see Chapter 3), (3) ~15 layers of epitaxial Mn on the Ru substrate, where the Mn atoms were trimerized (see Chapter 3), (4) ~10 layers of epitaxial Mn on the Fe substrate, where, as shown by RHEED, the Mn lattice was bcc with the lattice constant of the Fe bcc lattice, (note that the bump on the left hand side is due to the Fe 3s signal), (5) VMn (~25% at. Mn) on the Ru substrate. For comparison, the normalized Cu 3s peak was added in Fig. 5.3a over the VMn 3s peak. Fig. 5.3b shows the normalized 3s peaks for Ti through Cu. The peaks are aligned for easier comparison.

All data shown in Fig. 5.3 were subjected to background subtractions. Due to the energy loss and inelastic scattering of photoelectrons in the sample and due to photoelectrons ejected by high-energy bremsstrahlung in the spectrometer, there is always a background in an original XPS spectrum. To obtain information about the intensity of an XPS peak, it is necessary to subtract the background from the original data. As proposed by Shirley (1972) and explained in detail by Seah (1983), the background intensity at an energy point in the peak can be considered to be proportional to the peak area above the background to the higher kinetic-energy side of that point. This idea is based on the fact that the more higher-kinetic-energy photoelectrons, the more intense the background. According to this idea, a computer program was developed (shown in Appendix E, thanks are due to Dr. Heinrich and Mr. Urquhart for the program) to subtract background from the original data. Fig. 5.4 shows an example of such a background subtraction for Cu 3s XPS data. Fig. 5.4a shows the original Cu 3s peak. Fig. 5.4b shows that a reasonable region was chosen for the background subtraction. This region is crucial and care should be taken to make sure that the background subtraction will not distort the peak. Usually it is chosen between the flat area on both sides of the peak. A straight line (so-called baseline) was drawn (as shown in Fig. 5.4b) as the first approximation. Then corrections for each point on the baseline were made according to the integrated area above the baseline to the lower binding energy side of that point. The final background curve was determined by iteration and is shown in Fig. 5.4b by the curve around the baseline. The final peak after background subtraction is

Fig. 5.4. Diagrams showing the subtraction of background from a XPS peak. (a) Original Cu 3s peak, 50eV pass energy. (b) The selected zone and the calculated background curve of the Cu 3s peak. (c) Cu 3s peak after background subtraction.

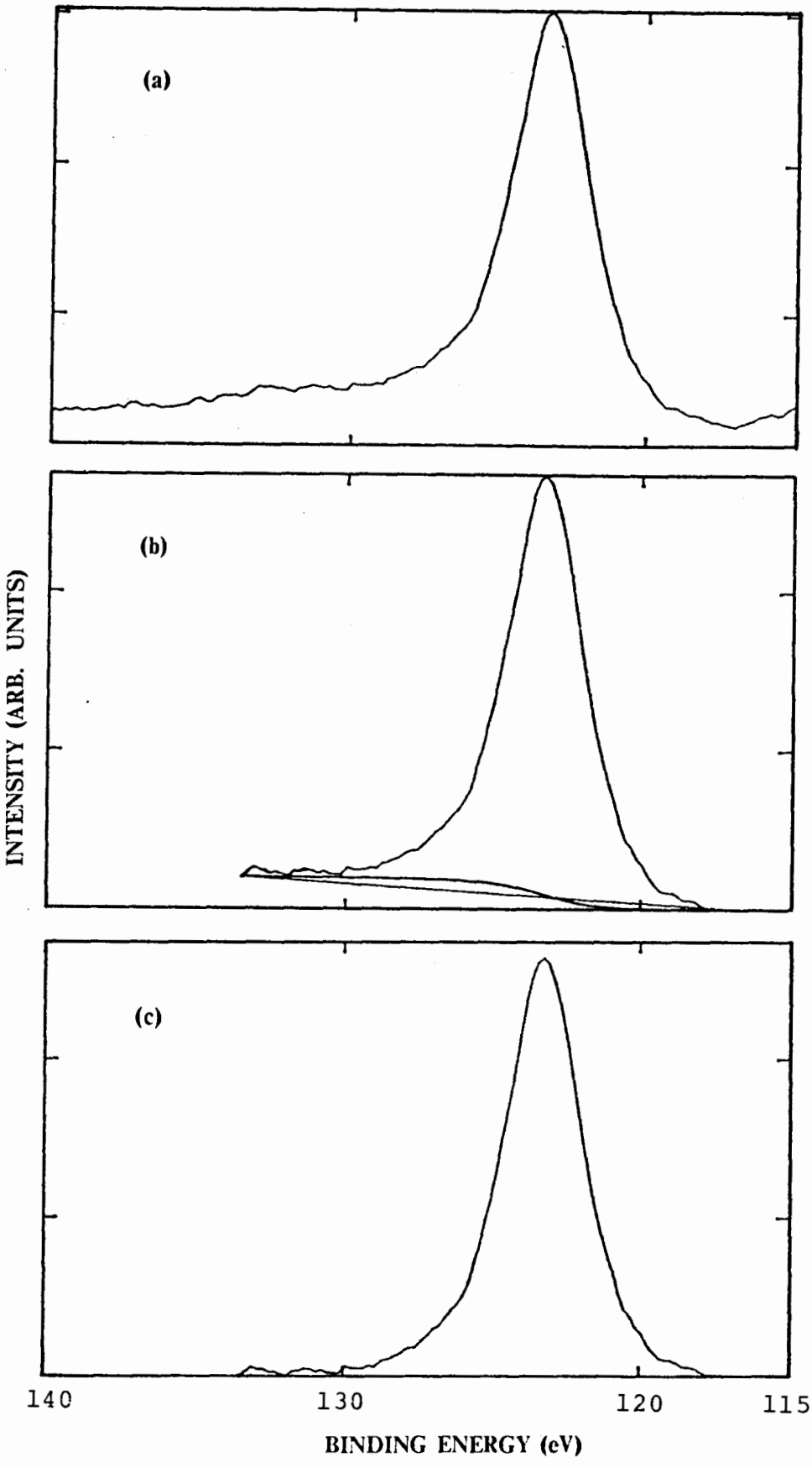
(a)
(b)
(c)
INTENSITY (ARB. UNITS)
140
130
120
115
BINDING ENERGY (eV)

shown in Fig. 5.4c.

This method of background subtraction was also applied to the spectra (2)–(4) shown in Fig. 5.3a. For the spectra of the transition elements Ti through Ni (Fig. 5.3b), the intensity on the lower binding energy side is actually higher than that on the higher binding energy side. Presumably this is due to some hidden plasmon peaks of 3p core level excitation. The above mentioned technique thus might be not suitable for the present case. Alternatively, we decided to simply subtract a flat background using the lowest flat area on the higher binding energy side as the reference. To justify this, wider scans of 50 eV or 100 eV were measured and the line shapes were studied. It was found that a flat background is quite reasonable for 3s peaks in 3d transition metals. In contrast, for 2p or 3p peaks, Shirley's method of background subtraction is needed.

For AgMn and VMn alloys, the Mn 3s peak is accompanied by Ag 4s and 4p peaks or V 3s peaks. In these cases, the Mn 3s peaks were obtained by subtracting the Ag or V background. Fig. 5.5 shows the process of such a background subtraction for AgMn (17% at. Mn). First of all, a pure Ag signal in the same energy range was recorded and smoothed. Then the smoothed data were scaled to match the 4s and 4p peaks in the AgMn data (we assume that at positions of Ag 4s and 4p peak, the Mn 3s intensities are essentially zero). The Mn 3s signal is then simply what is left after the subtraction of the Ag signal from the AgMn signal. Since both sides of the remaining Mn 3s peak reach zero intensity rather fast, no further background subtraction is needed. The computer program for this kind of background subtraction is shown in Appendix E. The Mn 3s peak for VMn (25% at. Mn) (Fig. 5.3a (5)) was obtained in a similar manner.

For the 2-layer Mn on Ru case, since the Mn overlayer was so thin, the Ru 4s and 4p signals also showed up in the original spectrum. They were subtracted by using the same method just mentioned. The remaining background was again subtracted using Shirley's method.

Fig. 5.5. A diagram showing the process of subtracting Ag background from the AgMn XPS signal. The lowest curve is the smoothed Ag background. The top curves are the original AgMn signal and the scaled Ag background.

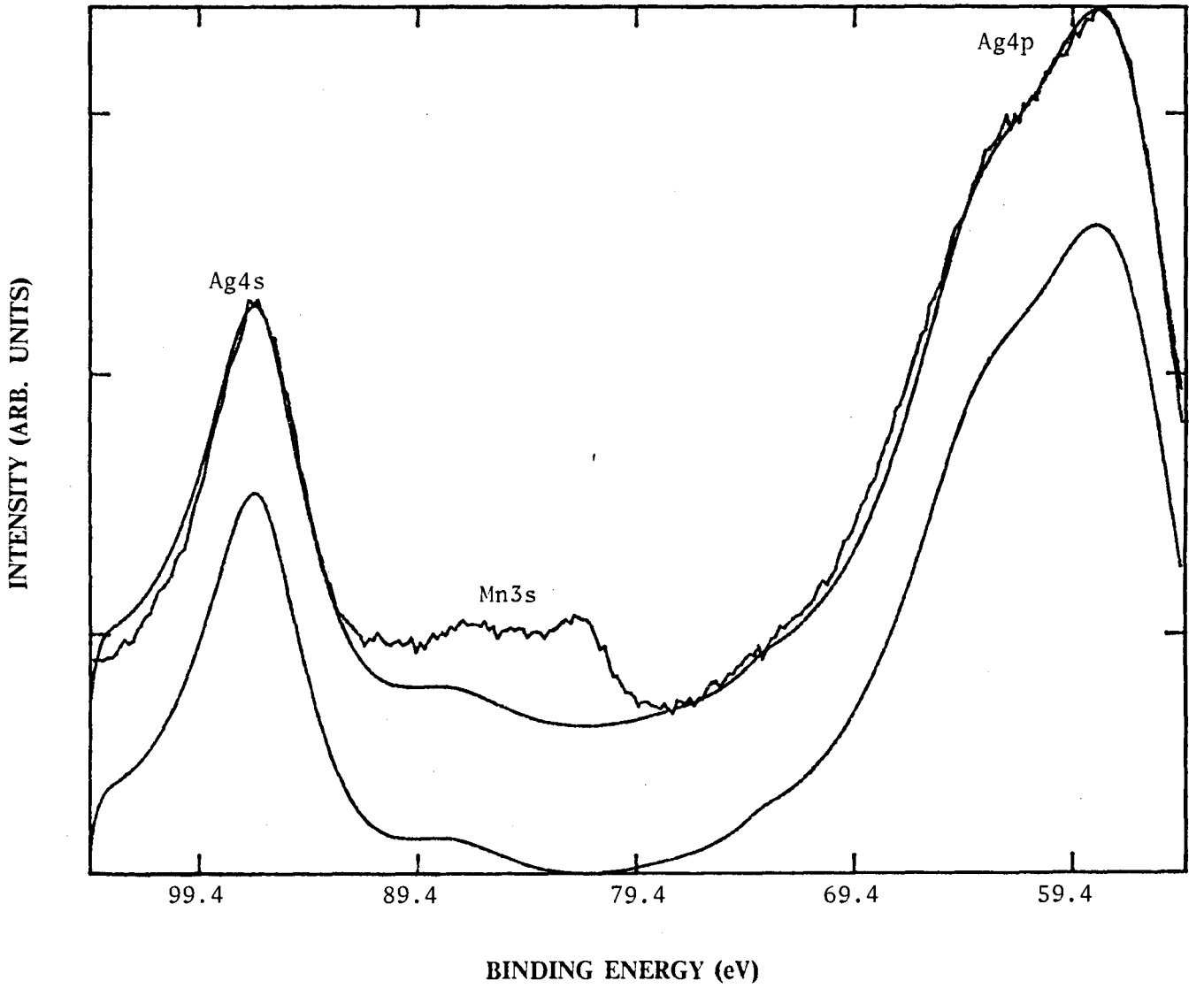
Ag4p
Ag4s
Mn3s
INTENSITY (ARB. UNITS)
99.4
89.4
79.4
69.4
59.4
BINDING ENERGY (eV)

The background subtraction is a non-trival matter and should be carried out with great care. We have tried our best by overviewing the wider spectrum and selecting the right region for background subtraction. Also we have tried to do this in a consistent way to minimise the introduced error.

By comparing the spectra shown in Fig. 5.3, one can see that the satellite intensity of the main 3s peak varies from sample to sample and the energy splittings are also slightly different. Among these spectra, the Cu 3s peak has basically no splitting. This is not surprising, because Cu has a filled d shell. It is thus reasonable to subtract the Cu 3s peak from the other spectra and compare the remaining satellite peaks. The results of such a treatment are shown in Fig. 5.6.

Fig. 5.6 and Fig. 5.3 have a one to one correspondence except that Fig. 5.3b is now split into two subdiagrams ((b) and (c) in Fig. 5.6) after subtracting the Cu 3s peak. The Cu 3s peak was first normalized to the height of the main 3s peak in each spectrum shown in Fig. 5.3 and shifted with the lower binding energy edge aligned, and then subtracted. We have neglected the small differences in the peak position in Fig. 5.3a, i.e., we simply subtracted the dotted line from all five lines in Fig. 5.3a without further aligning the Cu peak for every individual peak. It can be seen from Fig. 5.6a that the satellite peaks for the 2 layers of Mn on Ru and AgMn (15% at. Mn) have the same intensity and their intensities are the highest compared to the others. The trimerized Mn on Ru and Mn on Fe have weaker intensities. The VMn (25% at. Mn) has the smallest 3s satellite peak. These features are compared with that of the 3d transition metal elements shown in Fig. 5.6 (b) and (c), where α-Mn and Fe have the strongest 3s satellite peak and the elements on both sides of Mn and Fe have weaker satellites. This fact leads us to believe that the 3d spin polarization is related to the intensity of the 3s satellite peak.

The energy splittings of these 3s satellites follow the same trend as their intensities, i.e., decreasing from AgMn and expanded Mn on Ru to trimerized Mn on Ru and Mn on Fe to VMn. The results of energy splitting as measured from Fig. 5.6 (measured from $\Delta E=0$ to the satellite peak positions) are shown in Table 5.1. Further discussions will be given in later

Fig. 5.6. XPS 3s satellite peaks for (a) Mn in different enviroments: (1) (dotted line) AgMn (15% at.Mn), (2) 2 layers of Mn on Ru, (3) 15 layers of Mn on Ru, (4) 10 layers of Mn on Fe and (5) VMn (25% at.Mn), (note that (1) and (2) have the same intensity, note also that in (4) the bump on the left hand side is due to the Fe 3s signal), (b) α-Mn, Fe, Co and Ni and (c) α-Mn, Cr, V and Ti. These spectra were obtained by scaling and then subtracting the Cu 3s peak from the main 3s peaks shown in Fig. 5.3. α-Mn data was repeated in (b) and (c) for easier comparison of the scale in (b) and (c).

(a)
(b)
(c)
(1)
(2)
(3)
(4)
(5)
α-Mn
Fe
Co
Ni
α-Mn
Cr
V
Ti
-5
0
5
ΔE (eV)
INTENSITY (ARB. UNITS)

Samples	AgMn (15%at.Mn)	2 layers Mn on Ru	15 layers Mn on Ru	10 layers Mn on Fe	VMn (25%at.Mn)
Splittings	4.5	4.3	4.1	4.1	3.4

Samples	Ti	V	Cr	α-Mn	Fe	Co	Ni
Splittings	2.2	2.8	3.0	3.8	3.8	3.7	2.8

Table 5.1. Energy splittings (eV, ±0.1eV) of 3s peak for Mn in different environments and for elements Ti through Ni.

sections.

5.3 Curve Fittings Using the Doniach-Sunjic Lineshape

As introduced in Section 2.3.2, Doniach and Sunjic (1970) have presented a formula (Eq. (2.3-4)) to describe XPS lineshapes of metals. We have applied their theory to fit our data. To account for the instrumental resolution, we have added to the program (thanks are due to Dr. Heinrich for the program) a Gaussian line broadening function. The programs are shown in Appendix E. The Gaussian parameter σ was obtained by comparing the measured Ag $3d_{5/2}$ peak (which is very narrow) with a Gaussian lineshape. The measured FWHM (Full Width at Half Maximum) of the Ag $3d_{5/2}$ peak was 1.10 eV for 25eV pass energy, 1.60 eV for 50 eV pass energy and 2.75 eV for 100 eV pass energy. Thus the corresponding σ's would be 0.47, 0.68 and 1.17 respectively. To check the program, we have calculated the line shape using these parameters and a very small γ (between 0.001 to 0.045) and obtained the FWHM's which are what we expected.

Using the program we have fitted the Mn 3s and $2p_{3/2}$ peaks for the trimerized Mn (~15 layers Mn on Ru), the expanded Mn (~2 layers Mn on Ru) and AgMn (~17% at. Mn). The fittings together with the measured data are shown in Fig. 5.7. The data shown in Fig. 5.7 are subjected to background subtractions, which have been described before. The smooth lines are computer fits, where the decomposed individual peaks are also shown. The fitting parameters are shown in Table 5.2. Most of these parameters have been defined already in Eq.(2.3-4). σ is the Gaussian parameter discussed in the previous paragraph. R_{12} is the intensity ratio of peak 1 to peak 2. The intensity of each calculated peak is taken as the total area under that peak. And E's are represented as relative peak positions with respect to the main peak position in the trimerized Mn.

Fig. 5.7. Computer curve-fittings by using the Doniach-Sunjic theory for Mn 3s ((a), (b) and (c)) and $2p_{3/2}$ ((d), (e) and (f)) peaks in the trimerized structure ((a) and (d)), in the expanded structure ((b) and (e)) and in the AgMn (17% at.Mn) ((c) and (f)). The pass energies used were 25eV for (d) and (f), 50eV for (a), (b) and (e), and 100eV for (c). The smooth lines are computer fits.

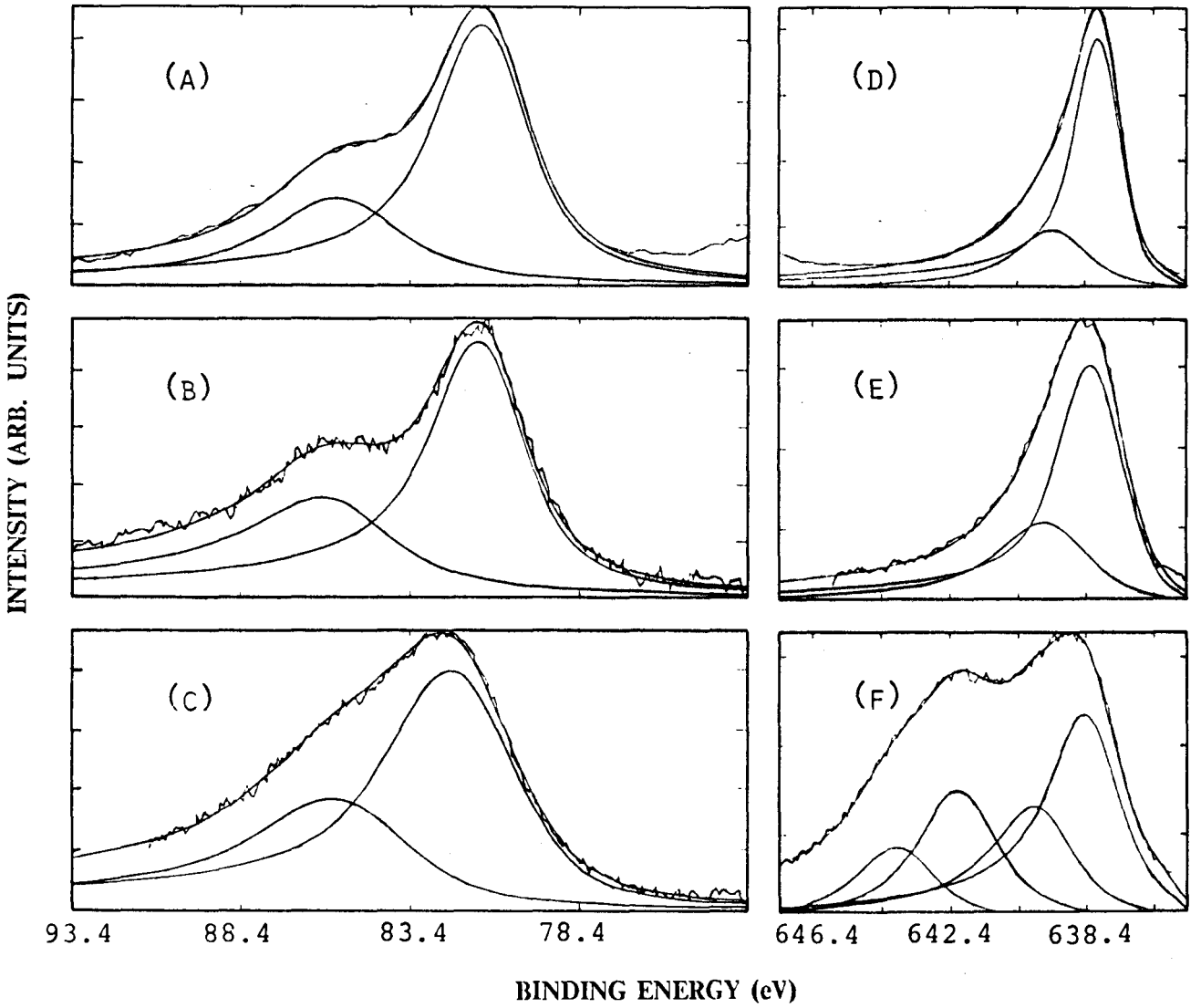
(A)
(B)
(C)
(D)
(E)
(F)
INTENSITY (ARB. UNITS)
93.4
88.4
83.4
78.4
646.4
642.4
638.4
BINDING ENERGY (eV)

3s peak	E_1	E_2	$2\gamma_1$	$2\gamma_2$	a_1	a_2	σ	R_{12}
Trimerized Mn	0.00	4.30	2.4	3.9	0.10	0.10	0.68	2.4
Expanded Mn	0.05	4.32	2.3	3.1	0.13	0.22	0.68	1.8
AgMn	0.72	4.02	2.2	3.1	0.15	0.21	1.17	1.8
$2p_{3/2}$ peak	E_1	E_2	$2\gamma_1$	$2\gamma_2$	a_1	a_2	σ	R_{12}
Trimerized Mn	0.00	1.33	0.7	2.0	0.16	0.11	0.47	2.2
Expanded Mn	0.16	1.48	0.8	2.0	0.16	0.16	0.68	2.1
AgMn	0.38	1.84	1.8	2.2	0.15	0.16	0.47	1.6
	E_3	E_4	$2\gamma_3$	$2\gamma_4$	a_3	a_4	σ	R_{34}
AgMn	4.18	5.98	2.3	2.4	0.05	0.07	0.47	1.7

Table 5.2. Parameters used in the fittings shown in Fig. 5.7, where E's (in eV) are relative peak positions, γ's (in eV, ±0.1eV) are the lifetime parameters, a's are the asymmetry parameters and R_{ij} (±0.1) is the area ratio of peak i to peak j, and σ is the Gaussian parameter.

From Fig. 5.7, it can be seen that the fittings are quite satisfictory. The parameters shown in Table 5.2 are also reasonable. It is worthwhile to mention that the ratios of the Mn 3s doublets in the expanded Mn and in the AgMn (17% at. Mn) are equal (both are 1.8 ± 0.1). This result is exactly what we obtained by the subtracting the Cu 3s peak from the Mn 3s peak for the expanded Mn and AgMn (15% at. Mn) (see Fig. 5.6 and Section 5.2). It is also interesting to note that the AgMn data shown in Fig. 5.6 and Fig. 5.7 are from two different experiments and the pass energies used are also different (100 eV and 50 eV respectively). The 2-layer Mn on Ru data in both Fig. 5.6 and Fig. 5.7 are the same set of data.

The intensity ratio of 1.8 for the Mn 3s doublets in the expanded Mn and the AgMn alloy is comparable with what Kowalczyk *et al.* (1973) got for MnF_2 ($\sim$2.0).

It was noted that the AgMn (17% at. Mn) $2p_{3/2}$ data shown in Fig. 5.7f can not be fitted by two or three Doniach-Sunjic peaks with resonable parameters. To make sure about this, a Minuit program (from Mr. Urquhart) was used. It was found that no reasonable fitting could be obtained when we used just two or three peaks. Minuit is a program which allows the computer to choose automatically the best parameters to fit the data. We are thus convinced that we need four Doniach-Sunjic peaks for the AgMn (17% at. Mn) data. As shown by Steiner *et al.* (1980), the second set of peaks (E_3 and E_4) comes from those Mn ions which have a perfect Ag environment. The physical origin of these new peaks is still an open question.

As introduced in Section 2.3.3, Veal and Paulikas (1983) proposed a two-channel screening mechanism and argued that for a pure screening-caused splitting, the splitting in the 2p peak can be used to predict the splitting in the 3s peak. We have used our program to check this idea for the case of Ni. Ni core-level satellites have been extensively studied for over a decade. It is thus of interest to see how these satellites and main peaks fit the Doniach-Sunjic lineshape. Fig. 5.8 shows such fits for Ni $2p_{3/2}$ and 3s peaks, where the data shown are subjected to background subtractions as described in Section 5.2. The parameters used are shown in Table 5.3.

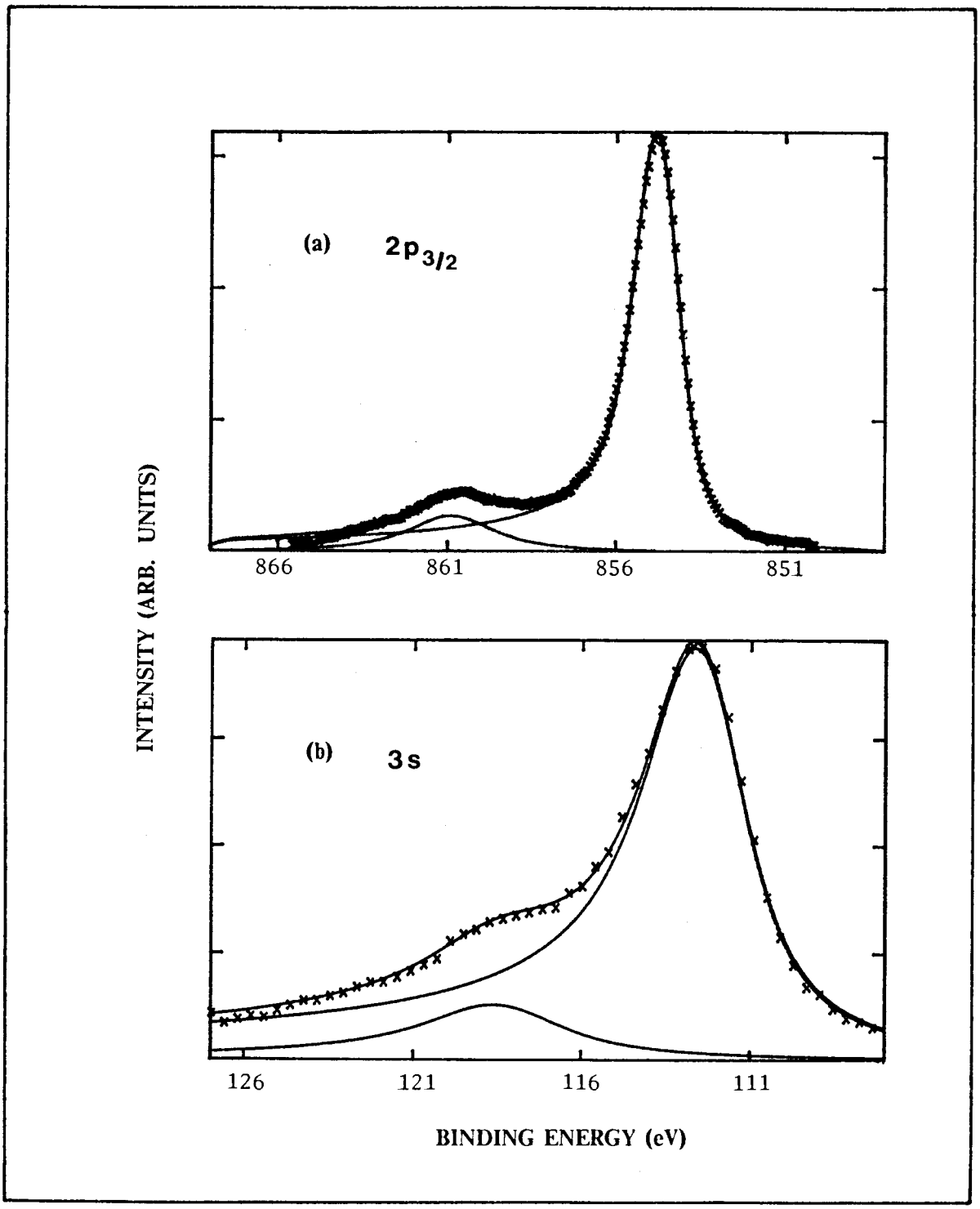

Fig. 5.8. Doniach-Sunjic lineshape fittings (solid lines) for Ni $2p_{3/2}$ and 3s peaks (dotted lines). The pass energies were 25eV for $2p_{3/2}$ and 50eV for 3s peaks.

Peak	E_1	E_2	ΔE	$2\gamma_1$	$2\gamma_2$	a_1	a_2	σ	R_{12}
$2p_{3/2}$	854.75	860.90	6.15	0.88	2.80	0.12	0.00	0.47	6.6
3s	112.39	118.40	6.01	2.72	4.40	0.17	0.10	0.68	6.0

Table 5.3. Parameters used in computer fits for Ni $2p_{3/2}$ and 3s peaks shown in Fig. 5.8, where E_1 and E_2 are peak positions (binding energy, eV) of the main peak and the satellite peak, ΔE is the energy splitting, γ_1, γ_2 are the lifetime parameters (eV), σ is the Gaussian parameter and R_{12} is the area ratio of the main peak to the satellite peak.

From Fig. 5.8 and Table 5.3, it can be seen that both the energy splitting and the intensity ratio of the main peak to the satellite peak are very close for the $2p_{3/2}$ and 3s peaks. The ~6 eV splittings in both $2p_{3/2}$ and 3s peaks agree with the excitation energy calculations, using a two-channel screening model, by Martensson and Johansson (1980). This fact together with the very close intensity ratios (6.6 ± 0.2 and 6.0 ± 0.2) suggest that Veal and Paulikas' idea is somewhat justified. Due to the exchange interactions (although quite weak in Ni), the splittings in 3s and 2p should not be exactly the same. This accounts for the small differences in ΔE and R_{12} as well as for the differences in other parameters. (Note that the overall difference in the linewidth of 3s and 2p peak is mainly due to the lifetime effect). The small exchange splitting in the 3s peak might hide in the asymmetric side of both the main and the satellite peaks, and accounts for the 3s peak lineshape (Fig. 5.8b) and the larger α parameters.

If we apply this idea of a two-channel screening mechanism to cases of the trimerized Mn and the expanded Mn (Fig. 5.7 and Table 5.2), we can see that the satellite of the 3s peak is mainly due to the exchange interaction. The decomposed splitting in $2p_{3/2}$ peak is small (~1.3 eV) and might be due to the two-channel screening mechanism. If so, the two-channel screening effect in 3s peak might be hidden in the asymmetric part of the main and the satellite peak. To find out the possibility of this picture for the case of Mn, we have used the Doniach-Sunjic lineshape to refit the trimerized Mn and the expanded Mn 3s data with four peaks. The peak positions were determined mainly according to the above argument, as described below. The main peak was taken as the local screening case. The splitting due to the non-local screening was determined according to the 2p peak splitting, which was ~1.3 eV (Table 5.2). The splitting determined in Fig. 5.7 (~4.3 eV) was taken as the exchange splitting under the fully screened conditions, i.e., corresponds to a d^6 final state. Then according to Eq. (2.3-6), the exchange splitting under the non-local screening conditions (a d^5 final state) should be ~5.2 eV. Other parameters were varied to give the best fit. The fit is shown in Fig. 5.9 and the parameters are listed in Table 5.4. From Fig. 5.9, we can see that by using the above argument, we can fit the

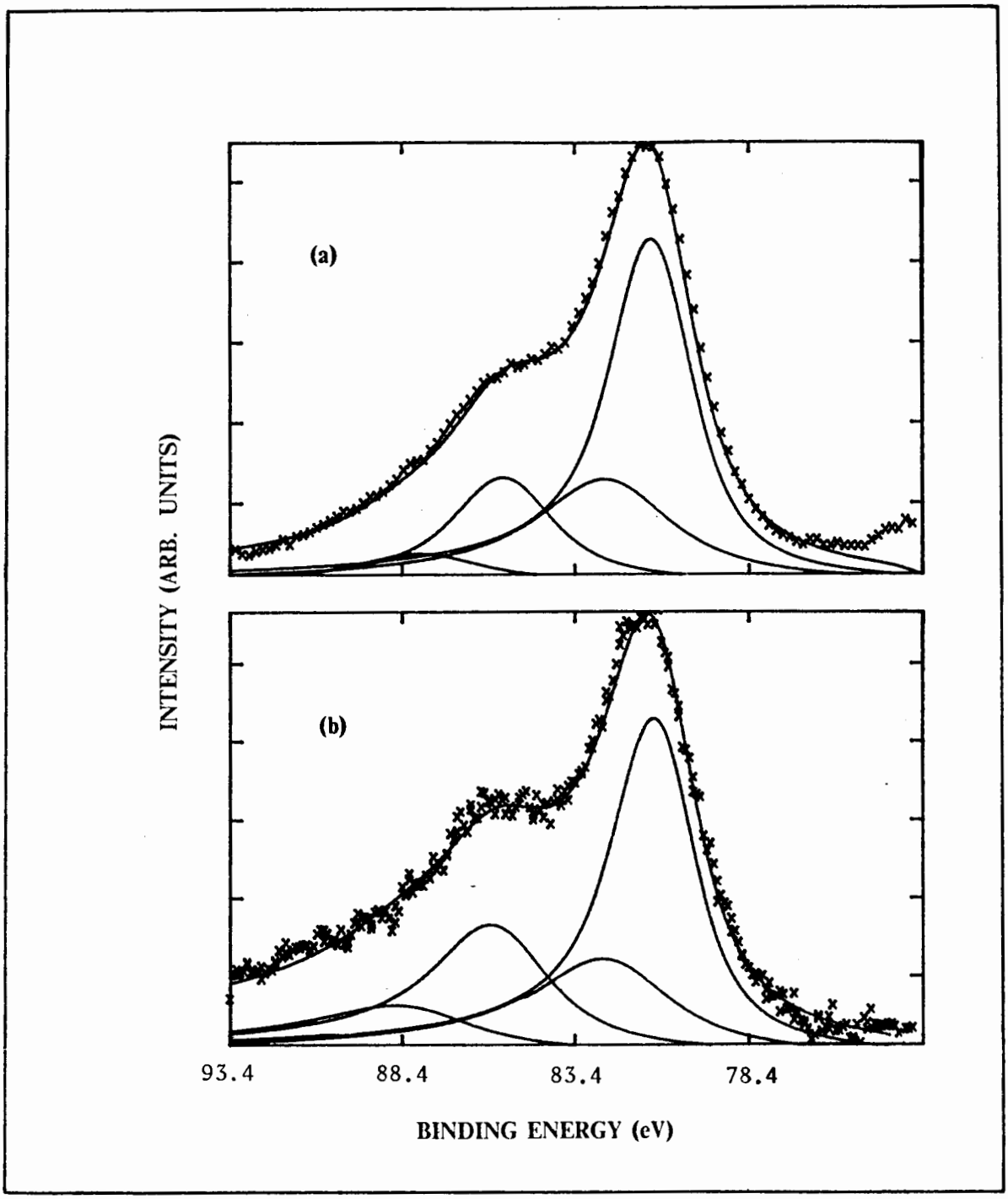

Fig. 5.9. 4-peak Doniach-Sunjic lineshape fittings for the Mn 3s peak in the trimerized structure (a), and in the expanded structure (b).

Sample	E_1	E_2	E_3	E_4	$2\gamma_1$	$2\gamma_2$	$2\gamma_3$	$2\gamma_4$
Trimerized Mn	0.00	1.30	4.30	6.70	2.0	4.0	2.8	4.0
Expanded Mn	0.05	1.30	4.50	6.90	2.0	4.0	3.2	4.4

Sample	a_1	a_2	a_3	a_4	R_{13}	R_{24}	R_{12}	R_{34}
Trimerized Mn	0.08	0.08	0.05	0.05	2.7	3.5	2.1	2.8
Expanded Mn	0.10	0.12	0.14	0.26	1.8	1.8	2.2	2.0

Table 5.4. Parameters used in the fittings shown in Fig. 5.9, where E's (in eV) are relative peak positions, γ's (in eV, ±0.1eV) are the lifetime parameters, a's are the asymmetry parameters and R_{ij} (±0.1) is the area ratio of peak i to peak j. The Gaussian parameters used are all 0.68.

data quite well. For the parameters, we can see that the intensity ratio R_{12}'s (screening splitting) for $2p_{3/2}$ peak (Table 5.2) and for 3s peak (Table 5.4) are in excellent agreement, and indicates that the local and non-local screenings are indeed quite similar for the $2p_{3/2}$ and 3s peaks. The intensity ratio for the exchange splittings (R_{13} and R_{24}) agrees well with that in the 2-peak fittings (Table 5.2) for the case of the expanded Mn and not that well for the case of the trimerized Mn. Note that in both 4-peak and 2-peak fittings, the intensity ratio of the exchange splitting is smaller for the case of the trimerized Mn compared to the case of the expanded Mn, i.e., the relative intensity of the satellite in the trimerized Mn is smaller compared to that in the expanded Mn. For the γ's, we noticed that the main peaks (peak 1) are much narrower than the satellite peaks. And the α's differ quite a bit from peak to peak. This might indicate that more complicated factors exist beyond the present simple model. As a matter of fact, Kowalczyk *et al.* (1975) pointed out that multiplet splittings exist for Mn 2p and 3p peaks in MnF_2. Thus it is likely that the Mn $2p_{3/2}$ in our case has also multiplet splittings. However, we believe that this effect is small and the splitting is dominated by the two-channel screening mechanism. This judgement should be verified for Mn by similar calculations as Martensson and Johansson (1980) did for Ni and Veal and Paulikas (1983, 1985) did for transition metal compounds. Up-to-date such a calculation is not available. But Antonides *et al.* (1977) measured the effective Coulomb interaction between two 3d holes on the same atomic site, U_{eff}, for Ni, Fe and Co *etc.* and found that U_{eff}=4.1eV for Ni, U_{eff}=1.1eV for Fe and U_{eff}=1.2eV for Co. We thus speculate that the ~1.3eV splitting in Mn $2p_{3/2}$ peak and the ~6eV splittings in Ni might have a similar physical origin.

The physical picture behind Fig. 5.9 is summarized as follows. The main peak is the fully screened (local screening) final state. ~1.3eV higher (in binding energy) is the peak corresponds to the nonlocal screening final state. ~4.3eV away from the main peak is the satellite peak due to the exchange splitting of the local screening state. ~5.2eV away from the nonlocal screening peak is the satellite peak due to the exchange splitting of the nonlocal screening state. The effects of

other multiplets are neglected from the above picture. Since the nonlocal screening satellites are small, we can also ignore them, leading to a picture of the 2-peak fittings (Fig. 5.7). It is thus concluded that the 3s peak splitting for the case of Mn is mainly due to the exchange splitting. In the case of Ni, the splitting is dominated by the two-channel screening effects.

In general the above Doniach-Sunjic lineshape fittings agree quite well with the observations we discussed in Section 5.2. This will be helpful in our understanding of the 3s splittings and the 3d spin polarization, which we discuss below.

5.4 Discussions

5.4.1 XPS 3s peak splittings and the 3d spin polarization

As mentioned before, the 3s multiplet splittings are directly related to the 3d spin polarization of the sample atom. Our experiments showed however, that the energy splitting of the 3s peak for Mn atoms in various environments is almost independent of the spin state deduced by thermodynamic measurements of susceptibility and specific heat. The intensity of the satellite peak on the other hand, is sensitive and correlated with the thermodynamic measurements. This correlation is not complete since some intensity remains for the satellite peak for Mn in V where there is no indication of a thermodynamic spin degree of freedom. This is to be explained in terms of spin quantum fluctuations and the surface-induced volume effect. The latter will be discussed in the next section.

To understand the quantum fluctuations, let us examine the quantum states involved in the photoemission process of the excitation of a Mn 3s electron. The initial ground state is $3s^2 3d^5$ ($S=5/2$). The final states for a high spin 3d shell should be $3s^1 3d^6$ ($S=5/2$) or $3s^1 3d^6$ ($S=3/2$) depending on whether the remaining 3s electron has its spin parallel or antiparallel to the 3d spin polarization (Here we consider only the fully screened case where the excited 3s electron effectively goes into a 3d level. The nonlocal screening is neglected). There might be also low

spin 3d shells where the 3d spins are randomly averaged in times short compared to the XPS measurement time. In that case, the exchange splitting will be small and most of the intensity will be at the position of the main peak. Thus the exchange splitting is mainly due to the high spin state. The contributions from the low spin state to the main peak might explain why the measured intensity ratio of the main peak to the satellite peak is always higher than what people expected from the theory (Eq. (2.3-7)). For the high spin state, the two final states (S=5/2 and S=3/2) correspond to the main and the satellite peak respectively. The one with S=5/2 corresponds to the case where the excited 3s electron goes into the 3d level without "flipping" of its spin. The other one with S=3/2 however, has the spin of the excited 3s electron "flipped". The "flipping" of spin occurs in an exchange field of 4 μ_B and needs a certain energy. Thus the S=3/2 state corresponds to the satellite peak which lies at the higher binding energy side. The S=5/2 state corresponds to the main peak. Further more, since in the case of the main peak there is no "spin-flipping", the position of the main peak should not be sensitive to the magnetic moment of the 3d shell. This has been confirmed by comparing positions of the 3s main peak and the $3p_{3/2}$ peak for 3d transition elements Sc through Zn (Arrott *et al.* (1985)). The comparison is shown in Fig. 5.10. The data shown in Fig. 5.10 were taken from our measurements, the PHI handbook (Wagner *et al.* (1979)) and Shirley *et al.* (1977)'s measurements. Fig. 5.10a shows the positions and Fig. 5.10b shows the deviation of the positions from straight lines drawn through the Ti and Cu values. It can be seen from the figure that the 3s main peaks track the $3p_{3/2}$ peaks very well. The $3p_{3/2}$ peaks are not sensitive to the 3d spin polarization. This suggests that the 3s main peak is produced by those transitions where the total spin of both the initial and final states does not change. This might also be the reason why the position of the Mn 3s main peak is almost independent of the environment.

The satellite peak should depend on the magnetic moment. However, we found that the energy splitting of Mn 3s peak is very little affected by the change in environment from Mn in Ag to Mn in V. While the relative intensity of the satellite peak is more sensitive to the 3d spin

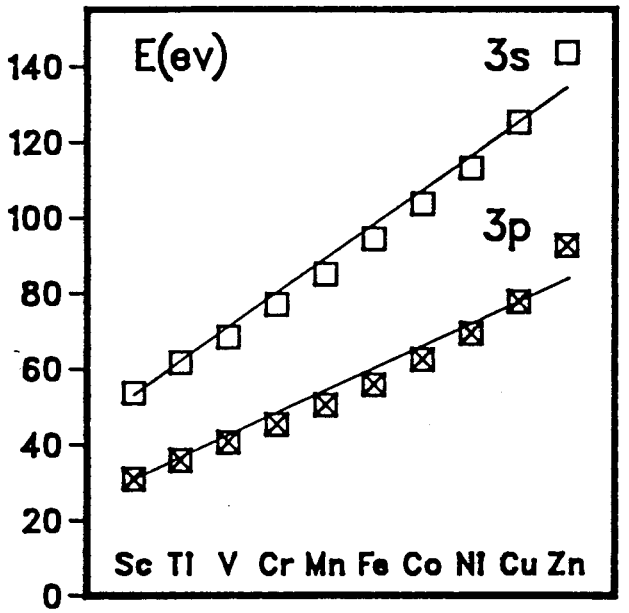

(a)

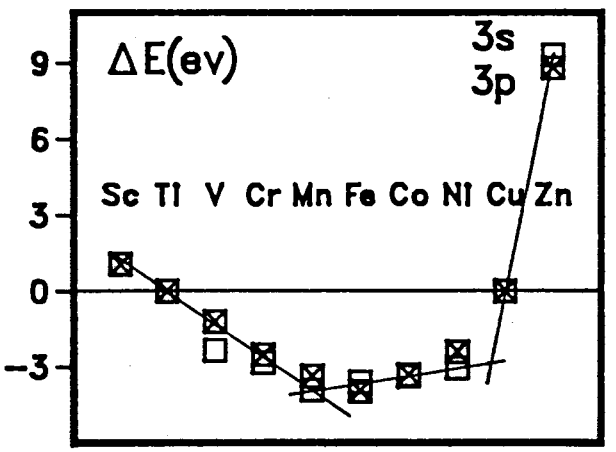

(b)

Fig. 5.10. (a) Electron binding energy for 3s and $3p_{3/2}$ peaks for elements Sc through Zn. (b) Deviation of peak positions in (a) from straight lines through the Ti and Cu values.

polarization. The satellite peak also shows up for Mn in V (although quite small). We thus speculate that on the XPS time scale of $4x10^{-15}$s, the high spin state (5 μ_B in Mn case) can always be detected, while on the time scale of 10^{-13}s, which is the case for thermodynamic measurements, this high spin state is smeared out due to the quantum fluctuations between the high and the low spin states. The intensity of the satellite peak thus represents the probability of the high spin state. The high spin state can be reflected in the thermodynamic measurement as long as the quantum fluctuation is slow enough for thermodynamic averaging to occur, e.g., to allow precession of one atom in the field of its neighbors. If the quantum fluctuations are slower than 10^{-15}s and faster than 10^{-13}s, the high spin state will be seen in the XPS but not in the thermodynamic measurements. This idea of quantum fluctuations comes from van Vleck's model (van Vleck (1953)). In the van Vleck model, a narrow band metal is treated as an ensemble of atomic states with individual configurations and numbers of electrons fluctuating rapidly. The fluctuation is due to the interaction between these atomic states.

We have presented the above argument at the 1985 ICM meeting. At the same time, Klebanoff and Shirley (1985) have used the 3s satellite intensity to show a surface–sensitive enhancement of the atomic 3d spin at the Cr(001) surface. They used angle–resolved photoelectron spectroscopy to compare the Cr 3s peak lineshape for different electron detection angles. They found that the relative intensity of the satellite peak increased as the surface sensitivity of the measurement increased. This is used as an indication of enhancement of 3d spin polarization. It was also found from their data that the energy splitting is not sensitive to the angle. The energy splitting they found is very close to what we obtained for Cr (~3.0eV in both cases, cf. Table 5.1).

The residual satellite intensity for Mn in V might also be explained in terms of surface–induced volume effect, which we discuss below.

5.4.2 Atomic size and magnetic moment

As we introduced in the begining of this thesis, the atomic size should affect the magnetic moment. As a matter of fact, the magnetic 3d transition metals are already in expanded lattices compared to other elements. This can be seen from Fig. 5.11 which shows the atomic concentration of the 3d transition elements Ti through Cu (cross dots) compared to elements Zr through Ag (box dots). The data for Zr through Ag have been scaled so that the Ag data matches the Cu data. If we compare these two sets of data, it is clear that the magnetic metals have a relatively lower density, or in another words, they are in an expanded lattice. It is of interest to compare the deviation of these two sets of data with the data shown in Fig. 5.6b. Fig. 5.6b shows the decrease in the 3s satellite intensity on both sides of Mn and Fe, while Fig. 5.11 shows that the deviation from the Zr through Ag data also decreases on both sides of Mn and Fe. This correlation might suggest that both the relative size of the atom and the relative intensity of the 3s satellite peak are related to the magnetic moment of the 3d transition metals.

Considering that the 2-layer Mn on Ru has an expanded structure and its 3s XPS data shows the same relative satellite intensity as Mn in Ag, we believe that this expanded Mn has larger magnetic moment than other forms of pure Mn.

It is also of interest to compare the atomic size for Mn in different environments. Mn in Ag as suggested by RHEED observations might have a substitutive position in Ag fcc lattice for which the nearest neighbor distance is 2.87Å. The Mn atoms might be squeezed a little by Ag atoms and thus might have a size close to that of the expanded Mn (2.7Å in diameter). Mn on Fe has a bcc structure as bcc Fe with a nearest neighbor distance of 2.48Å, which is compared with the estimated atomic size of ~2.39Å for the trimerized Mn. Comparing the relative stellite intensities (Fig. 5.6a), we see that Mn in Ag and the expanded Mn have higher satellite intensity than Mn on Fe and the trimerized Mn. This is in agreement with our speculation. The lower intensity observed in Mn on Fe compared with the trimerized Mn might be due to some other unknown factors. Since VMn on Ru did not show a well defined structure, it is hard to estimate

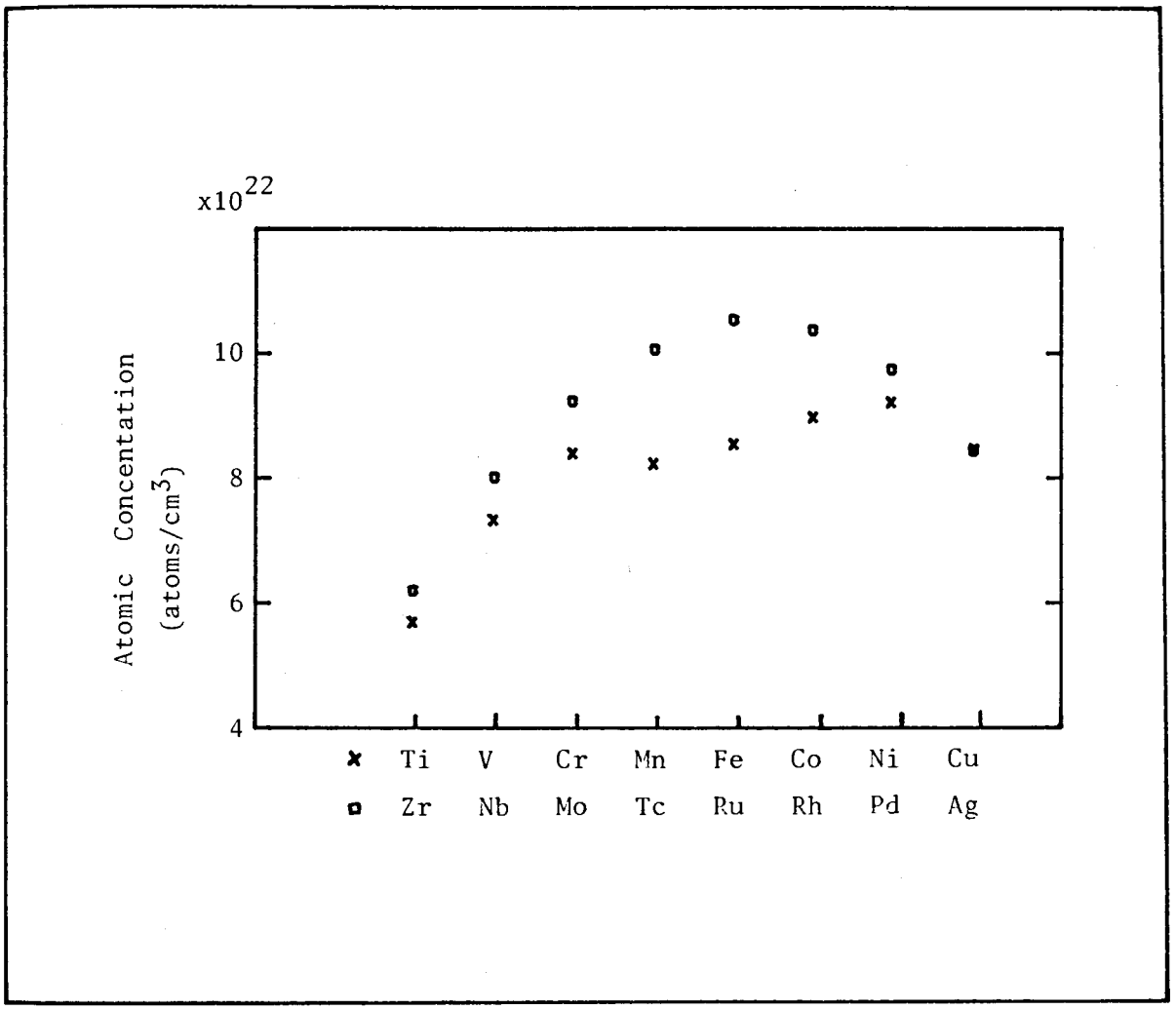

Fig. 5.11. Atomic concentration for Ti through Cu (cross dots) and Zr through Ag (box dots). The Zr through Ag data have been scaled so that the Cu and the Ag data overlap.

the atomic size for Mn in V.

We suspect that the surface Mn atoms have a larger size in all environments. This surface–induced volume effect might contribute to the satellite intensity of Mn in V. To clarify this idea, we have grown an additional V thin film (about one monolayer) on top of the VMn overlayers. To our surprise, the Mn 3s peak still showed still a clear satellite. This fact shows that the 3s satellite peak is not due to the surface–induced volume effect.

Despite this experiment on VMn, we still believe that the surface atoms should contribute more to the local magnetic moment than the bulk atoms. We speculate that the surface–sensitive enhancement of the atomic 3d spin of Cr observed by Klebanoff and Shirley (1985) might have the same physical origin. That is to say, the expanded atomic volume will allow the atom to obey Hund's rule, leading to a high spin state. This high spin state is obscured in thermodynamic measurements, where the bulk properties dominate. On the other hand, XPS measurements are surface sensitive. This together with the time scale factors might explain the observed evidence of local magnetic moment in XPS for Mn in V.

CHAPTER 6

AES STUDIES OF MN, AGMN AND VMN THIN FILMS ON RU SUBSTRATE

6.1 Introduction

Like XPS, AES is also an important tool we used for analyzing the MBE-grown thin films. The fundamental principles of AES have been introduced in Section 2.4 and AES instrumentation has been discribed in Appendix D. Its applications in analyzing the growth type, the growth rate and the compositions of binary alloys have been discussed in Section 3.2. For these applications, a derivative mode with an electron beam excitation is often used.

Fig. 6.1 shows an AES survey scan for an ~2 layers Mn on Ru sample. A 3 keV primary electron beam and a 6 eV peak-to-peak modulation were used. These kind of survey scans are what people usually use for surface chemical analysis. They are very successful in identifying chemical components and detecting impurities. For example, from Fig. 6.1, both Mn and Ru Auger signals can be clearly seen. Also, noticeable oxygen (~7% at. in Mn) is present. (This large amount of oxygen is mainly due to an electron beam stimulated oxidation process we mentioned before (cf. Section 3.2). Note that in XPS for a similar sample we did not see the evidence of oxygen within the experimental limits (cf. Fig. 5.1).) Some carbon signal can also be found from Fig. 6.1 by measuring and comparing the ratio of the bottom part and the top part of the Ru 273eV peak (cf. Section 3.2). No other impurities were found from Fig. 6.1.

Despite the success of these applications, this kind of AES has serious limitations in physical analysis. This is mainly due to its low energy resolution (usually several eV). Even worse, inelastic back-scattering of the primary electron beam further smears out the lineshape information of the useful signal.

Fig. 6.1. An AES survey scan for a ~2 layers Mn on Ru sample. The primary electron beam energy was 3 keV. The modulation used was 6eV peak to peak.

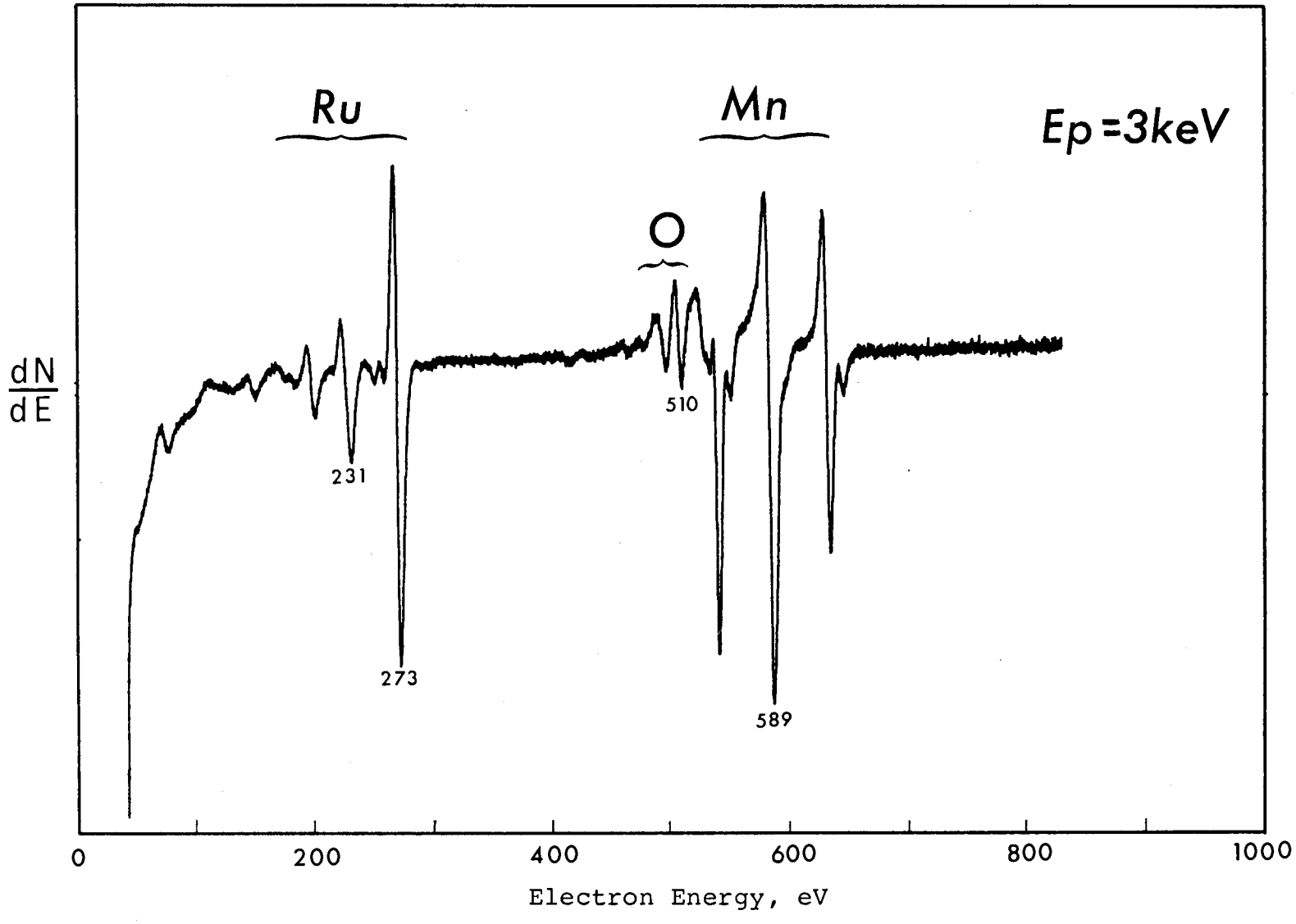
Ru
Mn
O
Ep=3keV
dN/dE
231
273
510
589
0
200
400
600
800
1000
Electron Energy, eV

On the other hand, the Auger spectrum people observed in XPS (or the so-called x-ray excited AES) has much better energy resolution. This is because if one uses x-ray excitation, a retarding potential can easily be added to the electron energy analyzer. This retarding potential provides a constant pass energy for photoelectrons and Auger electrons, leading to a much higher resolution (cf. Appendix C). This pre-retard mode is difficult to apply in an electron excited AES system due to restrictions on the application of scanning and retarding potentials to sample, electron gun and analyzer (cf. Fuggle (1981)).

In this chapter we will no longer discuss the electron-beam excited AES and concentrate on x-ray excited AES. Mainly we will use the x-ray excited Auger peaks to study the effective Coulomb interaction for Mn, AgMn and VMn thin films.

As shown in Eq. (2.4-1), the kinetic energy of Auger electrons for a solid depends not only on binding energies of electron levels involved in the Auger process, but also on the Coulomb interaction between the two holes in the final state and the relaxation energy due to the two-hole final state. If we use U_{eff}, the effective Coulomb interaction, to represent these two terms of Coulomb interaction and relaxation energy, then U_{eff} can be directly measured. i.e.

$$U_{eff} = E(A)-E(ABC)-E(B)-E(C) \qquad (6.1-1)$$

where as defined before, E(ABC) is the kinetic energy of Auger electrons for an ABC Auger process and E(A), E(B) and E(C) are the measured binding energies of levels A, B and C respectively. For an atomic-like Auger spectrum, the Auger peak is split due to different final-state terms. In this case, E(ABC) and thus U_{eff} have several different values corresponding to each final term. This has been demonstrated by Antonides *et al.* (1977) for Cu, Zn, Ga and Ge. For a free-electron metal, many-body effects dominate. The term splittings (usually several eV) are comparable to the lifetime broadening of the Auger transitions. As a result, the Auger spectrum shows broad, featureless peaks. In this case, E(ABC) and E(A) *etc.* are measured from the centre of gravity of the corresponding peaks (Fuggle (1981)). Things become difficult for Ni,

Co, Fe, Mn, Cr and V, where the 3d shell is partially filled. The partially filled 3d shell makes the Auger lineshape calculation difficult and the complicated density of states makes the 3d XPS band not well defined. In this case, quantitative analysis is not possible at the present time. Nevertheless, we would like to present our experimental results for the case of Mn in different environments and try to relate the possible differences in U_{eff} with the local magnetic moment.

6.2 Experimental results of $L_3M_{45}M_{45}$ Auger Spectra for Mn, AgMn and VMn thin films on Ru substrate

The same technique used for XPS 3s narrow scans was used for the present Auger studies. Narrow scans with a 50eV or 25eV pass energy were used to record the $2p_{3/2}$ XPS peak, the $L_3M_{45}M_{45}$ Auger peak and the 3d XPS peak for each specimen. We have studied AgMn (~21% at. Mn), ~2 layers Mn on Ru, ~10 layers Mn on Ru and VMn (~25% at. Mn). The results of $L_3M_{45}M_{45}$ Auger spectra for these samples are shown in Fig. 6.2, where the spectra were normalized and vertically shifted for clarity. The binding energy used was 50eV for all these spectra. From Fig. 6.2, it can be seen that these spectra are quite broad and featureless. The peak position as well as the centre of gravity are shifted to the low kinetic energy side as we go from AgMn to ~2 layers Mn on Ru to ~10 layers Mn on Ru to VMn. The centres of gravity for each peak are shown in Fig. 6.2 by heavy crosses. Note that for the AgMn (~21% at. Mn) and VMn (~25% at. Mn) data, the tails of Ag $3p_{1/2}$ and V 2s peaks showed up in the spectra. These Ag and V signals were subtracted (as shown by the dash lines in the diagram) before the centres of gravity were determined. The Auger kinetic energies ($E(L_3M_{45}M_{45})$) measured from the centres of gravity are listed together with other parameters in Table 6.1.

A 25eV pass energy was used for measuring the $2p_{3/2}$ and 3d XPS peaks. Since the Mn $2p_{3/2}$ peak is narrow and well defined, the main peak position was used for measuring $E(L_3)$. It was found that the main peak position of the $2p_{3/2}$ peak did not change much for Mn in different environments. The measured values are listed in Table 6.1. Other experimental data

Fig. 6.2. $L_3M_{45}M_{45}$ Auger spectra for: (1) AgMn (~21% at. Mn), (2) ~2 layers Mn on Ru, (3) ~10 layers Mn on Ru and (4) VMn (~25% at. Mn). The spectra were normalized and vertically shifted for clarity. The binding energy used was 50 eV for (1) to (4). In the diagram, the heavy crosses represent the centres of gravity for each peak and the vertical dash line serves as a guide to the eyes.

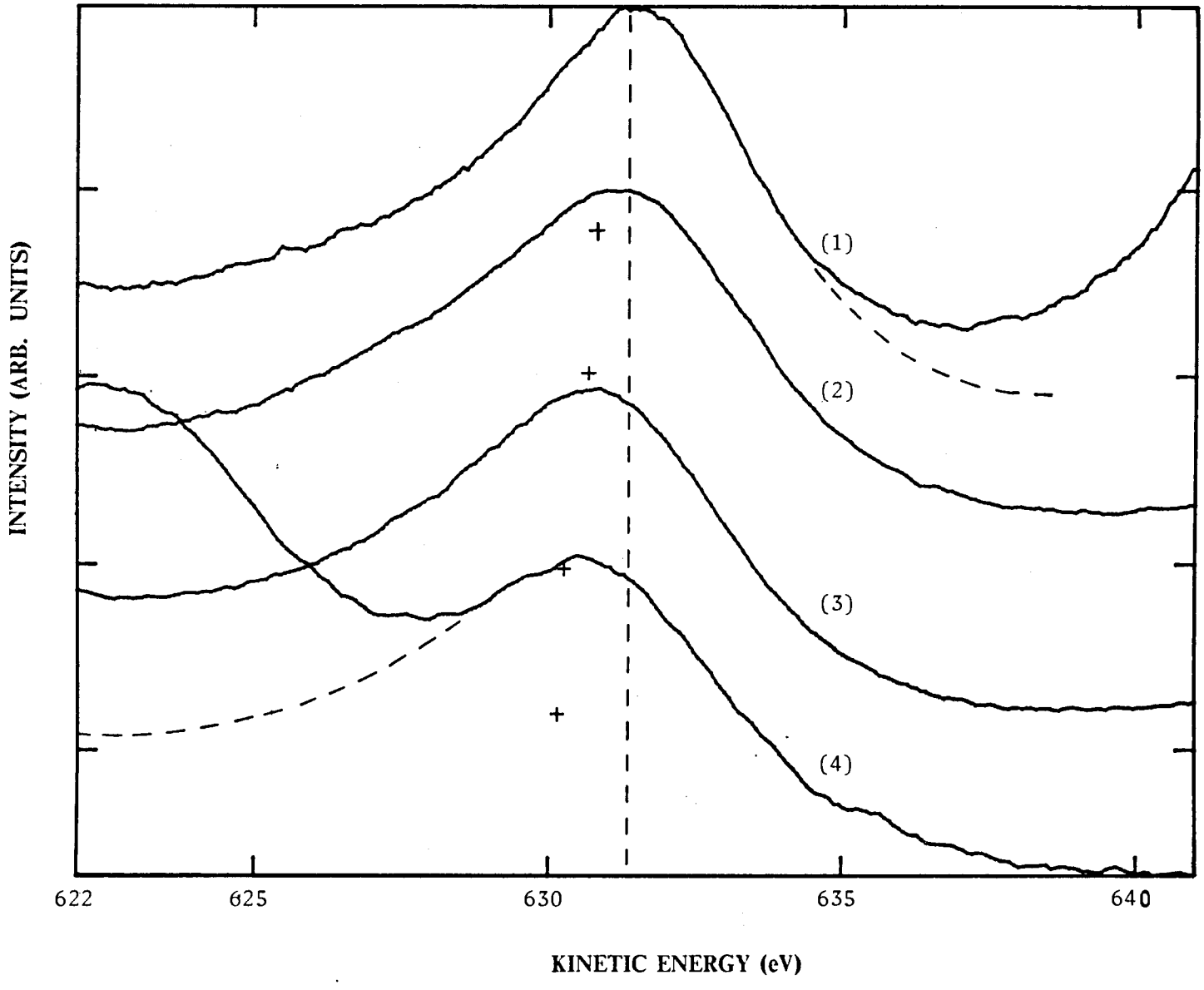
INTENSITY (ARB. UNITS)
(1)
(2)
(3)
(4)
622
625
630
635
640
KINETIC ENERGY (eV)

Samples	AgMn (21%at.Mn)	2 layers Mn on Ru	10 layers Mn on Ru	VMn (25%at.Mn)
$E(L_3)$	638.8±0.1	638.7±0.1	638.7±0.1	638.8±0.1
$E(L_3M_{45}M_{45})$	630.8±0.1	630.7±0.1	630.2±0.1	630.1±0.1
$E(M_{45})$	(3.4±0.1)	(3.4±0.1)	3.4±0.1	(3.4±0.1)
U_{eff}	1.2±0.2	1.2±0.2	1.7±0.2	2.0±0.2

Table 6.1. Experimental values of $E(L_3)$, $E(L_3M_{45}M_{45})$, $E(M_{45})$ and U_{eff} (all in eV) for AgMn (21% at. Mn), 2 layers Mn on Ru, 10 layers Mn on Ru and VMn (25% at. Mn). $E(L_3)$ is the Mn $2p_{3/2}$ binding energy, $E(M_{45})$ is the Mn 3d binding energy, $E(L_3M_{45}M_{45})$ is the kinetic energy of the $L_3M_{45}M_{45}$ Auger electrons and U_{eff} is the effective Coulomb interaction.The $E(M_{45})$ values for AgMn, VMn and 2 layers Mn on Ru samples could not be measured and the estimated value of 3.4±0.1eV was used (see text).

showed also that the Mn $2p_{3/2}$ peak position does not change much. For instance, the Mn on Ru with different thicknesses, the VMn with different concentrations, the Mn on Fe and the Mn on $NbSe_2$ all have their Mn $2p_{3/2}$ peaks located at around 638.7±0.1eV. The AgMn alloy with low Mn concentration is an exception, where the Mn $2p_{3/2}$ peak has a totally different lineshape (cf. Section 5.3 and Fig. 5.5). An additional broad peak (call it peak 2) showed up on the higher binding energy side about 4 eV away from the old $2p_{3/2}$ peak (called it peak 1). For the present sample (AgMn (~21% at. Mn)), it was measured that $E_1(L_3)=638.8\pm0.1$ eV and $E_2(L_3)=642.8\pm0.1$ eV, where E_1 and E_2 stand for the positions of peak 1 and peak 2 respectively. The physical origin of peak 2 is not clear. For the present study, we will use $E_1(L_3)$ for the Mn $2p_{3/2}$ binding energy.

Analysis becomes more difficult for the Mn 3d peak though not too bad for the ~10 layers Mn on Ru sample. For this sample we could still obtain a clear Mn 3d spectrum. Such a spectrum is shown in Fig. 6.3. The energy scale is expressed in kinetic energy. The Fermi level is indicated by the dash line, which was determined by the calibration process (cf. Appendix C). The signal was weak when a 25eV pass energy was used and eight scans were accumulated by using the Nicolet signal averager to obtain the spectrum shown in Fig. 6.3. The 3d bandwidth measured as a FWHM is about 5eV and $E(M_{45})$ measured from the centre of gravity to the Fermi level is 3.4±0.1 eV. Considering the instrumental broadening, the actual 3d bandwidth W should be considerablly smaller. According to our XPS measurements for Ag $3d_{5/2}$ peak (which is very narrow) using 15 eV, 25 eV, 50 eV and 100 eV pass energies, the FWHM's are 0.9 eV, 1.2 eV, 1.7 eV and 2.4 eV respectively. Thus a FWHM of 5 eV measured at 25 eV pass energy should correspond to a real FWHM of 3.5 eV or less. Due to the complicated density of states for the partially filled 3d shell, the 3d bandwidth is not well defined. Thus we simply take W to be 3.5 eV, which is the same value that Kostroun *et al.* (1971) measured for Fe. This estimation should not affect our qualitative analysis.

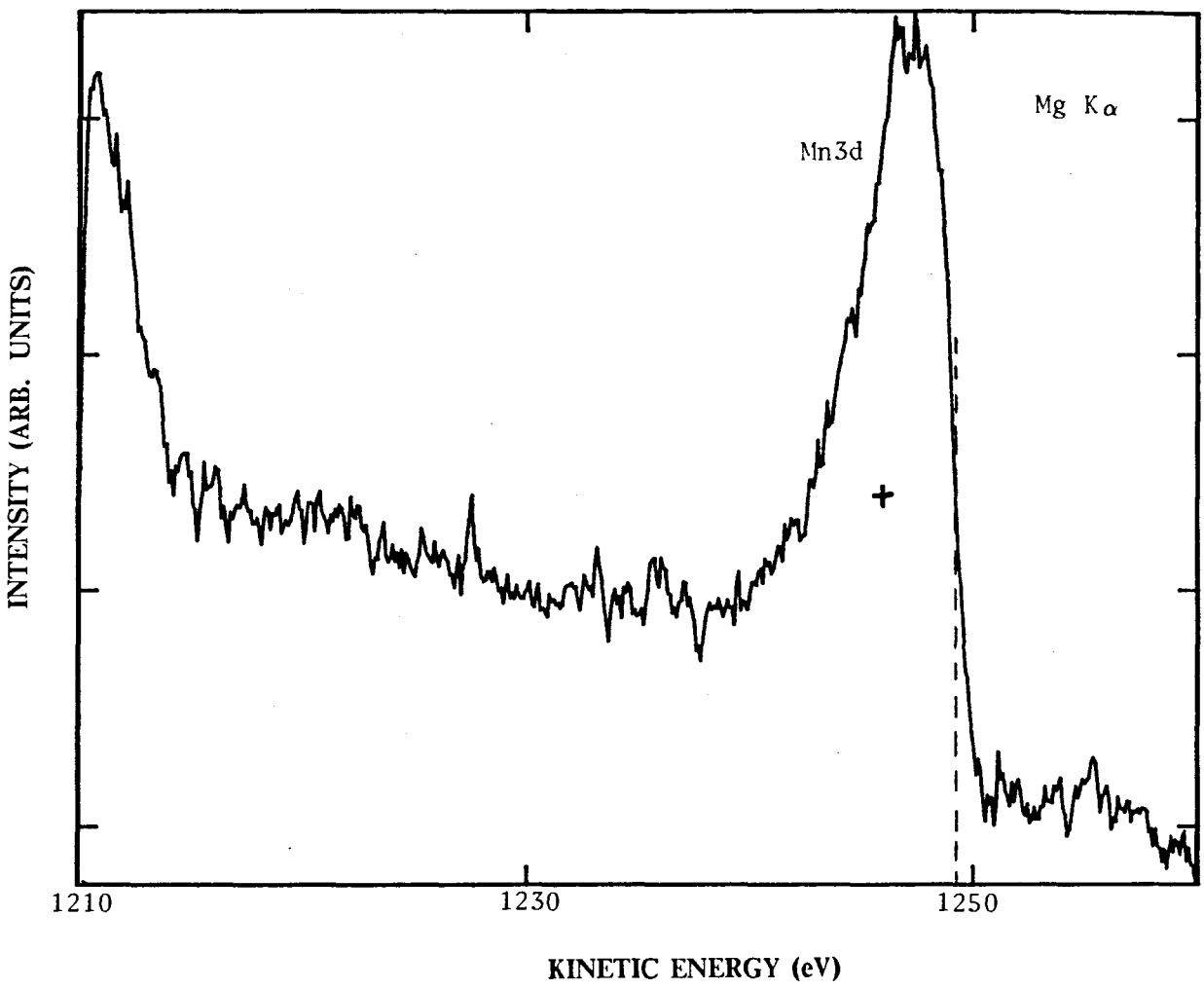

Fig. 6.3. Mn 3d spectrum obtained from an XPS narrow scan for an ~10 layers Mn on Ru sample. The dash line shows the location of the Fermi level. The heavy cross indicates the centre of gravity of the 3d peak. The pass energy used was 25 eV. The dashed line serves as a guide to the eye.

For the ~2 layers Mn on Ru sample, the Mn 3d peak was severely interfered with by the Ru 4d signal. For the AgMn (~21% at. Mn) and VMn (~25% at. Mn) samples, we could not distingush the Mn 3d signal from the Ag 4d or V 3d signal either. Thus we could not measure accurately the Mn 3d peak in these cases. But from the appearance of the spectra of these samples (not shown) we believe that both the bandwidth and the value of $E(M_{45})$ are not far from that of the ~10 layers Mn on Ru sample. In later analysis, we will assume that the Mn 3d bandwidth is about 3.5eV and $E(M_{45})$ is about 3.4eV for all these samples.

Using Eq. (6.1-1), the effective Coulomb interactions were easily calculated from the above measurements. The results are summarized in Table 6.1. It can be seen from the table that U_{eff} increases from AgMn and ~2 layers Mn on Ru to ~10 layers Mn on Ru to VMn. These values are compared to the values obtained by Antonides *et al.* (1977) for Fe (~1.1 eV) and Co (~1.2 eV).

6.3 Discussions

Sawatzky (1977) has pointed out that the measured effective Coulomb interaction U_{eff} is closely related to the well known Hubbard U. Within the model of one-electron theory Hubbard (1963, 1964) investigated the effects of electron correlation and proposed a positive energy U (times the number of doubly occupied ionic levels) to represent the Coulomb interaction. His idea is based on van Vleck's model of quantum fluctuations, which we have introduced in Section 5.4.1. In his calculation, the atom is considered to be an "average configuration" and U is defined as the sum of the energy required to transfer an electron from the Fermi level to that atom and the energy required to move an electron from such an atom to the Fermi level. The interaction between these two electrons is restricted to a single ionic site. This restriction is somewhat justified considering the screening effects due to the itinerant nature of valence electrons in a metal. This simplification makes calculations easier and Hubbard found that for large correlation the electronic band is split into two subbands separated by U. He found also that in the limit of

negligible intrasite repulsion (U << W, where W is the one-electron bandwidth) one has an ordinary metallic band. In the opposite limit (U >>W), the electrons seemly are localized on a single atom.

Sawatzky and Lenselink (1980) have calculated the Auger spectrum for an initially filled simple-cubic tight-binding s band and found that the Auger line shape is strongly dependent on U_{eff}, the effective Coulomb interaction between the two holes in the final state. For various values of U_{eff}/W, the obtained spectra show both the band states and bound states with the trend predicted by Hubbard, i.e., the bound states (represented by an intense narrow atomiclike peak) dominate when $U_{eff} >> W$ and the band states (represented by a broad bandlike peak) dominate when $U_{eff} << W$. This has been confirmed by their experimental observations (Antonides *et al.* (1977)). Thus U_{eff} is closely related to the Hubbard U (despite the fact that by definition U_{eff} is not quite the Hubbard U).

For our case of Mn, it can be seen from Fig. 6.2 that the Auger spectra are bandlike for Mn in all cases we studied. The measured U_{eff}'s are much smaller than the one-electron 3d bandwidth W (~3.5 eV). We can thus conclude that the correlation is small in the case of Mn. Considering the values of U_{eff} for Fe (~1.1 eV) and Co (~1.2 eV), we see also that Mn is similar to Fe and Co. This is compared with the case of Ni. For Ni, U_{eff} (~4.1 eV) is larger than W (~2.6 eV according to Kostroun *et al.* (1971) or ~3.0 eV according to Antonides *et al.* (1977)). Obviously Ni has larger correlation between 3d electrons compared with Mn, Fe and Co. This larger correlation (i.e. the electrons are more localized) in the partially filled 3d shell might be the reason why Ni has a large two-channel screening splitting (cf. Section 5.3). For Mn, Fe and Co, the U_{eff} is quite small and electrons are more free electron like. As a result, the two-channel screening effect is much smaller. We are thus convinced that the ~4 eV splitting observed in various forms of Mn is the exchange splitting and not the two-channel screening splitting. That is to say that the splitting is related to the 3d spin polarization.

It is of interest to note that the values of U_{eff} we measured for Mn in different environments are slightly different from each other (cf. Table 6.1). Although there is a large uncertainty (~±0.2 eV) in the measured values due to the difficulty in measuring $E(M_{45})$, the results show clearly that U_{eff} increases as we go from AgMn and 2 layers Mn on Ru to 10 layers Mn on Ru to VMn. This is the same trend we observed in their 3s XPS satellite intensities (cf. Fig. 5.6a). We do not know if there is any correlation between U_{eff} and the magnetic moment, but it is interesting enough to note that U_{eff} goes rapidly down from Cu (~8.0 eV) to Ni (~4.1 eV) to Co (~1.2 eV) to Fe (~1.1 eV), (cf. Antonides *et al.* (1977)). At least, the results we obtained for U_{eff} are in the direction we would expect. This discovery together with a more detailed study of U_{eff} and Auger spectra for Ti through Ni would increase our understanding of magnetism and magnetic moments in 3d transition metals.

CHAPTER 7

SUMMARY AND CONCLUSIONS

The structure and magnetic properties of Mn ultrathin films grown by molecular beam epitaxy have been carefully studied by using RHEED, EELFS, XPS and AES techniques. AgMn and VMn binary alloys have also been grown and studied for comparison.

Mn can be grown on a Ru(001) substrate epitaxially layer-by-layer. An expanded structure with the same lattice constant as that of Ru has been found for the first two Mn overlayers. A trimerized structure was proposed to explain the observed 3x1 RHEED pattern which developed after the formation of the third Mn overlayer. The nearest neighbor distance between Mn atoms in this model (~2.39Å) has been confirmed by the EELFS analysis.

The layer-by-layer growth of Mn on Ru was revealed by AES and XPS, which showed good exponential behavior in the AES (XPS) intensity vs. deposition time measurements. From these measurements it was also found that the electron inelastic mean free path is 5.8±0.5Å for the Ru 231eV Auger signal and 12.7±0.5Å for the Mn 589eV Auger signal. RHEED also showed evidence of layer-by-layer growth for Mn on Ru. We are convinced that for a layer-by-layer growth, RHEED shows only the diffraction pattern of the top surface layer. The method of using a layer-compound substrate (e.g. $NbSe_2$) and RHEED to determine the growth rate is unique and would be useful in MBE work.

Calculations using the van der Merwe model showed good agreement between the calculated critical thickness and the experimental observations for Mn on Ru. The information about the mismatch and adsorption energies of the substrate and the overlayer can thus give us some guidance when we grow other materials or use other substrates.

Our XPS studies showed that the splitting observed in the Mn XPS 3s peak is due to the exchange interaction. The two-channel screening effects are small in case of Mn. However, the observed energy splitting and the intensity ratio of the main peak to the satellite peak for Mn in different environments differ from what one would expect from the simple one-electron van Vleck theory of the exchange splitting. Although quantitative agreement could not be obtained, qualitatively both the energy splitting and the intensity ratio are in the direction predicted by the theory of exchange splitting.

The expanded Mn atoms are found to have larger magnetic moment compared with the trimerized Mn atoms. This conclusion about the 3d spin polarization was mainly obtained from the relative intensity of the 3s satellite peak. Although the energy splitting reflects some information about the 3s spin polarization, in general it is not sensitive in the case of metals. Similar 3s measurements performed for Mn in different environments and for the 3d transition elements Ti through Cu have shown clearly that the larger the local magnetic moment, the stronger the satellite peak and the larger the energy splitting (although the difference in energy splitting is small). This observation is correlated with the thermodynamic measurements of susceptibility and specific heat. We believe that the final states in a photoemission process involve high spin and low spin 3d shells. The high spin 3d shell obeys Hund's rule and the low spin 3d shell has randomly averaged spins. It is suggested that the quantum fluctuation between the high and the low spin states for Mn in VMn are slower than 10^{-15}s, the time scale for XPS measurements, and faster than 10^{-13}s, the time scale for thermodynamic measurements. The 3s satellite peak represents the exchange splitting due to the high spin states and its intensity represents the probability of the high spin states. The low spin states contribute only to the main peak. These ideas account for the experimental facts that the energy splitting is not sensitive to the magnetic moment and that the intensity ratio of the main peak to the satellite peak is always higher than the theoretic value.

The observed Mn 3s satellite peaks for Mn in different environments were compared with the relative Mn atomic sizes. This was also compared with the correlation of the relative atomic size and the relative intensity of the 3s satellite peak for the 3d transition metals. It is concluded that the magnetic moment of Mn atoms increases as the atomic size increases.

The Doniach-Sunjic theory of XPS lineshape has been successfully used to fit our spectra. The fitting paramenters give us a more quantitative idea about the energy splittings and intensity ratios. The Doniach-Sunjic lineshape fittings were especially used to test Veal and Paulikas' idea about the two-channel screening mechanism for Ni and the trimerized and the expanded Mn. The fittings have shown that for Ni the XPS splitting is mainly due to the two-channel screening effect and for Mn the 3s splitting is mainly determined by the exchange splitting.

The AES analysis of Mn $L_3M_{45}M_{45}$ peak shows also that the effective Coulomb interaction U_{eff} is much smaller for Mn than that for Ni. This means that for Mn the 3d electrons are more free electron like and the two-channel screening effect is much weaker in Mn than in Ni. The observed U_{eff} for Mn in different environments showed the same trend we observed in the 3s XPS satellite intensities. It is suggested that there might be some correlation between U_{eff} and the magnetic moment.

In summary, the present study of Mn, AgMn and VMn thin films shows that by changing the Mn environment we can change the magnetic properties of Mn atoms. Especially, by expanding the Mn lattice we can have a larger magnetic moment for Mn atoms. Further studies along this direction and searching for ways to enhance the interatomic exchange for ferromagnetism could lead eventually to better magnetic materials.

APPENDIX A : VACUUM SYSTEM

Cryogenic refrigeration pumping system

The cryogenic refrigeration pumping system (or simply, cryopump) is based on cryoadsorbing. It consists of a Displex Model CSW-202 water cooled two-stage refrigerator and a HV-202 cryopump. The refrigerator is a closed-circle cryogenic refrigeration system employing helium as a working medium. The cryopump consists of a pump enclosure and cryopanels. It uses the refrigerator as a cryogenic source.

The refrigerator consists of an expander, a compressor and a set of flexible interconnecting lines serves to supply and to return helium gas between the expander and compressor. This configuration allows easy installation of the expander together with the cryopump into the UHV system, leaving the relative heavy compressor away from the system. The refrigeration occurs in the expander where the helium gas is expanded. The whole refrigeration process is circulated in the so-called Solvay cycle which is first described by E. Solvay in 1886. The Solvay cycle in the expander accomplished by an orifice surge volume combination, a first-stage displacer, a second-stage displacer and a dual-ported rotary valve disc. The refrigerator is able to provide a temperature as low as 14K. The compressor compresses the depressurized helium gas from the expander and provides high pressure helium gas back to the expander. It is a converted, oil lubricated air conditioner type of Freon compressor. The heat captured by the oil and the helium is removed by cooling water. A glass wool packed column is used to agglomerate and separate the oil from the helium. A adsorber packed with charcoal and molecular sieve is used to trap residual oil vapor and water, which is desorbed from materials within the system.

By using the refrigerator as a cryogenic source and mounting the cryopanels to the vacuum chamber, the cryopump is able to adsorb all kinds of gases except helium.

The accumulated cryodeposits can be removed by warming up the cryopump to room temperature and using a roughing pump (we use a turbopump) to pump out the released gases.

Boostivac ion pump

An ion pump usually contains a magnet, a cylindrical-cell anode and two metal (tantalum in our system) cathode plates, as shown in Fig. A.1. A high electric voltage (about 5000 to 7000V) is applied between the anode and the cathode. Electrons emitted from the cathode are forced by the strong magnetic field into a spiral path towards the anode with high speeds. Gases in the ion pump are ionized by the collision with electrons. The positive ions then bombard the metal cathode and sputter metal atoms away from the cathode. These metal atoms are easily reacted with various chemically active gas molecules and form stable solid compounds resulting a high vacuum. The pumping speed of an ion pump is relatively low, so that it is not desirable to use an ion pump for heavy loads.

To increase the pumping rate of an ion pump at poor vacuum, a titanium evaporation unit is normally added. This unit together with the ion pump form a boostivac pumping system. Gases such as H_2, O_2, N_2 and CO_2 can be chemically combined with titanium. By frequently supplying titanium , the Boostivac system is able to getter a relatively large amount of these gatherable gases and thus permanently remove them. Titanium is supplied from a current-heated Ti filament to a substrate plate. The sublimation of Ti should be matched to the gas load, i.e., more sublimation is needed for a heavy load and less sublimation for a light load. In UHV operation, a sublimation period of only two minutes in 24 hours is sufficient.

The deposited Ti film can pump the gatherable gases quite rapidly, but other gases must be pumped away by other means. The ion pump can pump all kinds of gases, but does not have the capacity of rapid pumping. A combination of a Boostivac unit and an ion pump is thus desirable. For example, gases such as H_2O can be ionized by the ion pump and then rapidly

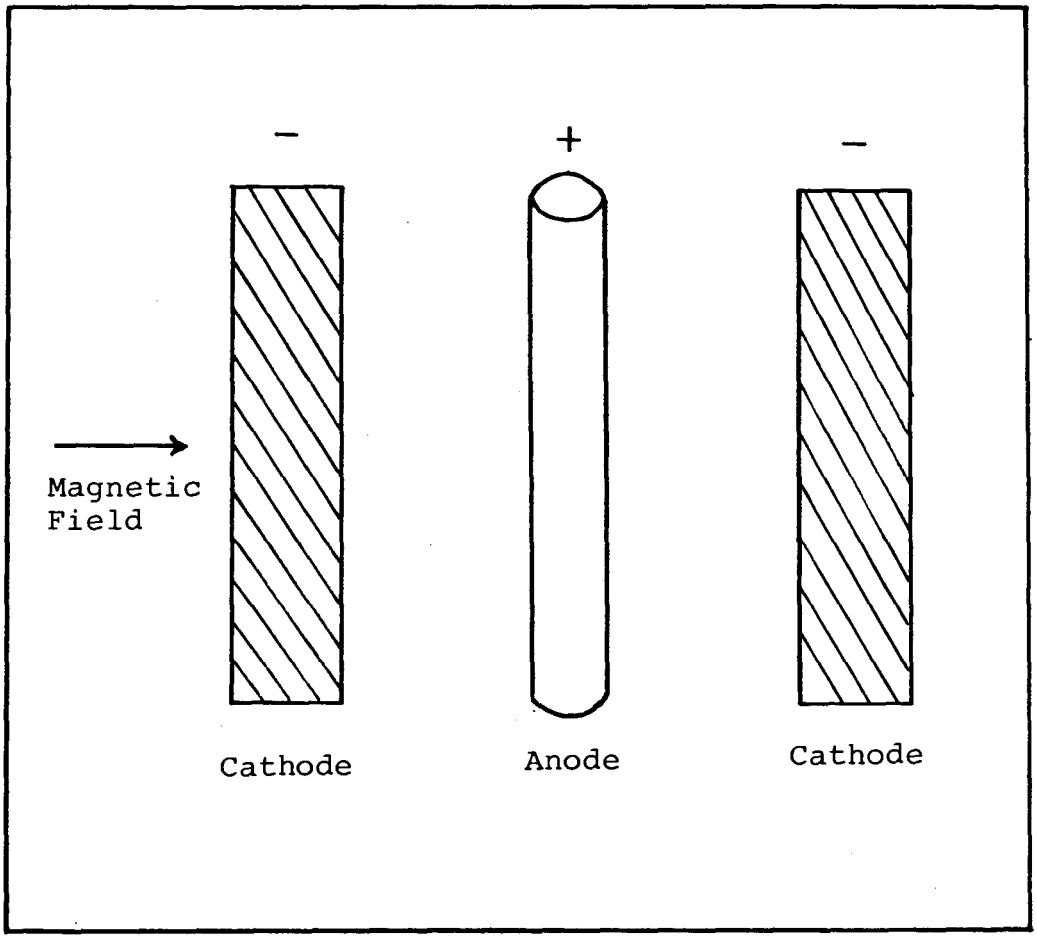

Fig. A.1. A schematic diagram of an ion pump, which shows a cylindrical-cell anode and two metal cathode plates in a magnetic field.

pumped by the Ti film. This ionization and gathering process is suitable for most residual gases and is mostly useful during the bakeout.

Cryosorption Pump

Whenever the analysis chamber or growth chamber is back filled with dry nitrogen, which is needed in opening the UHV system, a large amount of gases is involved. In this case cryosorption pumps are ideal for rough pumping because of their ability of rapid sucking out large amounts of gases. Furthermore, they are completely oil free.

The body of a sorption pump consists simply of a metallic container, which is filled of absorbents such as 5A molecular sieve and processed oxides of Al and Si. When the previously outgassed absorbent is cooled to liquid nitrogen temperature, it is an effective getter due to the enormous surface area of absorption. Outgassing a sorption pump is accomplished by baking out the pump at about 300C for 1–2 hours. By using two sorption pumps in sequence, we could pump our system from atmosphere to low millitorr region.

Turbo–molecular Pump

A very powerful mechanical type of pump is the turbomolecular pump. It consists of well designed rotor blades rotated by a high speed motor. The motor is overhung–mounted and runs in two high–precision ball bearings which are supplied with oil by wick lubrication. When gas molecules from the high vacuum port of the system hit the fast rotating blades, they receive an additional velocity component in the direction of the blade. When the circumferential speed of the rotor blades is of the order of the mean molecular velocity of the gas molecules, the appropriate design ensures the gas molecules be sweeped into the fore vacuum side. A schematic diagram of the turbopump is shown in Fig. A.2. The turbopump operates in the molecular flow

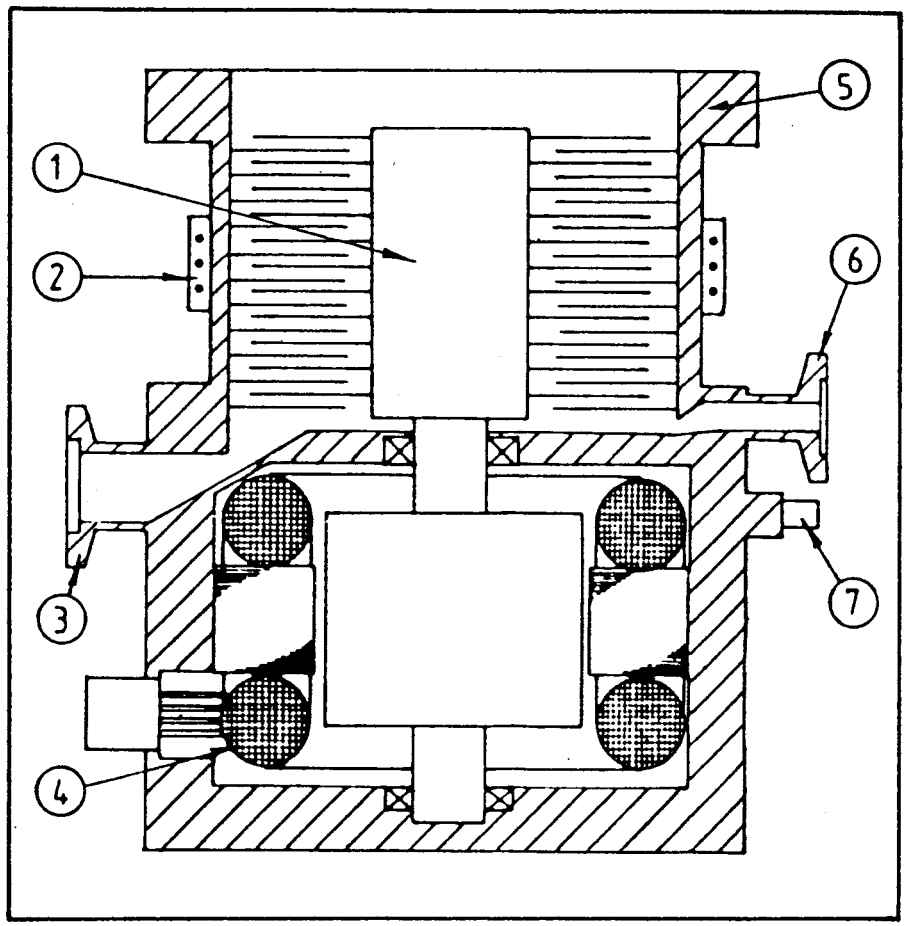

Fig. A.2. A schematic diagram of a turbopump. The parts are represented by: (1) rotor, (2) heater, (3) roughing vacuum, (4) motor, (5) UHV connection, (6) venting connection, (7) cooling water connection.

region where the geometrical dimensions of the blades are smaller than the mean free path of the gas molecules. As a result it is very efficient for pumping heavy molecules. A good turbopump can pump a vacuum system from atomosphere pressure down to very low pressure. The turbopump we used (TPH110, ARTHUR PFEIFFER Corporation, Germany) can reach a high vacuum of $4x10^{-8}$ Torr. So that it is conveniently used in the MBE system to pump the introduction chamber. A main disadvantage of turbopumps is the possible hydrocarbon backstreaming from the lubricant oil to the UHV system. Selecting high quality special oil is very important. It is believed that the hydrocarbon backstreaming can not be totally avoid and it is recommanded not to use a turbopump to pump the MBE growth chamber directly.

Due to the very high speed of the rotating blades (about 40,000 rpm), any foreign matter such as a peice of broken wire, broken ceramics etc. will be a disaster to the pump. A splinter shield may be used in the cost of decreasing the flow rate of the pump by about 15%.

Measurement of UHV---the Ionization Gauge

The ionization gauge is widely used to measure ultrahigh vacuum. The so-called Bayard Alpert ionization gauge has an inverted triode configuration with the filament external to a cylindrical wire grid and a fine wire collector in the axis of the grid, as shown in Fig. A.3. Electrons emitted from the filament oscillate between the filament and the collector through the wire grid and ionize residual gas molecules. The electrons eventually captured by the wire grid form the grid current I_g which indicates the value of filament emission. The positive ions arrive at the collector forming the resultant current I_c. I_c is proportional to pressure P and I_g, i.e., $I_c = SPI_g$. The proportional coefficient S is called the gauge sensitivity and depends on temperature, gas species, electron energy and gauge geometry. S can be obtained through a calibration procedure. P can then be determined by measuring I_c and I_g. Since S depends on the composition of the residual gas, the ionization gauge is not an absolute gauge and its

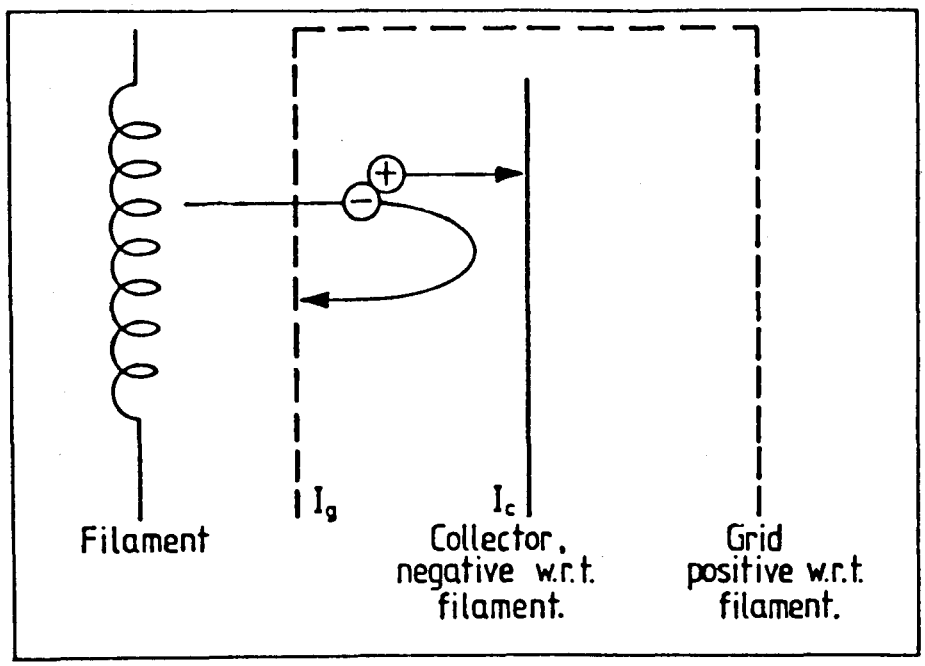

Fig. A.3. The configuration of an ionization gauge. The relative potential polarities of the collector and grid with respect to the filament are indicated. The motions of electrons and ionised residual gas molecules are also shown.

indicated pressure may show a total pressure correct within the range +100% to -50%.

In the UHV range (the low 10^{-11} torr), the ionization gauge is affected by the x-ray limit. When electrons strike directly the grid, x-rays may be emitted. If the emitted x-rays strike the collector, they may eject photoelectrons. The ejection of photoelectron is equivelent to the collection of positive ions, leading a so-called "x-ray pressure", which has nothing to do with the residual gas pressure. The x-ray pressure thus sets a lower limit to the ionization gauge. So that in the very high vacuum case, the true pressure should be obtained by subtracting the x-ray pressure from the indicated one.

The x-ray pressure differs for different ionization gauges due to its dependence on the surrounding geometry. It can be determined fairy easily by using the electron energy method. This method is based on the fact that the x-ray pressure is proportional to the grid voltage and independent of residual gas pressure. With the gauge at a constant pressure in the range of the x-ray limit, increase grid voltage and plot the indicated pressure as a function of electron energy (i.e., grid voltage minus filament voltage) in a log-log scale. The x-ray pressure can then be obtained by extrapolating the linear part of the graph back to the normal operating grid potential. Such a graph is shown in Fig. A.4. The normal operating grid potential is 175V and the filament potential is 45V.

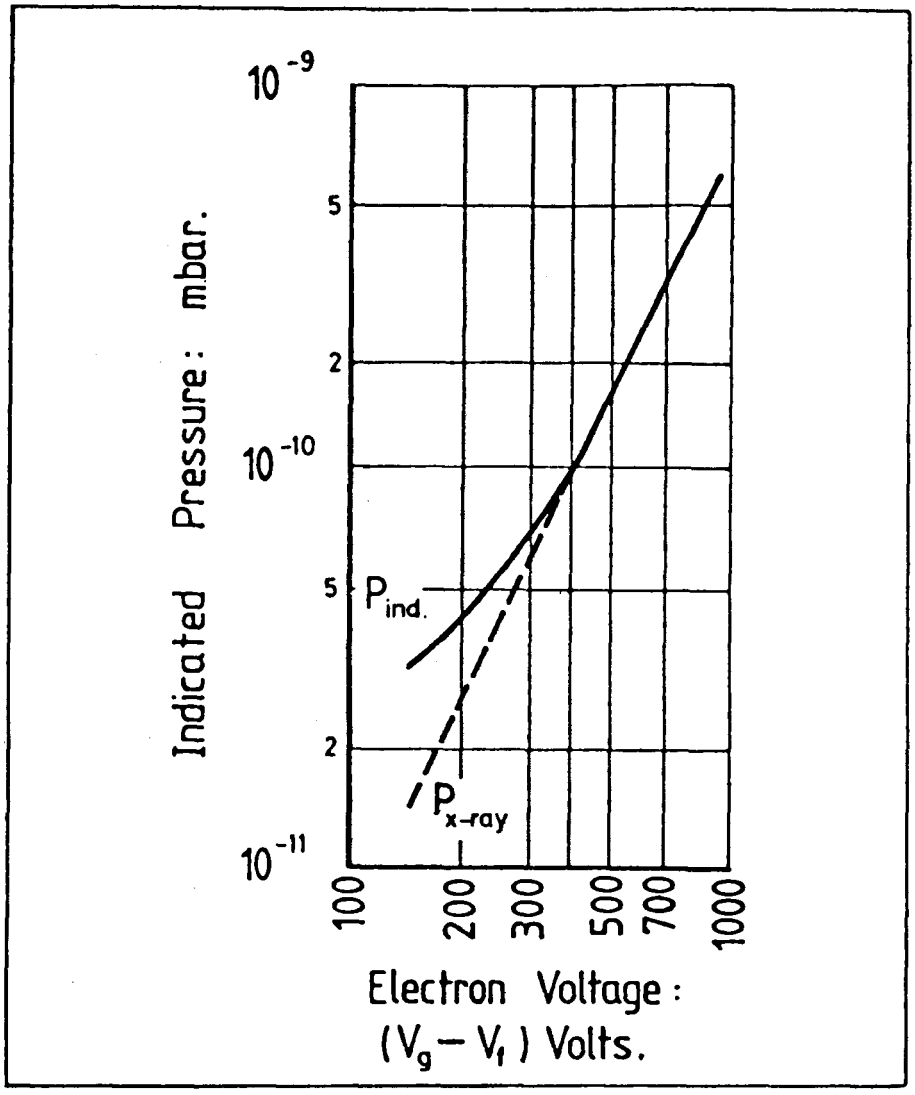

Fig. A.4. A graph showing the electron energy method used to determine the x-ray limit in an ionization gauge, which plots the indicated pressure (read directly from the panel meter) as a function of electron energy.

APPENDIX B : UTI QUADRUPOLE MASS ANALYZER

A UTI quadrupole mass analyzer consists of three components, namely, the ionizer, the quadrupole mass filter and the ion detector (electron multiplier). A schematic diagram is shown in Fig. B.1.

The ionizer consists of the filaments, the grid, the reflector and the focus plate. The thermionically emitted electrons from the dual hot filaments are accelerated toward the grid, which is at positive potential with respect to the filaments and ground. Those electrons which do not strike the grid wire or do not ionize any substance will keep circulating between the filaments and the reflector, which are at negative potential, until they are collected by the grid or lost by recapture to surrounding grounded surfaces. When gas atoms or molecules enter into the ionizer, they are bombarded by electrons and become positively charged ions. These charged ions are then injected into the quadrupole mass filter through the focus plate which is kept at a negative potential.

The quadrupole mass filter consists of four precisely machined molybdenum rods which are accurately aligned and attached to alumina insulators. Those two pairs of molybdenum rods are supplied by both radio–frequency and d.c. voltages and construct a quadrupole configuration, leading to a combined RF and electrostatic field around them. For certain applied voltages, the charged ions with a specific mass–to–charge ratio will have a dynamically stable trajectory within the field and can go through the filter section and enter into the ion detector. All other ions will be filtered out. By continuously varying the applied voltages, a range of substances can be sequentially stabilized and thus traverse the filter. The RF voltage sweeps continuously from about zero to 2400V (rms) in sweeping the entire mass range. It is controled by the scan circuit. The radio frenquency is nominally 2 MHz. The d.c. voltages applied to the molybdenum rods are supplied by the rod driver circuit in some fixed ratio referred to the RF voltage. The location and spacing of the mass spectrum peaks is determined by the RF voltage, whereas the

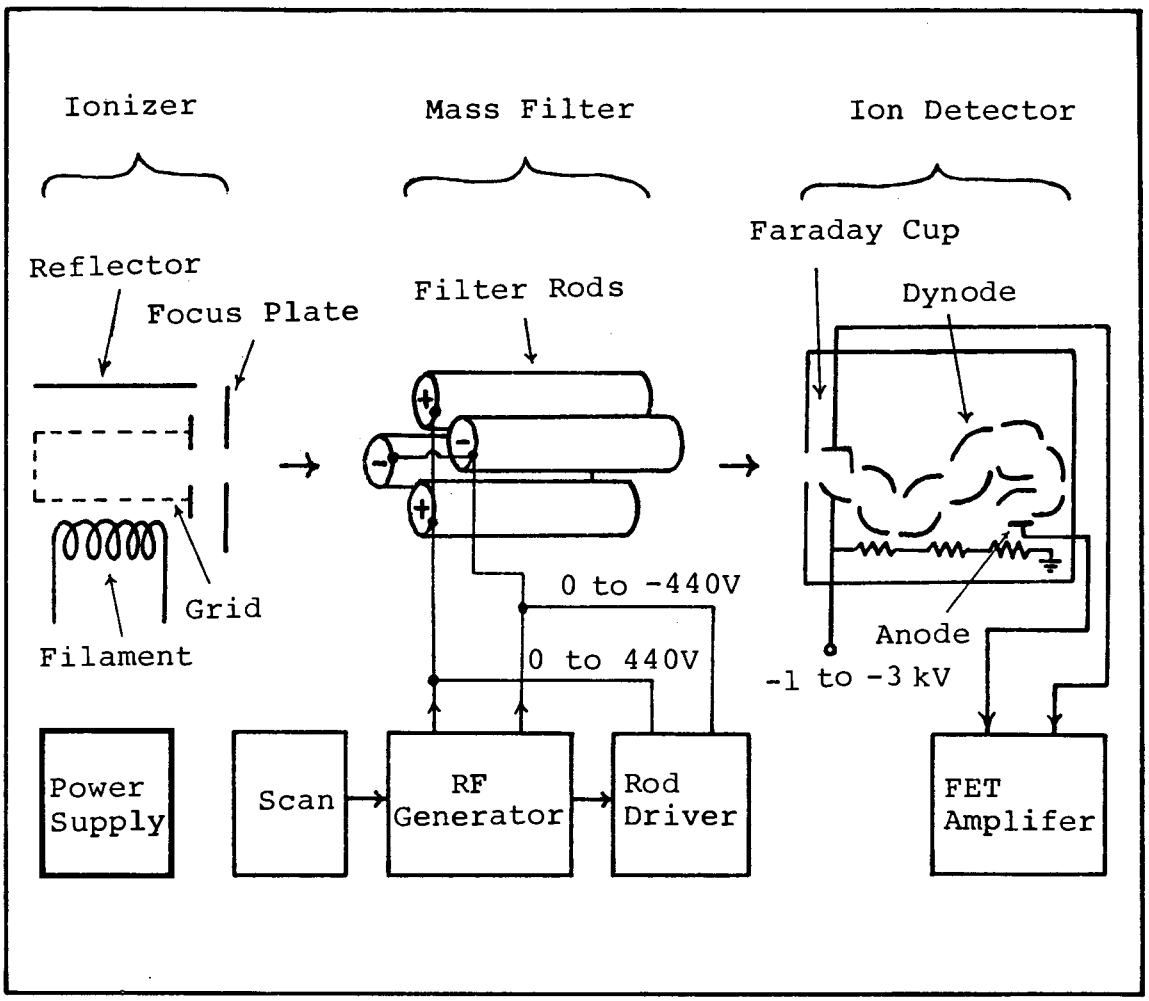

Fig. B.1. A schematical representation of a quadrupole mass analyzer, which shows the configuration of the ionizer, mass filter and ion detector.

DC/RF voltage ratio determines the spectrum resolution.

The ion detector is a 16-stage electron multiplier which amplifies the single charge of the arriving ion into a current. Each stage of the electron multipier is a Cu/Be oxygen activated dynode. The potential difference between each stage ranges from approximately 60 to 200V. The total charge multiplication is on the order of 10^4 to 10^6 depending on the age and working conditions of the multiplier. As an integral part of the ion detector, there is a Faraday cup which can be used to read ion currents emerged directly from the filter. The Faraday cup can thus be used to calibrate the gain of the multiplier. The current from the anode of the multiplier or from the Faraday cup is amplified by a FET amplifier. The output of the FET amplifier is referenced against the scan voltage, which determines the stable trajectory of the charged ions, thereby producing a spectrum with peaks corresponding to different ions. Since the charged ions have discrete masses and discrete charges (usually a single charge), discrete peaks are usually observed.

The UTI quadrupole mass analyzer can also be used for quantitative measurements. In the zeroth-order approximation, the measurements are carried out by comparing the ion currents from UTI directly. For instance, the percentage composition of element J can be calculated from

$$100\frac{\Sigma I^+_j}{\Sigma I^+_i} = 100\frac{I^+_J}{I^+_I}$$

where $I^+_J = \Sigma I^+_j$ (from j=1 to j=m) is the total ion current for substance j which has m isotropes and $I^+_I = \Sigma I^+_i$ (from i=1 to i=n) is the total ion current for all substances. The partial pressure P_J is then $P_J = P_T I^+_J / I^+_I$, where P_T is the "Total Press" reading on the UTI panel.

For more accurate measurement we should consider some corrections. Usually we should consider: the ionization efficiency $\epsilon(J)$, the electron multiplier gain G and the quadrupole transmission T. $\epsilon(J)$ is a function of the cross-section for electron removal. It is an indication of

the ease of bond-breaking. Usually nitrogen is used as a reference, i.e., $\epsilon(N_2)=1$. The multiplier gain G is a function of the ion mass m (AMU) and has an $m^{-1/2}$ dependence, i.e., the heavier the substance the smaller the gain. T is the efficiency of ion transmission through the quadrupole filter. For substances with a mass (AMU) from 1 to 40, T is very close to 100%. Care should be taken that T may be influenced by the ion energy, the focusing, and resolution setings *etc.* Considering all these three factors, the total corrected ion current for substance j can be expressed as

$$I^+ = \frac{1}{\epsilon_J} \Sigma \frac{I^+_{EM,\,j}}{G_i\, T_j} \quad ,$$

where $I^+_{EM,\,j}$ is the measured ion current from the electron multiplier for substance j. Using this expression we can easily calculate the relative sensitivity of certain substances. For example, we have calculated the relative sensitivity of Ag_{107} line with respect to Mn line. By checking out that $I(Ag_{107}) / I(Ag) = 54\%$, $\epsilon(Ag)=2.45$, $\epsilon(Mn)=1.65$, $G(Ag)=0.51$, $G(Mn)=0.71$, $T(Ag)=0.31$ and $T(Mn)=0.7$, we found that the actual vapor ratio of Ag/Mn is about four times less than that shown by the measured Ag_{107} and Mn line intensities.

From I^+_J one can obtain the corrected partial pressure of substance J from the following expression:

$$P_J = \frac{I^+_J}{S_B(N_2)} = \frac{1}{\epsilon_J S_B\,(N_2)} \Sigma \frac{I^+_{EM,\,j}}{G_j T_j} \quad ,$$

where $S_B(N_2)$ is the basic sensitivity for nitrogen which can be obtained from

$$S_B(N_2) = I^+_{Fc,N_2} / P_T$$

and I^+_{Fc,N_2} is the Faraday cup ion current when a known nitrogen pressure is present.

APPENDIX C : XPS---X-RAY PHOTOELECTRON SPECTROSCOPY

Instrument and experimental considerations

The basic components consist of an x-ray source, an electron energy analyser and detector, and some controlling electronics. The x-ray source which we used (PHI Model-548) consists of a heated filament cathode and two water-cooled anodes (one Al anode and one Mg anode lying side by side, only one anode is used in each measurement). An Al foil about 20μm thick (which is transparent to x-rays) is used as a window in front of the x-ray gun to separate the excitation region from the specimen. Within a maximum power of 400W the potential between the cathode and the anode can be adjusted up to 20kV (usually 15kV and 20mA were used). The accelerated hot electrons bombard on the anode and create holes in the inner levels of the anode atoms. The transitions of electrons from higher levels of the anode atoms into these holes result the radiation of x-rays. The low-z(atomic number) anodes used make it posible that the dominant transitions are of the type $2p_{3/2}$ to 1s and $2p_{1/2}$ to 1s, leading to a very intense, unresolved $K\alpha_{1,2}$ x-ray beam. The main x-rays produced in our x-ray source are 1253.6eV Mg$K\alpha_{1,2}$ x-ray with a FWHM (the Full Width at Half Maximum) of 0.7eV and 1486.6eV Al$K\alpha_{1,2}$ with a FWHM of 0.8eV. In addition of $K\alpha_{1,2}$ x-rays, there are also satellites arising from 2p to 1s transitions in atoms which are doubly-ionized or triply-ionized, *etc.* Among them,the $K\alpha_{3,4}$, which are generated from 2p to 1s transitions in doubly-ionized atoms (i.e., those atoms have initial holes in both 1s and 2s or 2p levels), are mostly significant. They appear at about 10eV above the $K\alpha_{1,2}$ peak in Mg and Al and have intensities of about 8% of that of the $K\alpha_{1,2}$ for Mg and 4% for Al (Krause and Ferreira (1975)). The other satellites are very weak (<1% of the $K\alpha_{1,2}$ intensity) and can be ignored. An additional band of K_β x-rays (about 45-50eV above the $K\alpha_{1,2}$line) arising from valence band to 1s transitions is also very small (about 1% of the $K\alpha_{1,2}$ intensity) and can be ignored in most cases.

Mg and Al are generally utilized as anode materials mainly due to their low vapor pressure and low chemical reactivity as well as the relatively narrow linewidth of their $K\alpha_{1,2}$ lines. In cases where higher energy resolution is needed, monochromatized Al $K\alpha$ excitation should be used. Photoelectron peaks as narrow as 0.4eV can be obtained by using monochromatization (Siegbahn *et al.* (1972)). While without using monochromatization, these peaks are as wide as 0.9eV. The monochromatization is usually realized by Bragg reflection from a suitable single crystal such as Si. The intensity loss thus introduced has to be compensated by other techniques (Siegbahn *et al.* (1972), Siegbahn (1974)).

Since we cannot focus x-ray beam, the spatial resolution of XPS is poor. Typically a circular analysis area of about 5mm in diameter (for large analyser apertures) in XPS compared to about 0.2mm in AES, where a electron beam is used. X-rays can penetrate quite deeply into the specimen(around 1-10 μm), but due to the attenuation of photoelectrons, only those electrons emitted from less than 10-80 Å (depending on their kinetic energy) from the surface are analyzed.

The analysis of photoelectrons is performed by an electron energy analyzer, which in our case is a PHI Model 15-255GAR Precision Electron Energy Analyzer. This analyzer consists of two energy filters (which are arranged in series) — a hemispherical retarding grid system and a double-pass cylindrical mirror analyzer (CMA), as shown schematically in Fig. C.1. Electrons to be analyzed are dispersed on the basis of kinetic energy by the electrostatic field of CMA. A CMA acts as an energy window or band-pass filter which collects only a narrow energy range of electrons. It has two coaxial cylinders. The inner cylinder has two cylindrical grided apertures suitably positioned along its length. The outer cylinder is applied with a negative voltage so that photoelectrons leaving a suitably located sample (which is grounded) will be reflected back from the outer cylinder as shown in Fig. C.1. The same process repeats for the second stage CMA. Only those electrons with certain energy matched to the applied voltage can enter into the electron multiplier, as shown by the dashed lines in Fig. C.1. The energy of those electrons

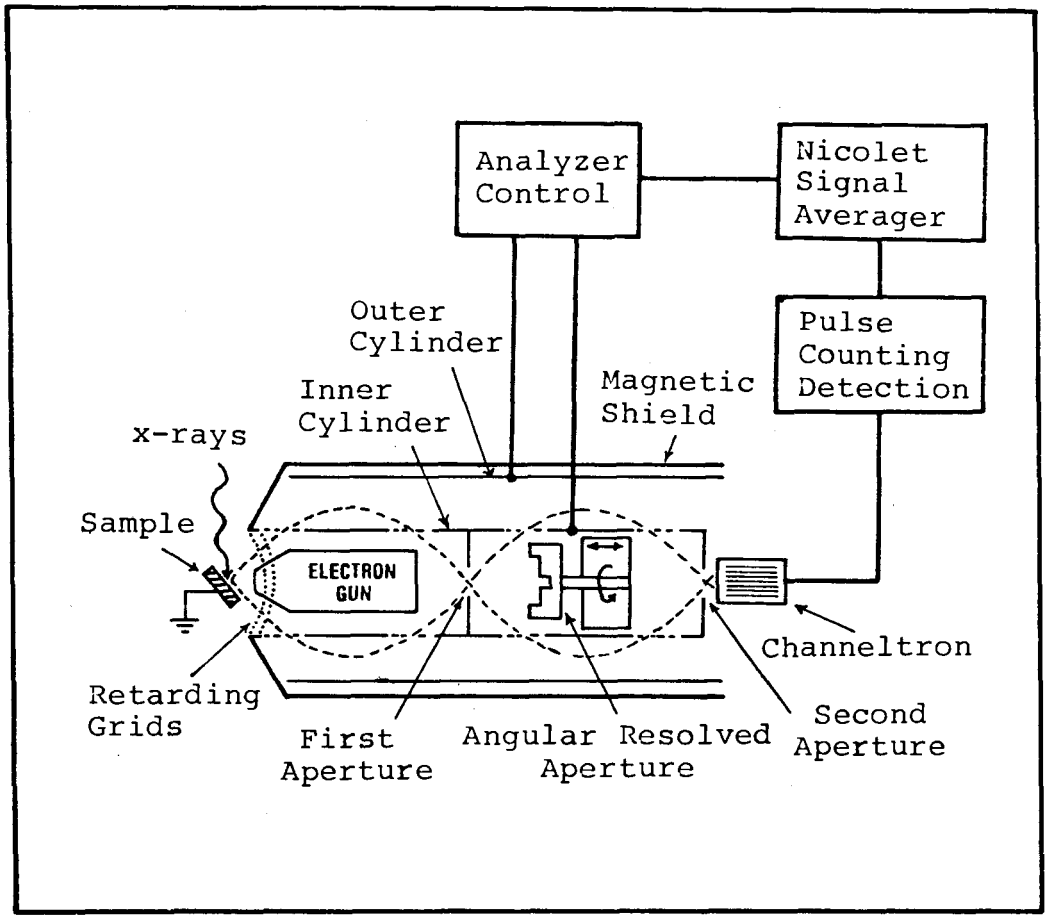

Fig. C.1. A schematic diagram of an XPS spectrometer system which uses a Cylindrical Mirror Analyzed (CMA).

which can pass through the CMA is related to the applied voltage by $E_{pass} = 1.7eV_{applied}$. The absolute energy resolution ΔE is proportional to the kinetic energy E of the electrons to be analyzed. It is customary to define the energy resolution as $\Delta E/E$ and $\Delta E/E$ is constant for a given CMA. For PHI15-255GAR, $\Delta E/E$ is about 0.6% for the small internal apertures (1mm in diameter) and 1.6% for the large apertures (4mm in diameter). In order to improve the absolute energy resolution, it is thus of advantage to use a spherical retarding grids to decrease the energy of the electrons emitted from the specimen and then measure them using CMA. The improved resolution, however, is achieved with a substantial loss in transmission due to the reduced image area on the specimen (because of grid refraction) and scattering from the grids. In the XPS measurements, the analyzer was always operated in the retarding mode. This gives a much better energy resolution. The retarding grids are used to scan the spectrum while the CMA is operated at a constant pass energy. This results in constant absolute energy resolution (ΔE) across the entire energy spectrum. When the larger apertures in CMA are used, a circular analysis area of about 5mm in diameter and energy resolution of 1.6% of the pass energy result. The smaller apertures in CMA give a smaller analysis area and better resolution, but the signal intensity decreases badly, so that they are usually not used in XPS.

The total energy resolution is determined by the analyzer resolution and the FWHM of the x-ray source. The poor resolution is a main disadvantage of XPS. Although by employing monochromatization the energy resolution can be improved to 0.5eV, it is still considerably poor compared to, e.g., UPS, which has a typical resolution of 0.2eV.

PHI15-255GAR provides also angular resolution . This is performed by an additional cylinder housed in the analyzer. This cylinder contains a slotted aperture for both 12° and 90° resolution (see Fig. C.2a). Its linear motion (up and down) and azimuthal location are controled by the "linear thimble" and the "rotary motion control" respectively. For ordinary use, this cylinder is in the upper ("open") position so that the electrons to be analyzed are not restricted by this cylinder. When angular resolution is used, this cylinder is driven down by rotating the

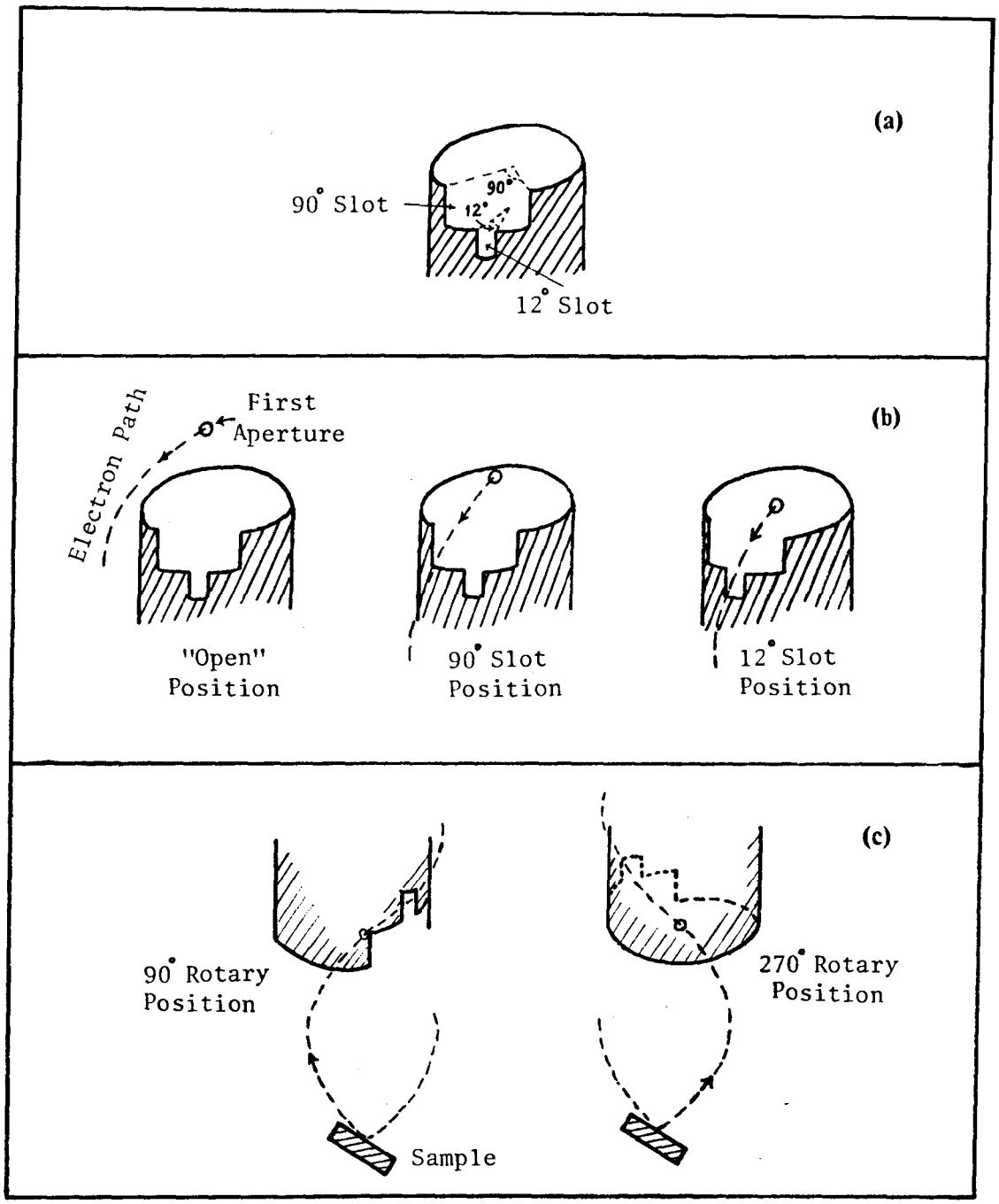

Fig. C.2. Schematic diagrams showing the angular resolved XPS arrangement: (a) a slotted cylinder, (b) relative position of the slotted cylinder with respect to the electron path, (c) relative position of the slot with respect to the sample.

linear thimble to the 90° or 12° position where only those electrons in the second stage of the double-pass analyzer passing through the 90° or 12° slot will be detected (Fig. C.2b). In an angular resolution measurement the sample is usually tilted with an angle of about 55° between its normal and the axis of the analyzer. Rotating the slotted cylinder changes the angular direction of the signal detected, resulting in the angular imformation of the signal (Fig. C.2c). As an example of the application of the angular resolution, one can measure the ratio of the O_2 1s signal to a signal from the specimen with the slotted cylinder at the 90° and 270° position on the rotary motion control (Fig. C.2c). A larger ratio obtained from the 90° position compared to that from the 270° position then indicates that O_2 are mostly come from the surface of the specimen.

The spectrometer system is completed by an electron multiplier, the pulse counting electronics and analyzer control electronics. The experimental data can be ploted in a x-y recorder or stored in a Nicolet signal averager and then transfered to a computer. For weak signals, repeated scans are needed to obtain better counting statistics.

Work function and binding energy

The work function ϕ is defined as the minimum energy required to extract an electron from a solid. The binding energy E_B is the energy separation between the Fermi level and the atomic orbital level of the electron. For a solid specimen in XPS, an electrical connection is made to the spectrometer so that both the specimen and the analyzer are at the same Fermi level. The work function of the specimen, ϕ_S, and that of the spectrometer, ϕ_A, are different however. The difference ($\phi_A - \phi_S$) acts as an accelerating or retarding potential to the electrons detected. Thus the binding energy measured in XPS is given by

$$E_B = h\nu - E_k - \phi_A$$

where E_k is the kinetic energy of the photoelectron measured by the spectrometer. It can be

seen that E_B depends only on the spectrometer work function ϕ_A and is independent of the work function of the sample ϕ_S. This is because that the electron losses energy ϕ_S to get out of the solid but gains the difference ($\phi_A - \phi_S$) upon entering the spectrometer. This becomes immediately clear if we draw an energy level diagram for a metallic specimen which is electrically connected to a metallic spectrometer (Fig. C.3). For a semiconducting or insulating specimen, the only difference is that the Fermi level is no longer the top level of the continuum but lies somewhere between the filled valence bands and the empty conduction bands.

The binding energy E_B is read directly from a digital meter in the electronic control unit, which should be calibrated. For our system, the calibration was carried out following the steps recommended in the PHI Model 11-055 manual using a high precision digital voltmeter (HP 3456A). Usually the Fermi level is used as the reference, and the following recommended values of gold and copper peaks should be used to check the accuracy of the instrument:

$Cu2p_{3/2}$	932.4 eV
$Cu(L_3M_5M_5)$	567.9 eV (Al radiation)
	334.9 eV (Mg radiation)
$Cu3p_{3/2}$	74.9 eV
$Au4f_{7/2}$	83.8 eV

In our instrument, the reading of the above peaks were in the range of ± 0.1eV from the recommended values.

For an insulating sample, the Fermi level may be anywhere in the energy gap and is defined only in thermal equilibium. In this case, it is better to reference all data to the edge of the valence band, which can be related to the vacuum level through optical measurements. Another problem for an insulating sample is the charging problem, i.e., the insulator will acquire a positive surface potential in photoemission due to the lack of conducting electrons. This potential will reduce the kinetic energy of the photoelectrons. A usual solution is to flood the sample surface with low-energy electrons using an electron flood gun. The amount of flooding is

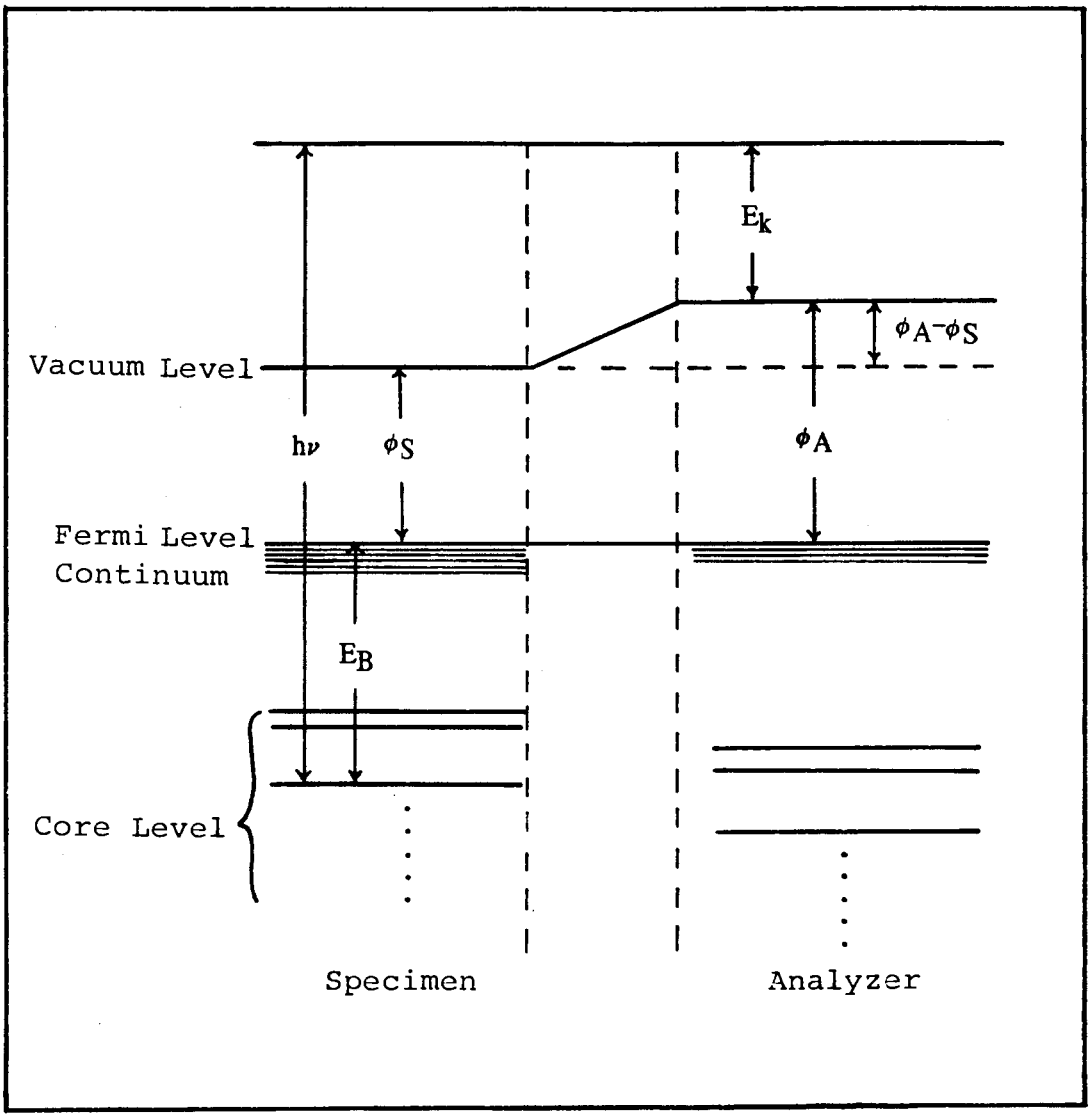

Fig. C.3. An energy level diagram showing the binding energy and work function for a metallic sample electrically connected with the spectrometer.

determined experimently by tuning the gun to minimize observed core level XPS line widths.

APPENDIX D : AES---AUGER ELECTRON SPECTROSCOPY

Instrument and experimental considerations

The AES instrument we used consists of an electron gun and an electron energy analyzer which is the same one in XPS but is operated in a differential mode. The electron beam is used in AES because it is better than x-ray beam as far as the beam intensity, the monochromaticity and the smaller penetrating power are concerned. These properties of the electron beam are very useful in improving the signal to noise ratio of Auger signals. In general, Auger yields are very low. The experimentally measured Auger current for a pure solid specimen is typically about 10^{-11} amperes, or about 10^{-5} of the primary beam current (Chattarji, 1976). Thus Auger peaks are only barely discernible in a strong background. The sensitivity is greatly increased by using the differential method, which is accomplished by superimposing a small a.c. voltage (the modulation voltage) on the energy analyzer. Synchronously detecting the output of the electron multiplier by using a lock-in amplifier one thus obtains the differentiated Auger signals. Over-modulation should be avoided so that the Auger peak shapes are not distorted. The selection of modulation voltage depends on the requirement of sensitivity and resolution. Usually a modulation of 2 eV to 6 eV (peak to peak) is sufficient.

The primary beam energy E_p has also large influence on the Auger yield. It is shown (Hink and Ziegler, 1969) that a maximun Auger yield occurs when $E_p \simeq 2.72E_w$, where E_w is the binding energy of the initial hole in the Auger process. In practical work, E_p should be at least 2.5 times higher than E but not too large. In our lab, primary beams of 2 KeV or 3 keV were usually used.

AES analysis for a layer-by-layer growth

Due to the inelastic scattering of Auger electrons, the substrate Auger signal will decay during the growth. Meanwhile the overlayer signal will increase. Using a hard-ball atomic model and the concept of inelastic mean free path, we can show that for a layer-by-layer growth, a AES intensity vs. thickness curve for both the substrate and the overlayer will have a linear dependence showing "breaks" with the first break corresponds to the completion of the first monolayer, the second break to the second monolayer, etc. . To show this, let us consider first the signal decay of the substrate. Assume the initial signal from a clean substrate surface is I_0. In the process of deposition of the first overlayer, the substrate signal coming from the underneath of the deposit will suffer a decay $\exp(-l_0/\lambda)$, where l_0 is the distance electrons traveled through one single overlayer and λ is called the electron inelastic mean free path. The signal from the uncovered area is not decayed by the deposit. The total substrate signal is thus

$$I_1 = I_0(1-S) + I_0 S\exp(-l_0/\lambda) \qquad \text{(D.2-1)}$$

where S is the fraction of the coverage of deposit. One can see immediately that I_1 has a linear dependance on S, with a slope $s_1 = dI_1/dS = I_0[\exp(-l_0/\lambda)-1]$, while S is proportional to the deposition time. When $S=1$, we have simply $I_{10} = I_0\exp(-l_0/\lambda)$, where I_{10} represents the substrate signal passing through one complete monolayer of deposit. Similarly, during the growth of the second monolayer, if we assume that the sticking coefficient for depositing on the deposit is the same as that on substrate, we have

$$\begin{aligned} I_2 &= I_{10}(1-S) + I_{10} S\exp(-l_0/\lambda) \\ &= I_0(1-S)\exp(-l_0/\lambda) + I_0 S\exp(-2l_0/\lambda) \end{aligned} \qquad \text{(D.2-2)}$$

Again I_2 has a linear dependance on S but has a different slope $s_2 = I_0[\exp(-l_0/\lambda)-1]\exp(-l_0/\lambda)$. The ratio of slope 2 to slope 1, s_2/s_1, is simply

$$s_2/s_1 = \exp(-l_0/\lambda) \qquad \text{(D.2-3)}$$

The same principle applies to the third overlayer and the ratio of the third slope to the first slope is $\exp(-2l_0/\lambda)$. So that we have $s_3/s_1 = (s_2/s_1)^2$.

For the signal of the deposit, it increases as more and more atoms deposit on the substrate. Assuming the Auger generation rate G per unit area in a monolayer of deposit, in the process of completing the first overlayer, the signal intensity from the deposit for a layer by layer growth would be simply $I_1 = ASG$, where A is a proportional constant and S the fraction of coverage. Thus I_1 is again linearly dependent on S with a slope $s_1 = AG$. For $S=1$, $I_{10} = AG$. In the completion of the second monolayer, $I_2 = AG[1 + S\exp(-l_0/\lambda)]$, which has also a linear dependence on S with a slope $s_2 = AG\exp(-l_0/\lambda)$.

$$\begin{aligned}
\text{Similarly, } I_3 &= AG[1 + \exp(-l_0/\lambda) + S\exp(-2l_0/\lambda)], \\
&\cdots\cdots\cdots\cdots \\
&\cdots\cdots\cdots\cdots \\
I_n &= AG[1 + \exp(-l_0/\lambda) + \cdots\cdots + S\exp(-(n-1)l_0/\lambda)], \\
I_\infty &= AG[1 - \exp(-l_0/\lambda)]^{-1}.
\end{aligned}$$

Also we have $s_2/s_1 = \exp(-l_0/\lambda)$ and $s_3/s_1 = (s_2/s_1)^2 = \exp(-2l_0/\lambda)$.

When AES is used, the sample is perpendicular to the electron beam. Considering the geometry correction of 42° of the electron analyzer, we have $l_0 = d_0/\cos 42^\circ$, where d_0 is the thickness of one monolayer. In XPS, the geometry correction is hard to make since the sample is tilted.

The signal intensity in AES is measured by the peak-to-peak height of the Auger signal in the derivative mode. This is justified because the peak-to-peak height in the derivative mode is proportional to the Auger peak area provided the Auger line profile per atom is constant (Weber and Johnson, 1969). It is noted that along with the inelastic scattering there is also an elastic

back scattering effect which has an influence on the AES (XPS) signal. However, this effect is negligible in the AES (XPS) growth determinations (Dwyer and Matthew, 1984).

APPENDIX E: COMPUTER PROGRAMS

Computer Program for Backgound Subtraction Using the Shirley Method

```
      SUBROUTINE DATSUB
C
C DATA INPUT FOR BASELINE FITTING
C
C PURPOSE:
C
C NORMALLY WE JUST READ THE DATA IN AND PASS IT TO GANDER
C FOR PLOTTING. THIS ROUTINE DOES SEVERAL THINGS MORE:
C
C 1) READ AND PASS DATA TO GANDER
C 2) READ AND PASS DATA PLUS SAVE THE DATA IN SOME VECTORS
C 3) READ AND PASS THE VECTORS OF DATA TO GANDER, LEAVING
C    THE INPUT FILE ALONE
C
C THESE OPTIONS ARE SELECTED THROUGH THE INTEGER SWITCH
C 'SELECT' WHICH CAN BE SET TO 1, 2, OR 3. OTHER VALUES
C ARE INVALID AND CAUSE OPTION 1 TO BE FOLLOWED.
C
      REAL*8 S(1024), SZ(1024), B1(1024), B0(1024), E(1024)
      COMMON /BASELN/ S, SZ, B1, B0, E, IPMAX, ISTART, IEND
      INTEGER*4 F8 /8/
C
C 'S'  HOLDS THE COUNTS PER CHANNEL
C 'SZ' HOLDS S(I) - S(IEND)'
C 'E'  HOLDS THE CHANNEL NUMBER (PROPORTIONAL TO ENERGY)
C 'B0' HOLDS THE OLD BASE-LINE VALUES
C 'B1' HOLDS THE NEW BASE-LINE VALUES
C
      COMMON /DREALV/ GS, GE, GEOFF, GSZ, GB1, GSZMB1, AK
      COMMON /DREALV/ ESTART, EEND, POINTS
      REAL*8 DS, DE, DEOLD
C
C 'GS' GANDER PLOTTING VARIABLE FOR 'S'
C 'GE' GANDER PLOTTING VARIABLE FOR 'E'
C 'GEOFF' OFFSET TO BE ADDED TO EACH 'E' VALUE READ IN
C
      COMMON /CONTRL/ EOF
C
C 'EOF' SWITCH SET BY GANDER TO TELL US IF WE ARE READING
C       A NEW FILE OR STILL READING AN OLD ONE
C
      COMMON /DINT/ SELECT
      INTEGER*4 SELECT
C
C THE SWITCH USED TO SELECT THE DATSUB FUNCTION
```

```
C
      COMMON /DLOGI/ LSAVE
      LOGICAL LSAVE
C
C SWITCH USED TO ALLOW SAVING OF ENERGY DATA ONLY AFTER FITTING
C HAS BEEN DONE TO A FILE. IT WILL BE TURNED ON BY THE 'FINAL'
C MACRO AND SET OFF WHEN A NEW FILE IS READ IN
C
      LOGICAL*1 FDFILE(60) /60*' '/
      LOGICAL*1 FDOLD(60)  /60*' '/
C
C STRING TO HOLD FILE NAME ATTACHED TO UNIT 10,
C PREVENTS NC QUESTION ON EACH 'DATA' COMMAND
C
      COMMON /ESL/ ESLOPE, EINT, NOR2
      REAL*8 ESLOPE, EINT
C
C ENTRY: BRANCH TO OPTION SELECTED
C
      IF (SELECT .LT. 1 .OR. SELECT .GT. 3) SELECT = 1
      GO TO (10, 10, 90), SELECT
C
C SELECT = 1 OR 2, READ THE DATA FILE
C
   10 IF (EOF .EQ. 0.0) GO TO 20
C
C CONVERT ENERGY VALUES
C
      IF (SELECT .EQ. 2) ESLOPE = (EEND-ESTART)/(POINTS-1)
      IF (SELECT .EQ. 2) EINT   = ESTART - ESLOPE
      LSAVE = .FALSE.
      EOF = 0.0
      DEOLD = -100.0
      IPTR = 0
C
C INITIALIZE FOR 1 OR 2 COLUMN DATA
C
      CALL FTNCMD('QUERY FDNAME 10;', 0, FDFILE)
C
C IF NEWFILE = OLDFILE WE ASSUME NOR2 IS SET RIGHT
C
      IF (LCOMC(60, FDFILE, FDOLD) .EQ. 0) GO TO 13
      CALL MOVEC(60, FDFILE, FDOLD)
   11 WRITE (6,12)
   12 FORMAT ('&NICOLET OR 2-COLUMN DATA (1 OR 2)')
      CALL FREAD(5, 'I:', NOR2)
      IF (NOR2 .NE. 1 .AND. NOR2 .NE. 2) GO TO 11
C
C NOR2 = 1 —> NICOLET DATA, NOR2 = 2 —> 2-COLUMN DATA
C
   13 CALL FREAD(-2, 'ENDFILE', 1, 'ERROR', 2, 'VERB', 0, 'ENDLINE',
     # 'STREAM')
```

```
C
C DUMMY READ FOR FIRST LINE IF IN NICOLET FILE
C
      IF (NOR2 .EQ. 1) CALL FREAD(10, ':', F, &50, &40)
C
C ENTRY TO NORMAL READ
C
   20 IF (NOR2 .EQ. 1) CALL FREAD('*', 'R*8:', DS, &70, &40)
      IF (NOR2 .EQ. 2) CALL FREAD(10, '2R*8:', DE, DS, &70, &20)
C
C WATCH FOR DUPLICATE ENERGY READINGS (WILL KILL INTEGRATION
C PACKAGE)
C
   30 IF (NOR2 .EQ. 2 .AND. DE .EQ. DEOLD) GO TO 20
      DEOLD = DE
      IPTR = IPTR + 1
      IF (NOR2 .EQ. 1) DE = IPTR
C
C SAVE STARTING ENERGY VALUE IF 2-COLUMN DATA
C
      IF (NOR2 .EQ. 2 .AND. IPTR .EQ. 1 .AND. SELECT .EQ. 1)
     #    ESTART = DE
C
C CONVERT NICOLET INDEPENDENT DATA VALUES TO ENERGY VALUES
C IF SELECT = 2 (IE, WE ARE SAVING DATA IN ARRAYS FOR LATER
C BASELINE FITTING)
C
      IF (SELECT .EQ. 2 .AND. NOR2 .EQ. 1) DE = ESLOPE*IPTR + EINT
      GS = DS
      GE = DE - GEOFF
      GSZ = 0.0
      GB1 = 0.0
      GSZMB1 = 0.0
      IF (SELECT .EQ. 1) RETURN
C
C SELECT = 2) PACK DATA POINT INTO ARRAY
C
      IF (IPTR .GT. 1024) GO TO 70
      S(IPTR) = DS
      SZ(IPTR) = DS
      E(IPTR) = DE
      B0(IPTR) = DS
      B1(IPTR) = 0.0D0
      RETURN
C
C ERROR READING NICOLET INPUT LINE, SKIP LINE AND CONTINUE
C
   40 CALL FREAD(10, 'R*8:', DS, &70, &40)
      GO TO 30
C
C HARD EOF, NO DATA READ AT ALL!
C
```

```
   50 EOF = -1.0
      WRITE (6,60)
   60 FORMAT (' *** ERROR *** DATA FILE IS EMPTY')
      REWIND 10
      CALL FREAD(-1, 'ENDFILE', 'ERROR', 'VERB', 'ENDLINE')
      RETURN
C
C NORMAL EOF AFTER SOME DATA HAS BEEN READ IN
C
   70 EOF = 1.0
      IF (NOR2 .EQ. 2 .AND. SELECT .EQ. 1) EEND = GE
      IPMAX = IPTR
      POINTS = IPTR
      ISTART = 1
      IEND = IPMAX
      REWIND 10
      CALL FREAD(-1, 'ENDFILE', 'ERROR', 'VERB', 'ENDLINE')
C
C SORT THE DATA BEFORE RETURNING IF 2-COLUMN FORMAT
C
      IF (NOR2 .EQ. 1 .OR. SELECT .EQ. 1) RETURN
      CALL SORT3('S=FL,,,8 END ', E(1), E(IPMAX), F8, S(1),  F8)
      CALL SORT3('S=FL,,,8 END ', E(1), E(IPMAX), F8, SZ(1), F8)
      CALL SORT3('S=FL,,,8 END ', E(1), E(IPMAX), F8, B0(1), F8)
      RETURN
C
C READ DATA VECTORS, IPTR WAS SET PREVIOUSLY TO THE # OF POINTS
C
   90 IF (EOF .EQ. 0.0) GO TO 100
      IF (IPMAX .LT. 0 .OR. IPMAX .GT. 1024) GO TO 50
      EOF = 0.0
      IP = ISTART - 1
  100 IP = IP + 1
      IF (IP .GT. IEND) GO TO 110
      GS = S(IP)
      GE = E(IP) - GEOFF
      GSZ = SZ(IP)
      GB1 = B1(IP)
      GSZMB1 = SZ(IP) - B1(IP)
      RETURN
  110 EOF = 1.0
      RETURN
      END
C
C ROUTINE TO FIT THE BASELINE
C
      SUBROUTINE BASEFT(K)
      REAL*8 S0(1024), K, ERR
      REAL*8 S(1024), SZ(1024), B1(1024), B0(1024), E(1024)
      COMMON /BASELN/ S, SZ, B1, B0, E, IPMAX, ISTART, IEND
C
C COMPUTE THE NEW K VALUE
```

```
C
      IDEL = IEND - ISTART + 1
      DO 10 I = ISTART, IEND
        S0(I) = SZ(I) - B0(I)
   10 CONTINUE
      IFAIL = 1
      CALL D01GAF(E(ISTART), S0(ISTART), IDEL, K, ERR, IFAIL)
      IF (IFAIL .NE. 0) CALL DERROR(IFAIL)
      K = SZ(ISTART) / K
C
C NOW RE-COMPUTE THE BASE LINE
C
      ILIM = IEND - 3
      DO 20 IE = ISTART, ILIM
        IFAIL = 1
        CALL D01GAF(E(IE), S0(IE), IEND - IE + 1, B1(IE), ERR, IFAIL)
        IF (IFAIL .NE. 0) CALL DERROR(IFAIL)
        B1(IE) = B1(IE) * K
        B0(IE) = B1(IE)
   20 CONTINUE
      ILINC = ILIM + 1
      DO 30 IE = ILINC, IEND
        B1(IE) = B0(IE)
   30 CONTINUE
      RETURN
      END
C
C EXPLAIN D01GAF ERROR MESSAGES
C
      SUBROUTINE DERROR(IFAIL)
      IF (IFAIL .GT. 3 .OR. IFAIL .LT. 1) IFAIL = 4
      GO TO (10, 30, 50, 70), IFAIL
   10 WRITE (6,20)
   20 FORMAT (' **** INTEGRATION ERROR 1: FEWER THAN 4 POINTS', 1X,
     #        'SUPPLIED')
      RETURN
   30 WRITE (6,40)
   40 FORMAT (' **** INTEGRATION ERROR 2: ENERGY VALUES NOT SORTED')
      RETURN
   50 WRITE (6,60)
   60 FORMAT (' **** INTEGRATION ERROR 3: DUPLICATE ENERGY VALUES')
      RETURN
   70 WRITE (6,80)
   80 FORMAT (' **** INTEGRATION ERROR 4: INTEGRATION FAILURE')
      RETURN
      END
C
C ROUTINE TO RETURN XWHERE, YWHERE TO A PROGRAM
C
      SUBROUTINE WXY(X, Y)
      REAL*8 X, Y
      REAL*4 XLINK(39)
```

```
      COMMON /CONTRL/ XLINK, XWHERE, YWHERE
      X = XWHERE
      Y = YWHERE
      RETURN
      END
C
C *** USUB CONTROL PROGRAM ****
C
      SUBROUTINE USUB(BSEL)
      REAL*8 S(1024), SZ(1024), B1(1024), B0(1024), E(1024)
      COMMON /BASELN/ S, SZ, B1, B0, E, IPMAX, ISTART, IEND
      COMMON /DREALV/ GS, GE, GEOFF, GSZ, GB1, GSZMB1, AK
      COMMON /DREALV/ ESTART, EEND, POINTS
      COMMON /ESL/ ESLOPE, EINT, NOR2
      INTEGER*4 BSEL
      REAL*8 EW, SW, SLOPE, K, ESLOPE, EINT
      LOGICAL*1 FNAME(60), FYLE(40), CCID(4)
      LOGICAL EQUC
      COMMON /DLOGI/ LSAVE
      LOGICAL LSAVE
C
C SELECT OPTION
C
      IF (BSEL .LT. 1 .OR. BSEL .GT. 9) RETURN
      GO TO (10, 30, 80, 100, 150, 180, 190, 210, 420), BSEL
C
C OPTION 1) TELL USER TO SELECT START OF FIT ZONE
C
   10 WRITE (6,20)
   20 FORMAT (' *** SELECT START OF FITTING ZONE')
      RETURN
C
C OPTION 2) GET LOCATION AND FIND IT IN VECTORS
C
   30 CALL WXY(EW, SW)
      DO 40 I = 1, IPMAX
        IF (E(I) .GE. EW) GO TO 60
   40 CONTINUE
      WRITE (6,50)
   50 FORMAT (' *** ILLEGAL LOCATION CHOSEN, TAKING START OF DATA')
      ISTART = 1
      RETURN
   60 ISTART = I
      WRITE (6,70) ISTART
   70 FORMAT (' **** ISTART = ', I4)
      RETURN
C
C OPTION 3) TELL USER TO SELECT END OF FIT ZONE
C
   80 WRITE (6,90)
   90 FORMAT (' *** SELECT END OF FITTING ZONE')
      RETURN
```

```
C
C OPTION 4) GET LOCATION AND FIND IT IN VECTORS
C
  100 CALL WXY(EW, SW)
      DO 110 I = 1, IPMAX
        IF (E(I) .GE. EW) GO TO 130
  110 CONTINUE
      WRITE (6,120)
  120 FORMAT (' *** ILLEGAL LOCATION CHOSEN, TAKING END OF DATA')
      IEND = IPMAX
      RETURN
  130 IEND = I
      WRITE (6,140) IEND
  140 FORMAT (' **** IEND = ', I4)
      RETURN
C
C OPTION 5) COMPUTE APPROXIMATE BASELINE
C
C SUBTRACT OFF END COUNTS
C
  150 DO 160 I = ISTART, IEND
        SZ(I) = S(I) - S(IEND)
  160 CONTINUE
C
C FORM LINEAR REGION
C
      SLOPE = (SZ(IEND) - SZ(ISTART)) / (E(IEND) - E(ISTART))
      SB = SZ(ISTART) - SLOPE * E(ISTART)
C
C IF LINEAR BASELINE EXCEEDS COUNTS PER CHANNEL VALUE, USE SZ
C FOR B0(I) AND NOT THE LINEAR ESTIMATE
C
      DO 170 I = ISTART, IEND
        B0(I) = SLOPE * E(I) + SB
        IF (B0(I) .GT. SZ(I)) B0(I) = SZ(I)
        B1(I) = B0(I)
  170 CONTINUE
      RETURN
C
C OPTION 6) INVOKE THE BASELINE FIT
C
  180 CALL BASEFT(K)
      AK = K
      RETURN
C
C OPTION 7) EXPLAIN
C
  190 WRITE (6,200)
  200 FORMAT (2X,' SETUP    : FILL THE SCREEN WITH THE RAW DATA'/2X,
     1' ZONE     : SELECT FITTING ZONE USING CROSS-HAIRS'/2X,
     2' BASELINE : SELECT AND DRAW THE FIRST LINEAR BASELINE'/2X,
     3' FIT      : DRAW ON A NEW BASELINE CURVE'/2X,
```

```
     4' KFIT     : COMPUTE NEW BASELINE BUT DO NOT DRAW IT ON'/2X,
     5' CFIT     : DRAW ONLY THE LATEST BASELINE, ERASE ALL PREVIOUS BAS
     6ELINES'/2X,
     7' FINAL    : DRAW ONLY THE CORRECTED ENERGY CURVE'/2X,
     8' SAVE     : SAVE CORRECTED ENERGY DATA'/2X,
     9' BOX      : FILL SCREEN WITH CURRENT PLOT'//)
      RETURN
C
C OPTION 8) SAVE DATA IN A FILE
C
  210 IF (LSAVE) GO TO 230
      WRITE (6,220)
  220 FORMAT (' *** ERROR: NO ENERGY DATA TO SAVE YET!!!!')
      RETURN
  230 WRITE (6,240)
  240 FORMAT ('&ENTER FILENAME TO SAVE ENERGY CURVE IN')
      CALL FREAD(-2, 'ENDFILE', 1, 'ERROR', 2, 'VERB', 0)
      CALL FREAD(5, 'S:', FYLE, 40, &410, &230)
C
C GO TO 410 IF NULL ENTRY
C
      IF (LCOMC(6,'      ',FYLE) .EQ. 0) GO TO 410
C
C CHECK FOR EXISTENCE
C
      IEMP = 0
      CALL CREATE(FYLE, 1, 0, 256, &250, &310, &310, &310, &270, &310,
     1&290)
      GO TO 330
C
C ERROR: FILE ALREADY EXISTS
C
  250 WRITE (6,260)
  260 FORMAT ('&*** ERROR: FILE ALREADY EXISTS, OK TO EMPTY (Y OR N)')
      CALL FREAD(5,'S:',CCID(1),1,&410,&250)
      IEMP = 1
      IF (EQUC(CCID(1),'Y')) GO TO 330
      GO TO 230
  270 WRITE (6,280)
  280 FORMAT (' *** ERROR: ILLEGAL FILE NAME, ENTER ANOTHER NAME')
      GO TO 230
  290 WRITE (6,300)
  300 FORMAT (' *** ERROR: NO DISK SPACE LEFT IN THIS ACCOUNT!!!!')
      GO TO 410
  310 WRITE (6,320)
  320 FORMAT (' *** ERROR: CANNOT CREATE FILE / SYSTEM ERROR')
      GO TO 410
C
C FILE HAS BEEN CREATED, ATTACH UNIT #12 TO IT
C
  330 CALL FTNCMD('ASSIGN 12 = ?;', 0, FYLE)
      IF (IEMP .EQ. 1) CALL EMPTYF(12)
```

```
C
C GET THE FILE NAME ATTACHED TO UNIT 10 AND WRITE IT IN THE FILE
C
      CALL FTNCMD('QUERY FDNAME 10;', 0, FNAME)
      CALL GUINFO('SIGNONID ', CCID)
      IF ( .NOT. EQUC(FNAME(5),':')) GO TO 340
      CALL MOVEC(4, FNAME(1), CCID(1))
      CALL MOVEC(55, FNAME(6), FNAME(1))
      CALL MOVEC(5, '      ', FNAME(56))
  340 CALL FINDC(FNAME, 60, ' ', 1, 1, ILEN, ICF, &350)
      GO TO 360
  350 ILEN = 61
  360 ILEN = ILEN - 1
      WRITE (12,370) CCID, (FNAME(I),I=1,ILEN)
  370 FORMAT ('*'/'* BASELINE ENERGY PROFILE OF ', 4A1, ':', 60A1)
      WRITE (12,380)
  380 FORMAT ('*')
C
C DUMP THE DATA FROM THE VECTORS
C
      DO 400 I = ISTART, IEND
        IF (NOR2 .EQ. 1) SE = I*ESLOPE + EINT
        IF (NOR2 .EQ. 2) SE = E(I)
        SW = SZ(I) - B1(I)
        WRITE (12,390) SE, SW
  390   FORMAT (2X, 2G16.8)
  400 CONTINUE
  410 CALL FREAD(-1,'ENDFILE','ERROR','VERB')
      RETURN
C
C OPTION 9) ENERGY FIT
C
  420 IF (NOR2 .EQ. 2) GO TO 460
  421 WRITE (6,430)
  430 FORMAT ('&ENTER CHANNEL #    1 VOLTAGE')
      CALL FREAD(-2, 'ENDFILE', 1, 'ERROR', 2, 'VERB', 0)
      CALL FREAD(5, 'R:', ESTART, &421, &421)
  440 WRITE (6,450) IPMAX
  450 FORMAT ('&ENTER CHANNEL #', I4, ' VOLTAGE')
      CALL FREAD(5, 'R:', EEND, &440, &440)
      CALL FREAD(-1, 'ENDFILE', 'ERROR', 'VERB')
      RETURN
  460 RETURN
      END
```

Computer Program for Curve Subtractions

```
COMMON /CREAL/  CX, CY, CS, ERROR, IPTR
COMMON /CREAL/  SCALE, CYOFF, CXOFF
COMMON /CCMPX/  CSY
COMMON /CINT/   KNOTS, CN, CER, CSMOOTH
COMMON /DREALV/ DX, DY, DSCALE, DYOFF, DXOFF
COMMON /DINT/   DN, CDFLG
*
* CALC DEFINITIONS
*
CPLOT=CSY,CAGAINST=CX,ANSWER=CX,CY,CS,CSY
STEPVAR=IPTR,FROM=1,STEP=1,AINCNO=256,ERROR=0,KNOTS=20
SCALE=1,CYOFF=0,CXOFF=0,CSMOOTH=0
*
* DATA DEFINITIONS
*
DPLOT=DY,DAGAINST=DX,DLNTYP=0
DSCALE=1,DYOFF=0,DXOFF=0
*
* MACROS
*
MACRO/CWHERE/USUB=2
MACRO/DWHERE/USUB=3
MACRO/DBOX/TOP=YXVD,DTOP=TOP,BOTTOM=0,DBOT=0,REDRAW
MACRO/CBOX/TOP=YXVC,DTOP=TOP,BOTTOM=0,DBOT=0,REDRAW
MACRO/BOX/TOP=YXVB,DTOP=TOP,BOTTOM=0,DBOT=0,REDRAW
MACRO/WINDOW/START=XN,END=XX,TOP=YXVB,DTOP=TOP,
  BOTTOM=YNVB,DBOT=BOTTOM,REDRAW
MACRO/SMOOTH/NEWPAGE,NOPLOT=1,CSMOOTH=0,USUB=5,
  SCALE=1,CYOFF=0,CPLOT=CSY,CALC,NOPLOT=0,WINDOW
MACRO/FIT/CPLOT=CS,UNDO,USUB=1,NOPLOT=1,CALC,NOPLOT=0,REDRAW
MACRO/UNDO/NEWPAGE,NOPLOT=1,SCALE=1,CYOFF=0,
  CSMOOTH=1,CALC,DATA,NOPLOT=0,WINDOW
MACRO/LOAD/NEWPAGE,NOPLOT=1,CSMOOTH=-1,USUB=5,
  SCALE=1,CYOFF=0,CPLOT=CY,CALC,NOPLOT=0,WINDOW
MACRO/CUT/CPLOT=CY,USUB=6,NEWPAGE,CSMOOTH=1,
  NOPLOT=1,CALC,NOPLOT=0,WINDOW,CSAVE
MACRO/CSAVE/CDFLG=1,USUB=7
MACRO/DSAVE/CDFLG=2,USUB=7
MACRO/SUB/USUB=8,NOPLOT=1,DATA,BOX,NOPLOT=0,DSAVE
$R *FTN SCARDS=ATLN:CURV(100) SPUNCH=ATLN:CURV(-500,-100)
$SOURCE PREVIOUS
$R ANDR:GANDER+ATLN:CURV(-500,-100) 5=ATLN:CURV(-99,-1)
$SOURCE PREVIOUS
CC
CC *** CALSUB TO SUPERVISE DATA SMOOTHING
CC
      SUBROUTINE CALSUB
CC
      REAL*8 CX(2048), CY(2048), CS(2048), ERROR
```

```
      INTEGER*4 UNIT, KNOTS, N, NMAX, IER
      COMMON /COMCV/ CX, CY
CC
      REAL*4 X, Y, S, ERR
      COMPLEX*8 CSR
      COMMON /CREAL/ X, Y, S, ERR, APTR
      COMMON /CREAL/ SCALE, CYOFF, CXOFF
      COMMON /CCMPX/ CSR
      COMMON /CINT/ KNOTS, N, IER, ISMOO
      COMMON /CONTRL/ EOF, XLINK(10), AINCNO
CC
      INTEGER*4 NMAX /2048/
      INTEGER*4 UNIT /11/
      LOGICAL*1 OFYLE(61) /61*' '/
      LOGICAL*1  FYLE(61) /61*' '/
CC
      IF (EOF .EQ. 0.0) GO TO 70
CC
CC ARE WE SMOOTHING OR CURVE MATCHING?
CC
      EOF = 0.0
      IF (ISMOO .GT. 0) GO TO 70
CC
CC GET CURRENT FILE NAME THAT UNIT 11 IS ATTACHED TO
CC
      CALL FTNCMD('QUERY FDNAME 11;', 0, FYLE)
      CALL FINDC(FYLE, 60, ' ', 1, 1, ILEN, ICF, &10)
      DO 5 I = ILEN, 61
        CALL MOVEC(1, ' ', FYLE(I))
    5 CONTINUE
      GO TO 20
   10 ILEN = 61
CC
CC COMPARE CURRENT FILE NAME TO THE OLD NAME
CC
   20 IF (LCOMC(60, FYLE, OFYLE) .EQ. 0) GO TO 40
CC
CC IF FILES ARE EQUAL, SKIP THE READ. IF FILES ARE
CC DIFFERENT, REPLACE THE OLD FILE NAME WITH THE NEW
CC FILE NAME
CC
      CALL MOVEC(60, FYLE, OFYLE)
CC
CC TRY TO LOAD THE DATA IN THE NEW FILE
CC
      CALL DLOAD(UNIT, CX, CY, N, NMAX, ICOL, IER)
      AINCNO = N
CC
CC CHECK FOR READING ERROR
CC
      IF (IER .EQ. 0) GO TO 40
      WRITE (6,30) IER
```

```
  30 FORMAT (' ...ERROR RETURN FROM "DLOAD", CER = ', I5)
     EOF = -1.0
     RETURN
CC
CC DO WE SMOOTH OR JUST DISPLAY THE DATA?
CC
  40 IF (ISMOO .EQ. 0) GO TO 45
     DO 41 I = 1, N
       CS(I) = CY(I)
  41 CONTINUE
     GO TO 70
CC
CC ------> SMOOTH DATA
CC
  45 CALL SMOOTH(CX, CY, CS, N, KNOTS, ERROR, IER)
CC
CC CHECK FOR SMOOTHING ERROR
CC
     IF (IER .EQ. 0) GO TO 60
     WRITE (6,50) IER
  50 FORMAT (' ...ERROR RETURN FROM "SMOOTH", CER = ', I5)
     EOF = -1.0
     RETURN
  60 ERR = ERROR
CC
CC PASS DATA BACK TO GANDER FOR PLOTTING
CC
  70 IPTR = APTR
     X = CX(IPTR)
     Y = CY(IPTR)
     S = CS(IPTR)
     X = X - CXOFF
     Y = SCALE*Y + CYOFF
     S = SCALE*S + CYOFF
     CSR = CMPLX(Y, S)
     RETURN
     END
CC
CC *** DATSUB ROUTINE TO READ IN AND LOAD DATA INTO VECTORS
CC
     SUBROUTINE DATSUB
     COMMON /DREALV/ DX, DY, DSCALE, DYOFF, DXOFF
     COMMON /DINT/   DN, ICDFLG
     COMMON /CONTRL/ EOF
     COMMON /COMDV/  DXV, DYV
     REAL*8 DXV(1024), DYV(1024)
     INTEGER*4 DN
     INTEGER*4 DNMAX /1024/
     LOGICAL*1 OFYLE(61) /61*' '/
     LOGICAL*1  FYLE(61) /61*' '/
CC
     IF (EOF .EQ. 0) GO TO 80
```

```
      EOF = 0.0
CC
CC GET CURRENT FILE NAME THAT UNIT 10 IS ATTACHED TO
CC
      CALL FTNCMD('QUERY FDNAME 10;', 0, FYLE)
      CALL FINDC(FYLE, 60, ' ', 1, 1, ILEN, ICF, &10)
      GO TO 20
   10 ILEN = 61
CC
CC COMPARE CURRENT FILE NAME TO THE OLD NAME
CC
   20 IF (LCOMC(ILEN, FYLE, OFYLE) .EQ. 0) GO TO 70
CC
CC IF FILES ARE EQUAL, SKIP THE READ. IF FILES ARE
CC DIFFERENT, REPLACE THE OLD FILE NAME WITH THE NEW
CC FILE NAME
CC
      CALL MOVEC(ILEN, FYLE, OFYLE)
CC
CC TRY TO LOAD THE DATA IN THE NEW FILE
CC
      CALL DLOAD(10, DXV, DYV, DN, DNMAX, ICOL, IER)
CC
CC IF IER .NE. 0 THEN THERE WAS AN ERROR READING THE DATA
CC
      IF (IER .EQ. 0) GO TO 70
      EOF = -1.0
      RETURN
CC
CC DATA RETURN SEGMENT, PICK POINTS OUT OF THE VECTOR
CC
   70 IPTR = 0
   80 IPTR = IPTR + 1
      IF (IPTR .GT. DN) GO TO 90
      DX = DXV(IPTR) + DXOFF
      DY = DSCALE*DYV(IPTR) + DYOFF
      RETURN
   90 EOF = 1.0
      RETURN
      END
CC
CC SUBROUTINE TO SMOOTH INPUT DATA
CC
      SUBROUTINE SMOOTH(DX, DY, CY, N, KNOTS, ERROR, IER)
      INTEGER*4 UNIT, N, KNOTS, IER
      INTEGER*4 IC   /28/
      INTEGER*4 MODE /0/
      REAL*8 DX(N), DY(N), CY(N), C(28,3), Y(28), XK(28)
      REAL*8 XKSTEP, XK1, ERROR, WK(34816), D
      COMMON /SPFIT/ C, Y, XK, NXK1
CC
CC SELECT KNOTS, MUST BE LESS THAN OR EQUAL TO 28
```

```
CC
      NXK = KNOTS
      IF (NXK .GT. 28) NXK = 28
      XKSTEP = (DX(N) - DX(1)) / (NXK-1)
      XK(1) = DX(1) - (DX(2)-DX(1))
      XK(NXK) = DX(N) + (DX(2)-DX(1))
      XK1 = XK(1)
      NXK1 = NXK - 1
      DO 10 I = 2, NXK1
        XK(I) = XK1 + XKSTEP*DFLOAT(I-1)
   10 CONTINUE
CC
CC CALCULATE THE SPLINE COEFFICIENTS
CC
      CALL ICSVKU(DX, DY, N, XK, NXK, Y, C, IC, ERROR,WK,IER)
      IF (IER .NE. 0) RETURN
CC
CC EVALUATE SMOOTHED CURVE
CC
      J = 1
      DO 30 I = 1, NXK1
   20   IF (DX(J) .GT. XK(I+1)) GO TO 30
        D = DX(J) - XK(I)
        CY(J) = ((C(I,3)*D + C(I,2))*D + C(I,1))*D + Y(I)
        J = J + 1
        IF (J .GT. N) GO TO 40
        GO TO 20
   30 CONTINUE
   40 CONTINUE
      RETURN
      END
CCCCCCCCCCCCCCCCCCCCCCCCCCCCCCCCCCCCCCCCCCCCCCCCCCCCCCCCCCCCCCCCCCCC
CCCCCCCCCCCCCCCCCCCCCCCCCCCCCCCCCCCCCCCCCCCCCCCCCCCCCCCCCCCCCCCCCCCC
CC
CC ROUTINE TO LOAD DATA FROM A SPECIFIED I/O UNIT
CC
      SUBROUTINE DLOAD(UNIT, X, Y, N, NMAX, ICOL, IER)
CC
CC UNIT   :  FORTRAN INPUT UNIT NUMBER ATTACHED TO DATA FILE
CC X      :  REAL*8 VECTOR TO HOLD X DATA
CC Y      :  REAL*8 VECTOR TO HOLD Y DATA
CC N      :  NUMBER OF DATA POINTS READ INTO THE VECTORS
CC NMAX   :  MAXIMUM DIMENSION OF X AND Y
CC ICOL   :  NUMBER OF COLUMNS IN DATA FILE
CC IER    :  ERROR PARAMETER, 0 MEANS DATA READ, 1 MEANS ERROR
CC
      INTEGER*4 UNIT, N, NMAX, ICOL
      REAL*8 X(NMAX), Y(NMAX)
      REAL*8    DCOL(25)
      INTEGER*4 NDMAX /25/
CC
CC REWIND INPUT UNIT TO START
```

```
CC
      REWIND UNIT
CC
CC SET FREAD PARAMETERS
CC
      CALL FREAD(-2, 'ENDFILE', 1, 'ERROR', 2, 'ENDLINE', 3,
     .           'VERB', 0)
CC
CC READ UNTIL VALID INPUT LINE OR END OF FILE
CC
   10 CALL FREAD(UNIT, ':', DUMMY, &20, &10, &10)
      CALL FREAD('*', 'R*8 V:', DCOL, NDMAX, &20, &10, &30)
      GO TO 30
CC
CC *** ERROR EXIT *** NO DATA READ IN
CC
   20 IER = 1
      CALL FREAD(-1, 'ENDFILE', 'ERROR', 'ENDLINE', 'VERB')
      RETURN
CC
CC VALID INPUT LINE READ, RE-SET FREAD PARAMETERS
CC
   30 IER = 0
      CALL FREAD(-1, 'ENDFILE', 'ERROR', 'ENDLINE', 'VERB')
      REWIND UNIT
CC
CC DETERMINE THE NUMBER OF COLUMNS:
CC
      DO 40 I = 1, NDMAX
        IF (DCOL(NDMAX - I + 1) .NE. 0.0D0) GO TO 50
   40 CONTINUE
      I = NDMAX + 1
   50 ICOL = NDMAX + 1 - I
CC
CC IF ICOL = 0 THEN A BLANK LINE WAS READ AND WE HAVE AN ERROR
CC
      IF (ICOL .EQ. 0) GO TO 20
CC
CC IF ICOL .LE. 3 THEN WE ASSUME WE HAVE 2 COLUMN DATA, OTHERWISE,
CC WE ASSUME WE HAVE NICOLET FORMAT DATA
CC
      IF (ICOL .LE. 3) GO TO 60
CC
CC NICOLET DATA:
CC
      CALL NICOL(UNIT, X, Y, N, NMAX)
      IF (N .EQ. 0) IER = 1
      RETURN
CC
CC TWO COLUMN DATA:
CC
   60 CALL TWOCOL(UNIT, X, Y, N, NMAX)
```

```
      IF (N .EQ. 0) IER = 1
      RETURN
      END
CCCCCCCCCCCCCCCCCCCCCCCCCCCCC
CCCCCCCCCCCCCCCCCCCCCCCCCCCCC
CC
CC ROUTINE TO READ IN 'NICOLET' DATA AND RETURN X AND Y VECTORS
CC
      SUBROUTINE NICOL(UNIT, X, Y, N, NMAX)
CC
CC UNIT  = FORTRAN UNIT NUMBER INPUT FILE IS ATTACHED TO
CC X     = VECTOR TO HOLD CHANNEL NUMBERS
CC Y     = VECTOR TO HOLD CHANNEL DATA
CC N     = NUMBER OF POINTS READ IN
CC NMAX  = MAXIMUM SIZE OF X AND Y VECTORS
CC
      INTEGER*4 UNIT, N, NMAX
      REAL*8 X(NMAX), Y(NMAX), DY
      REAL*8 CH1, E1, CH2, E2, ESL, EB
      LOGICAL*1 PCHR
      LOGICAL*1 ACHR /'*'/
      LOGICAL*4 EQUC
CC
CC ATTACH FILE
CC
      N = 0
      CALL FREAD(-2, 'ENDFILE', 1, 'ERROR', 2, 'VERB', 0, 'ENDLINE',
     1     'STREAM')
CC
CC DUMMY READ FOR FIRST LINE, CATCH 'EOF'
CC
      CALL FREAD(UNIT, ':', F, &40, &30)
CC
CC CHECK FOR ENERGY CALIBRATION LINE:
CC
      CALL FREAD('*', 'S, 2R*8:', PCHR, 1, E1, E2, &40, &4)
CC
CC IF FIRST CHAR ON FIRST LINE IS '*' AND TWO NUMBERS FOLLOW IT,
CC THEN WE HAVE CHANNEL/ENERGY CALIBRATION DATA AND CAN PROCEED
CC
      IF (EQUC(PCHR,ACHR)) GO TO 6
CC
CC MUST GET CALIBRATION FROM USER
CC
    4 WRITE (6,5)
    5 FORMAT(' ...ERROR, THE INPUT FILE IS IN NICOLET FORMAT'/
     .       '    BUT NO CHANNEL/ENERGY CALIBRATION DATA HAS'/
     .       '    BEEN SUPPLIED. ENTER THE TWO ENERGY VALUES'/
     .       '    FOR THE FIRST AND LAST CHANNELS"')
      CALL FREAD(5, '2R*8:', E1, E2, &40, &4)
CC
CC NOW RE-SET AND START THE ENCODING PROCESS
```

```
CC
    6 REWIND UNIT
      CALL FREAD(UNIT, ':', F, &40, &30)
CC
CC ENTRY TO NORMAL READ, READ DATA OFF A LINE UNTIL
CC ERROR ENCOUNTERED
CC
   10 CALL FREAD('*', 'R*8:', DY, &40, &30)
CC
CC PACK INTO ARRAYS (CHANNEL NUMBER IS ASSUMED TO START AT 1
CC                   AND IS CONVERTED TO AN ENERGY VALUE)
CC
   20 N = N + 1
      Y(N) = DY
      X(N) = N
      IF (N .GE. NMAX) GO TO 40
      GO TO 10
CC
CC ERROR READING INPUT LINE, START READING THE NEXT LINE
CC
   30 CALL FREAD(UNIT, 'R*8:', DY, &40, &30)
      GO TO 20
CC
CC NORMAL EOF AFTER SOME DATA READ
CC
   40 REWIND UNIT
      CALL FREAD(-1, 'ENDFILE', 'ENDLINE', 'ERROR', 'VERB')
CC
CC CONVERT CHANNEL NUMBER TO ENERGY
CC
      ESL = (E2 - E1)/(N - 1)
      EB  =  E1 - ESL
      DO 50 I = 1, N
        X(I) = ESL*I + EB
   50 CONTINUE
CC
CC TRASH THE FIRST AND LAST CHANNELS
CC
      Y(1) = Y(2)
      Y(N) = Y(N-1)
      RETURN
      END
CCCCCCCCCCCCCCCCCCC
CCCCCCCCCCCCCCCCCCC
CC
CC ROUTINE TO READ IN TWO COLUMN DATA AND RETURN X AND Y VECTORS
CC
      SUBROUTINE TWOCOL(UNIT, X, Y, N, NMAX)
CC
CC UNIT  = FORTRAN UNIT NUMBER INPUT FILE IS ATTACHED TO
CC X     = VECTOR TO HOLD CHANNEL NUMBERS
CC Y     = VECTOR TO HOLD CHANNEL DATA
```

```
CC N     = NUMBER OF POINTS READ IN
CC NMAX  = MAXIMUM SIZE OF X AND Y VECTORS
CC
      INTEGER*4 UNIT, N, NMAX
      REAL*8 X(NMAX), Y(NMAX)
CC
CC ATTACH FILE
CC
      N = 1
      CALL FREAD(-2, 'ENDFILE', 1, 'ERROR', 2, 'ENDLINE', 3,
     .           'VERB', 0)
CC
CC READ LOOP: EXITS ON END OF FILE OR VECTOR FULL CONDITION
CC
   10 CALL FREAD(UNIT, ':', F, &20, &10)
      CALL FREAD('*', '2R*8:', X(N), Y(N), &20, &10)
      N = N + 1
      IF (N .LE. NMAX) GO TO 10
CC
CC EOF:
CC
   20 N = N - 1
      REWIND UNIT
      CALL FREAD(-1, 'ENDFILE', 'ERROR', 'ENDLINE', 'VERB')
      RETURN
      END
C
C **** USUB ROUTINE ****
C
      SUBROUTINE USUB(ISEL)
      COMMON /CREAL/ CX, CY, CS, ERROR, APTR
      COMMON /CREAL/ SCALE, YOFF, XOFF
      COMMON /CCMPX/ CSY
      COMMON /CONTRL/ XLINK(39), XWHERE, YWHERE
      INTEGER*4 ECODE /21/
      LOGICAL*1 FNAME(30) /30*' '/
      LOGICAL*1 FYLE(60) /60*' '/
      INTEGER*4 F8 /8/
CC
CC CALSUB DATA VECTORS
CC
      REAL*8 CXV(2048), CYV(2048)
      INTEGER*4 CN
      COMMON /COMCV/ CXV, CYV
      COMMON /CINT/ KNOTS, CN, IER, ISMOO
CC
CC DATSUB DATA VECTORS
CC
      REAL*8 DXV(1024), DYV(1024)
      INTEGER*4 DN, ICDFLG
      COMMON /COMDV/ DXV, DYV
      COMMON /DREALV/ DDX, DDY, DSCALE, DYOFF, DXOFF
```

```
      COMMON /DINT/ DN, ICDFLG
CC
CC CUT VECTOR STORAGE
CC
      REAL*8 BX(2048), BY(2048)
      INTEGER*4 BN
CC
CC USUB FUNCTION SELECT:
CC
      IF (ISEL .LT. 1 .OR. ISEL .GT. 8) RETURN
      GO TO (10, 100, 120, 130, 200, 220, 330, 480), ISEL
C
C OPTION 1) ENTRY MESSAGE
C
   10 WRITE (6,20)
   20 FORMAT (' ENTER FOUR SCALE POINTS (CALC,DATA,CALC,DATA)'/
     1       ' TYPE AN "E" IF YOU MAKE A MISTAKE')
      GO TO 50
   30 WRITE (6,40)
   40 FORMAT (' *** ERROR *** RE-ENTER THE FOUR SCALE POINTS')
C
C GET CALC POINT
C
   50 CALL CXYIN(NSUB, XHIT, AMP1, ICODE)
      IF (ICODE .EQ. ECODE) GO TO 30
      WRITE (6,60) NSUB, AMP1
   60 FORMAT (1X, A4, ' AMP1 = ', G10.4)
C
C GET DATA POINT
C
      CALL DXYIN(NSUB, XHIT, AMP2, ICODE)
      IF (ICODE .EQ. ECODE) GO TO 30
      WRITE (6,70) NSUB, AMP2
   70 FORMAT (1X, A4, ' AMP2 = ', G10.4)
C
C GET A CALC POINT
C
      CALL CXYIN(NSUB, XHIT, AMP3, ICODE)
      IF (ICODE .EQ. ECODE) GO TO 30
      WRITE (6,80) NSUB, AMP3
   80 FORMAT (1X, A4, ' AMP3 = ', G10.4)
C
C GET DATA POINT
C
      CALL DXYIN(NSUB, XHIT, AMP4, ICODE)
      IF (ICODE .EQ. ECODE) GO TO 30
      WRITE (6,90) NSUB, AMP4
   90 FORMAT (1X, A4, ' AMP4 = ', G10.4)
C
C COMPUTE SCALE AND Y-OFFSET
C
      SCALE = (AMP4 - AMP2) / (AMP3 - AMP1)
```

```
      YOFF = AMP2 - (SCALE*AMP1)
      RETURN
C
C OPTION 2) CALC WHERE ONLY
C
  100 CALL CXYIN(NAME, XWHERE, YWHERE, KEY)
      WRITE (6,110) NAME, XWHERE, YWHERE
  110 FORMAT (2X, A4, 2G16.7)
      RETURN
C
C OPTION 3) DATA WHERE ONLY
C
  120 CALL DXYIN(NAME, XWHERE, YWHERE, KEY)
      WRITE (6,110) NAME, XWHERE, YWHERE
      RETURN
C
C OPTION 4) X-OFFSET
C
  130 WRITE (6,140)
  140 FORMAT (' LOCATE POSITIONS FOR VOFF (CALC,DATA)'/
     1       ' TYPE AN "E" TO RE-TRY')
      GO TO 170
  150 WRITE (6,160)
  160 FORMAT (' *** ERROR *** RE-ENTER THE TWO OFFSET POINTS')
C
C GET CALC POINT
C
  170 CALL CXYIN(NSUB, CX, YHIT, ICODE)
      IF (ICODE .EQ. ECODE) GO TO 150
      WRITE (6,180) NSUB, CX
  180 FORMAT (1X, A4, ' CX = ', G10.4)
C
C GET DATA POINT
C
      CALL DXYIN(NSUB, DX, YHIT, ICODE)
      IF (ICODE .EQ. ECODE) GO TO 150
      WRITE (6,190) NSUB, DX
  190 FORMAT (1X, A4, ' DX = ', G10.4)
C
C COMPUTE VOFF
C
      XOFF = CX - DX
      RETURN
C
C OPTION 5) ASSIGN UNIT 11 TO SMOOTHING FILE
C
  200 WRITE (6,210)
  210 FORMAT ('&ENTER FILE FOR SMOOTHING')
      CALL FREAD(5, 'S:', FNAME, 30)
      CALL FTNCMD('ASSIGN 11=?;', 0, FNAME)
      RETURN
C
```

```
C OPTION 6) ISOLATE REGION FOR CUTTING AND SPLICING
C
  220 WRITE (6,230)
  230 FORMAT(' LOCATE LEFT AND RIGHT SIDES OF THE CUT'/
     1       ' TYPE AN "E" TO RE-TRY')
      GO TO 260
  240 WRITE (6,250)
  250 FORMAT(' *** ERROR *** RE-ENTER LEFT AND RIGHTS SIDES OF THE CUT')
C
C GET CALC POINT LEFT
C
  260 CALL CXYIN(NSUB, CXL, YHIT, ICODE)
      IF (ICODE .EQ. ECODE) GO TO 240
      WRITE (6,270) NSUB, CXL
  270 FORMAT (1X, A4, '  LEFT CUT AT ', G10.4)
C
C GET CALC POINT RIGHT
C
      CALL CXYIN(NSUB, CXR, YHIT, ICODE)
      IF (ICODE .EQ. ECODE) GO TO 240
      WRITE (6,280) NSUB, CXR
  280 FORMAT (1X, A4, ' RIGHT CUT AT ', G10.4)
C
C LOCATE LEFT POINT IN CALC VECTOR
C
      ICXL = ICD(CXL, CXV, CN)
C
C LOCATE RIGHT POINT IN CALC VECTOR
C
      ICXR = ICD(CXR, CXV, CN) - 1
C
C LOCATE LEFT POINT IN DATA VECTOR
C
      IDXL = ICD(CXL, DXV, DN)
C
C LOCATE RIGHT POINT IN DATA VECTOR
C
      IDXR = ICD(CXR, DXV, DN) - 1
C
C MESH THE VECTORS TOGETHER.
C FIRST, THE CALC VECTOR UP TO THE CUT.
C
      BN = 1
      DO 290 I = 1, ICXL
        BX(BN) = CXV(I)
        BY(BN) = SCALE*CYV(I) + YOFF
        BN = BN + 1
  290 CONTINUE
C
C NOW ADD THE DATA VECTOR TO IT
C
      DO 300 I = IDXL, IDXR
```

```
      BX(BN) = DXV(I) + DXOFF
      BY(BN) = DSCALE*DYV(I) + DYOFF
      BN = BN + 1
  300 CONTINUE
C
C AND THEN THE REST OF THE CALC VECTOR
C
    DO 310 I = ICXR, CN
      BX(BN) = CXV(I)
      BY(BN) = SCALE*CYV(I) + YOFF
      BN = BN + 1
  310 CONTINUE
    BN = BN - 1
C
C SORT THE BIG VECTOR
C
    CALL SORT3('S=FL,,,8 END ', BX(1), BX(BN), F8, BY(1), F8)
C
C COPY IT OVER THE CALC DATA
C
    DO 320 I = 1, BN
      CXV(I) = BX(I)
      CYV(I) = BY(I)
  320 CONTINUE
    CN = BN
    CALL AINCN(CN)
    RETURN
C
C OPTION 7) SAVE CALC/DATA IN A FILE
C
  330 GO TO (331,332), ICDFLG
  331 WRITE (6,340)
  340 FORMAT ('&>> ENTER FILENAME TO SAVE CUT DATA IN')
    GO TO 333
  332 WRITE (6,341)
  341 FORMAT ('&>> ENTER FILENAME TO SAVE SUBTRACTED DATA IN')
  333 CALL FREAD(-2, 'ENDFILE', 1, 'ERROR', 2, 'VERB', 0, 'DELIM',
     1     '/;//')
    CALL FREAD(5, 'S:', FYLE, 60, &470, &470)
    CALL FREAD(-1, 'ENDFILE', 'ERROR', 'VERB', 'DELIM')
C
C RETURN IF NULL ENTRY
C
    IF (LCOMC(6,'      ',FYLE) .EQ. 0) RETURN
C
C CHECK FOR EXISTENCE
C
    CALL CREATE(FYLE, 1, 0, 256, &350, &410, &410, &410, &370,
   .&410, &390)
    GO TO 430
C
C ERROR RETURNS:
```

```
C
  350 WRITE (6,360)
  360 FORMAT (' *** ERROR: FILE ALREADY EXISTS, ENTER ANOTHER NAME')
      GO TO 330
  370 WRITE (6,380)
  380 FORMAT (' *** ERROR: ILLEGAL FILE NAME, ENTER ANOTHER NAME')
      GO TO 330
  390 WRITE (6,400)
  400 FORMAT (' *** ERROR: NO DISK SPACE LEFT IN THIS ACCOUNT!!!!')
      RETURN
  410 WRITE (6,420)
  420 FORMAT (' *** ERROR: CANNOT CREATE FILE / SYSTEM ERROR')
      RETURN
C
C FILE CREATED, ATTACH IT TO UNIT #12
C
  430 CALL FTNCMD('ASSIGN 12 = ?;', 0, FYLE)
C
C DUMP THE DATA FROM THE VECTORS
C
      GO TO (440, 460), ICDFLG
  440 WRITE (12,450) (CXV(I), CYV(I), I=1,CN)
  450 FORMAT (2G18.8)
      RETURN
  460 DO 461 I = 1, DN
        DDX = DXV(I) + DXOFF
        DDY = DSCALE*DYV(I) + DYOFF
        WRITE (12,450) DDX, DDY
  461 CONTINUE
      DYOFF = 0.0
      DXOFF = 0.0
      DSCALE = 1.0
  470 RETURN
C
C OPTION 8) SUBTRACT THE SMOOTHED CALC FROM THE DATA
C
  480 CALL SPEVAL(DXV, DXOFF, BY, DN)
      DO 490 I = 1, DN
        DXV(I) = DXV(I) + DXOFF
        DYV(I) = (DSCALE*DYV(I) + DYOFF) - (SCALE*BY(I) + YOFF)
  490 CONTINUE
      DSCALE = 1.0
      DYOFF = 0.0
      DXOFF = 0.0
      RETURN
      END
C
C ROUTINE TO RETURN A DATA HIT ONLY
C
      SUBROUTINE DXYIN(NAME, X, Y, KEY)
      INAME = IGPIKS('DATS','DATU','DATW','DATG')
      NAME = IGPIKN(0,X,Y,KEY)
```

```
      RETURN
      END
C
C ROUTINE TO RETURN A CALC HIT ONLY
C
      SUBROUTINE CXYIN(NAME, X, Y, KEY)
      INAME = IGPIKS('CALS','CALU','CALW','CALG')
      NAME = IGPIKN(0,X,Y,KEY)
      RETURN
      END
C
C ROUTINE TO LOCATE A POINT IN A VECTOR
C
      FUNCTION ICD(X, XV, N)
      REAL*8 X, XV(N)
      DO 10 I = 1, N
        IF (XV(I) .LT. X) GO TO 10
        ICD = I
        RETURN
   10 CONTINUE
      ICD = N
      RETURN
      END
C
C ROUTINE TO SET AINCNO = N
C
      SUBROUTINE AINCN(N)
      COMMON /CONTRL/ EOF, XLINK(10), AINCNO
      AINCNO = N
      RETURN
      END
C
C SPLINE EVALUATOR (A SMOOTHED DATASET HAS TO BE PRESENT
C                   FOR THIS TO WORK)
C
      SUBROUTINE SPEVAL(DX, DXOFF, CY, N)
      REAL*8 DX(N), DXOFF, CY(N), C(28,3), Y(28), XK(28), D
      COMMON /SPFIT/ C, Y, XK, NXK1
      J = 1
      DO 30 I = 1, NXK1
   20   IF ((DX(J)+DXOFF) .GT. XK(I+1)) GO TO 30
        D = (DX(J)+DXOFF) - XK(I)
        CY(J) = ((C(I,3)*D + C(I,2))*D + C(I,1))*D + Y(I)
        J = J + 1
        IF (J .GT. N) GO TO 40
        GO TO 20
   30 CONTINUE
   40 CONTINUE
      RETURN
      END
```

```
COMMON /CREAL/ ALFA1, ALFA2, ALFA3, ALFA4
COMMON /CREAL/ GAMA1, GAMA2, GAMA3, GAMA4
COMMON /CREAL/ AMP1, AMP2, AMP3, AMP4, SCALE, RESOL, VOFF
COMMON /CREAL/ E1, E2, E3, E4
COMMON /CREAL/ VOLT, SIG, EEND, ESTART, NSTEP
COMMON /CINT/ NSIG, N,NAREA
COMMON /DREALV/ DVOLT, DSIG, DVOFF, DSIGOFF
STEPVAR=NSTEP
NAREA=0
ANSWER=VOLT,SIG
FROM=1
START=1.0
AINCNO=400
STEP=1
CPLOT=SIG
CAGAINST=VOLT
DPLOT=DSIG
DLNTYP=0
DAGAINST=DVOLT
MACRO/BOX/START=XN,END=XX,TOP=YXVC,BOTTOM=YNVC,REDRAW
MACRO/DBOX/DTOP=YXVD,DBOT=YNVD,START=XN,END=XX,REDRAW
MACRO/RESET/TOP=BOTTOM,DTOP=DBOT
•
* PARAMETER DEFINITIONS:(Specify parameters)
•
N=400
NSTEP=1
EEND=403
ESTART=383
ALFA1=.0
ALFA2=.0
ALFA3=.0
ALFA4=.0
GAMA1=0.27
GAMA2=1.2
GAMA3=0.71
GAMA4=1.
AMP1=1.0
AMP2=0.2
AMP3=.2
AMP4=.1
E1=396.2
E2=393.2
E3=390.44
E4=387.44
SCALE=0.
NSIG=4
RESOL=.291
VOFF=0.0
```

```
DVOFF=0.
DSIGOFF=0.0
*
* END OF PARAMETER DEFINITIONS
*
$R *FTN SCARDS=CLIU:DON1(100) SPUNCH=CLIU:DON1(-500,-100) PAR=TEST
$SOURCE PREVIOUS
$RUN ANDR:GANDER+CLIU:DON1(-500,-100) 5=CLIU:DON1(-99,-1)+*MSOURCE*
$SOURCE PREVIOUS
      SUBROUTINE CALSUB
      REAL*4 ALFA1, ALFA2, ALFA3, ALFA4, GAMA1, GAMA2, GAMA3, GAMA4
      REAL*4 VOLT, AMP1, AMP2, AMP3, AMP4, SCALE, RESOL, SIG
      REAL*4 E1, E2, E3, E4, NSTEP
      REAL*8 ALFA(4)
      REAL*8 AMP(4), E(4), GAUS, S, SS(1000), V(1000), VV(1000), EE
      REAL*8 SG, PEAK,W1,W2
      REAL*8 ANSWER, ERR, OFF, GAMA(4), RESULT(1000), RES(1000)
      REAL*8 VG
      INTEGER*4 N, NSIG
      REAL*8 PI /3.141592653589793D0/
C
C     GANDER COMMONS
C
      COMMON /CREAL/ ALFA1, ALFA2, ALFA3, ALFA4
      COMMON /CREAL/ GAMA1, GAMA2, GAMA3, GAMA4
      COMMON /CREAL/ AMP1, AMP2, AMP3, AMP4, SCALE, RESOL, VOFF
      COMMON /CREAL/ E1, E2, E3, E4
      COMMON /CREAL/ VOLT, SIG, EEND, ESTART, NSTEP
      COMMON /CINT/ NSIG, N ,NAREA
      COMMON /CONTRL/ EOF
      IF (EOF .EQ. 0.0) GO TO 70
      EOF = 0.0
          PI=3.14159265
      ALFA(1) = ALFA1
      ALFA(2) = ALFA2
      ALFA(3) = ALFA3
      ALFA(4) = ALFA4
      E(1) = E1
      E(2) = E2
      E(3) = E3
      E(4) = E4
      AMP(1) = AMP1
      AMP(2) = AMP2
      AMP(3) = AMP3
      AMP(4) = AMP4
      GAMA(1) = GAMA1
      GAMA(2) = GAMA2
      GAMA(3) = GAMA3
      GAMA(4) = GAMA4
      DV = (EEND - ESTART) / N
      DO 20 I = 1, N
        S = 0.
```

```
      V(I) = EEND - (DV*I)
      DO 10 J = 1, NSIG
        EE = V(I) - E(J)
        W1 = ((PI*ALFA(J)/2.D0) + ((1.D0 - ALFA(J))*DATAN(EE/GAMA(J))))
          W1=DCOS(W1)
        W1 = W1 * DGAMMA(1. - ALFA(J))
        W2 = ((EE**2) + (GAMA(J)**2)) ** ((1.D0 - ALFA(J))/2.)
        PEAK = W1 / W2
         PEAK=PEAK*AMP(J)
        S = S + PEAK
   10   CONTINUE
      RESULT(I) = S
   20 CONTINUE
  767     FORMAT(2(E10.3,4X),I4,2X,I3)
     DO 40 I = 1, N
      DO 30 J = 1, I
        VV(J) = V(J)
        RES(J) = RESULT(J)
   30   CONTINUE
      IFAIL = 1
      CALL D01GAF(VV, RES, I, ANSWER, ERR, IFAIL)
      OFF =-ANSWER * SCALE
      SS(I) = RESULT(I) + OFF
   40 CONTINUE
        IF(NAREA.EQ.1) GOTO 70
         IGAUS=RESOL/DV
         IF(IGAUS.LT.5) GOTO 888
         JMAX=8*IGAUS
       DVV=8*RESOL/JMAX
          JMAX1=JMAX/2
C         WRITE(6,767) RESULT(I),OFF,JMAX,JMAX1
     DO 60 I = 1, N
      SG = 0.
      DO 50 J = 1, JMAX
        JJ = I + J - JMAX1
        IF (JJ .LT. 1) GO TO 50
        IF (JJ .GT. N) GO TO 50
        VG = V(I + J -JMAX1)-V(I)
          VG=DABS(VG)
        GAUS = DEXP(-((VG/(2.*RESOL+0.13*VG))**2))
        SG = SG + (SS(JJ)*GAUS)*DV
   50   CONTINUE
         SG=SG/((3.1415**.5)*RESOL*2.)
      RESULT(I)=SG
   60 CONTINUE
   70 ISTEP = NSTEP
     SIG = RESULT(ISTEP)
           IF(NAREA.EQ.1) SIG=SS(ISTEP)
     VOLT = V(ISTEP)
       GOTO 889
  888    WRITE(6,887) IGAUS
  887    FORMAT('INCREASE N',5X,I3)
```

```
 889     RETURN
      END
C
C *** DATSUB ROUTINE TO READ IN TWO COLUMN DATA WITH X-OFFSET
C
      SUBROUTINE DATSUB
      COMMON /DREALV/ VOLT, SIG, VOFF, SOFF
      COMMON /CONTRL/ EOF
      IF (EOF .EQ. 0) GO TO 10
      EOF = 0.0
      CALL FREAD(-2, 'ENDFILE', 1, 'ERROR', 2, 'VERB', 0)
   10 CALL FREAD(10, ':', F, &20, &10)
      CALL FREAD('*', '2R:', VOLT, SIG, &20, &10)
      VOLT = VOLT - VOFF
      SIG = SIG - SOFF
      RETURN
   20 EOF = 1.0
      CALL FREAD(-1, 'ENDFILE', 'ERROR', 'VERB')
      REWIND 10
      RETURN
      END
```

BIBLIOGRAPHY

Antonides E, Janse EC and Sawatzky GA, 1977, Phys. Rev. 15, 1669

Arrott AS, Heinrich B, Liu C and Purcell ST, 1985, in press

Bagus PS, Freeman AJ and Sasaki F, 1973, Phys. Rev. Lett. 30, 850

Barrett CS, 1952, "Structure of Metals", Barrett CS and Massalski TB, 1980, 3rd rev. ed. Pergamon, Oxford New York, (International Series on Materials and Technology, Vol. 35)

Barry JJ and Hughes HP, 1983, J. Phys. C: Solid St. Phys. 16, L275

Bauer E, 1969, "Reflection Electron Diffraction" in "Techniques of Metal Research", vol.2, pt.2, ed. R.F.Bunshah, Interscience Publishers, New York

Bauer E, 1972, Vacuum, 22, 539

Beal AR, 1979, "Physics and Chemistry of Materials with Layered Structures" Vol.6: 'Intercalated Layer Materials', ed. F.Levy, Reidet, pp251-305

Bechstedt F, 1982, Phys. Stat. Sol. (b)112, 9

Beeby JL, 1979, Surf. Sci. 80, 56

Bergmann G, 1978, Phys. Rev. Lett. 41, 264

Binns C and Norris C, 1982, Surf. Sci. 116, 338

Bradley AJ and Thewlis J, 1937, Proc. Roy. Soc. (London), A115, 456

Bransden BH and Joachain CJ, 1983, "Physics of Atoms and Molecules", Longman, London and New York, pp461-526

Brodsky MB, 1981, J. Appl. Phys. 52, 1665

Brodsky MB, 1983, J. Magn. Magn. Mat. 35, 99

Chattarji D, 1976, "The Theory of Auger Transitions", Academic Press, London New York San Francisco

Chaudhari P, Cuomo JJ, Gambino RJ and Giess EA, 1977 in "Physics of Thin Films" Vol.9, p263, ed. G.Hass, M.H.Francombe and R.W.Hoffman, Academic Press, New York

Chiarello G, Colavita E, Crescenzi MDe and Nannarone S, 1984, Phys. Rev. B29, 4878

Clark DT and Adams DB, 1971, Chem. Phys. Lett. 10, 121

Coad JP, Bishop HE and Riviere JC, 1970, Surf. Sci. 21, 253

Cowley JM, 1981, "Diffraction Physics", 2nd Ed., North-Holland Publishing Company, Amsterdam New York Oxford

Crescenzi MDe, Papagno L, Chiarello G, Scarmozzino R, Colavita E, Rosei R and Mobilio S, 1981, Solid St. Comm. 40, 613

Davis LE, MacDonald NC, Palmberg PW, Riach GE and Weber RE, 1978, Handbook of Auger Electron Spectroscopy, 2nd Ed. Perkin Elmer Co. Physical Electronics Division, Eden Prairie, Minnesota

Doniach S and Sunjic M, 1970, J. Phys. C3, 285

Dwyer VM and Matthew JAD, 1984, Surf. Sci. 143, 57

Feldkamp LA and Davis LC, 1979, Phys. Rev. Lett. 43, 151

Frank FC and van der Merwe JH, 1949a, Proc. Roy. Soc. (London) A198, 205

Frank FC and van der Merwe JH, 1949b, Proc. Roy. Soc. (London) A198, 216

Friedel J, 1954, Philos. Mag. Suppl. 3, 446

Friend RH, Beal AR and Yoffe AD, 1977, Phil. Mag. 35, 1269

Fu CL, Freeman AJ and Oguchi T, 1985, Phys. Rev. Lett. 54, 2700

Fuggle JC, 1981, "High Resolution Auger Spectroscopy of Solids and Surfaces" in "Electron Spectroscopy: Theory, Techniques and Applications" Vol.4, ed. C.R.Brundle and A.D.Baker, Academic Press, London New York

Goldberger ML and Watson KM, 1964, "Collision Theory", John Wiley and Sons, New York

Guillot C, Ballu Y, Paigne J, Lecante J, Jain KP, Thiry P, Pinchaux R, Petroff Y and Falicov LM, 1977, Phys. Rev. Lett. 39, 1632

Heidenreich RD, 1964, "Fundamentals of Transmission Electron Microscopy", Interscience, New York

Heinrich B, Liu C and Arrott AS, 1985, J. Vac. Sci. Technol. B3, 766

Heinrich B, Arrott AS, Cochran JF, Liu C and Myrtle K, 1985b, in press

Hink W and Ziegler A, 1969, Z. Phys. 226, 222

Hubbard J, 1963, Proc. Roy. Soc. 276, 238

Hubbard J, 1964, Proc. Roy. Soc. 277, 237

Hubbard J, 1964, Proc. Roy. Soc. 281, 401

Hufner S and Wertheim GK, 1975, Phys. Lett. 51A, 299

Jackson DC, Gallon TE and Chambers A, 1973, Surf. Sci. 36, 381

Jepsen O, Madsen J and Anderson OK, 1980, J. Magn. Magn. Mater. 15-18, 867

Jepsen O, Madsen J and Anderson OK, 1982, Phys. Rev. B26, 2790

Jesser WA and Kuhlmann-Wilsdorf D, 1967, Phys. Status Solidi, 19, 95

Kittel C, 1976, "Introduction to Solid State Physics", 5th ed. John Wiley and Sons, New York, p69

Klebanoff LE and Shirley DA, 1985, to be published in Phys. Rev. B

Koopmans T, 1934, Physica 1, 104

Kostroun VO, Chen MH and Crasemann B, 1971, Phys. Rev. A3, 533

Kowalczyk SP, Ley L, McFeely FR and Shirley DA, 1973, Phys. Rev. B7, 4009

Kowalczyk SP, Ley L, McFeely FR and Shirley DA, 1975, Phys. Rev. B11, 1721

Krause MO and Ferreira JG, 1975, J. Phys. B8, 2007

Leapman RD, Rez P and Mayers DF, 1980, J. Chem. Phys. 72, 1232

Ley L, Kowalczyk SP, McFeely FR and Shirley DA, 1973, Phys. Rev. B8, 2392

Li ZM, Palffy-Muhoray P and Bergersen B, 1985, to be published in J. Phys. C

Liberman DA, Cromer DT and Waber JT, 1965, Phys. Rev. 137, 27

Liebermann L, Clinton J, Edwards DM and Mathon J, 1970, Phys. Rev. Lett. 25, 323

Lince JR, Nelson JG and Williams RS, 1983. J. Vac. Sci. Technol. B1, 553

Liu C, 1983, "Single Layers of the Metallic Layered Compounds TaS_2 and NbS_2", M.Sc. Thesis, Simon Fraser University, CANADA

Liu C, Singh O, Joensen P, Curzon AE and Frindt RF, 1984, Thin Solid Films, 113, 165

Liu C and Frindt RF, 1985, Phys. Rev. B31, 4086

Markov I and Milchev A, 1984, Surf. Sci. 136, 519

Martensson N and Johansson B, 1980, phys. Rev. Lett. 45, 482

Meservey R, Tedrow PM and Kalvey VR, 1980, Solid St. Commun. 36, 969

Miedema AR and Dorleijn JWF, 1980, Surf. Sci. 95, 447

Namba Y and Vook RW, 1981, Thin Solid Films, 82, 165

Noffke J and Fritsche L, 1981, J. Phys. C14, 89

Nozieres P and de Dominicis CT, 1969, Phys. Rev. 178, 1097

Oh SJ, Allen JW, Lindau I and Mikkelsen JCJr, 1982, Phys. Rev. B26, 4845

Oguchi T and Freeman AJ, 1984, J. Magn. Magn. Mater. 46, L1

Okuda T, Koshizuka N and Ando K, 1983, J. Magn. Magn. Mater. 35, 164

Parkin SSP and Friend RH, 1980, Phil. Mag. B41, 65

Pearson WB, 1958, "A Handbook of Lattice Spacing and Structures of Metals and Alloys", Pergamon Press, Oxford, pp55–75

Pierce DT and Siegmann HC, 1974, Phys. Rev. B9, 4035

Powell CJ, 1974, Surf. Sci. 44, 29

Ranke W and Jacobi K, 1975, Surf. Sci. 47, 525

Rau C and Eichner S, 1981, Phys. Rev. Lett. 47, 939

Samsonov GV, 1968, "Handbook of the Physicochemical Properties of the Elements" ed. G.V.Samsonov, translated from Russian, IFI/Plenum, New York

Sawatzky GA, 1977, Phys. Rev. Lett. 39, 504

Sawatzky GA and Lenselink A, 1980, Phys. Rev. B21, 1790

Seah MP, 1972, Surf. Sci. 32, 703

Seah MP, 1983, in "Practical Surface Analysis by Auger and X-ray Photoelectron Spectroscopy", ed. D.Briggs and M.P.Seah, John Wiley and Sons, New York, p204

Seah MP and Dench WA, 1979, Surf. Interface Anal. 1, 2

Shiga M, 1973, in "Magnetism and Magnetic Materials", pt.1, American Institute of Physics, New York (1974), p463

Shirley DA, 1972, Phys. Rev. B5, 4709

Shirley DA, 1978, in "Photoemission in Solids I", ed. M.Cardona and L.Ley, Springer-Verlag Berlin Heidelberg New York, p165

Shirley DA, Martin RL, Kowalczyk SP, McFeely FR and Ley L, 1977, Phys. Rev. B15, 544

Siegbahn K, 1974, J. Electr. Spectr. 5, 3

Siegbahn K, Hammond D, Fellner-Felldegg H and Barnett EF, 1972, Science, 176, 245

Steiner P, Hochst H and Hufner S, 1980, Phys. Lett. 76A, 335

Stern EA, 1974, Phys. Rev. B10, 3027

Sully AH, 1955, "Maganese", Academic Press, New York

Takei WJ, Shirane G and Frazer BC, 1960, Phys. Rev. 119, 122

Tersoff J and Falicov LM, 1982, Phys. Rev. B26, 6186

Timoshenko S, 1934, "Theory of Elasticity", McGraw-Hill, London, pp12-134

Timoshenko S and Goodier JN, 1951, "Theory of Elasticity", 2nd ed. McGraw-Hill, New York, p148

Vainshtein BK, 1964, "Structure Analysis by Electron Diffraction", Pergamon, New York

van der Merwe JH, 1964, in "Single Crystal Films", ed. M.H.Francombe and H.Sato, Pergamon, Oxford, p139

van der Merwe JH, 1966, in "Basic Problems in Thin Film Physics", ed. R.Niedermayer and H.Mayer, Vandenhoeck and Ruprecht, Gottingen, p122

van der Merwe JH and Ball CAB, 1975, in "Epitaxial Growth", ed. J.W.Matthews, pt.B, Academic Press, New York, p493

van Hove MA and Tong SY, 1979, "Surface Crystallography by LEED, Theory, Computation and Structural Results", Springer-Verlag, Berlin Heidelberg New York

van Vleck JH, 1934, Phys. Rev. 45, 405

van Vleck JH, 1953, Rev. Mod. Phys. 25, 220

Veal BW and Paulikas AP, 1983, Phys. Rev. Lett. 51, 1995

Veal BW and Paulikas AP, 1985, Phys. Rev. B31, 5399

Wagner CD, Riggs WM, Davis LE, Moulder JF and Mulenberg GE, 1979, Handbook of X-ray Photoelectron Spectroscopy, Perkin Elmer Co. Physical Electronics Division, Eden Prairie, Minnesota

Wang CS and Freeman AJ, 1980, Phys. Rev. B21, 4585

Wang DS, Freeman AJ and Krakauer H, 1981, Phys. Rev. B24, 1126

Wang DS, Freeman AJ and Krakauer H, 1982, Phys. Rev. B26, 1340

Weber RE and Johnson AL, 1969, J. Appl. Phys. 40, 314

Williams AR and Lang ND, 1978, Phys. Rev. Lett. 40, 954

Williamson DL, Bukshpan S and Ingalls R, 1972, Phys. Rev. B6, 4194

Wu TY and Ohmura T, 1962, "Quantum Theory of Scattering", Prentice Hall, Englewood Cliffs, p26